

CHEMICAL EXPANSION IN MANGANITES

A THESIS SUBMITTED TO
THE GRADUATE SCHOOL OF NATURAL AND APPLIED SCIENCES
OF
MIDDLE EAST TECHNICAL UNIVERSITY

BY

MEHMET HAZAR ŞEREN

IN PARTIAL FULFILLMENT OF THE REQUIREMENTS
FOR
THE DEGREE OF MASTER OF SCIENCE
IN
METALLURGICAL AND MATERIALS ENGINEERING

JUNE 2015

Approval of the thesis:

CHEMICAL EXPANSION IN MANGANITES

submitted by **MEHMET HAZAR ŞEREN** in partial fulfillment of the requirements for the degree of **Master of Science in Metallurgical and Materials Engineering Department, Middle East Technical University** by,

Prof. Dr. Gülbin Dural Ünver

Dean, Graduate School of **Natural and Applied Sciences**

Prof. Dr. Cemil Hakan Gür

Head of Department, **Metallurgical and Materials Engineering**

Prof. Dr. Cemil Hakan Gür

Supervisor, **Metallurgical and Materials Eng. Dept., METU**

Examining Committee Members:

Prof. Dr. Tayfur Öztürk

Metallurgical and Materials Eng. Dept., METU

Prof. Dr. Cemil Hakan Gür

Metallurgical and Materials Eng. Dept., METU

Prof. Dr. Kadri Aydınol

Metallurgical and Materials Eng. Dept., METU

Assoc. Prof. Dr. Yunus Eren Kalay

Metallurgical and Materials Eng. Dept., METU

Assist. Prof. Dr. Caner Şimşir

Manufacturing Eng. Dept., ATILIM UNIVERSITY

Date: 29.06.2015

I hereby declare that all information in this document has been obtained and presented in accordance with academic rules and ethical conduct. I also declare that, as required by these rules and conduct, I have fully cited and referenced all material and results that are not original to this work.

Name, Last Name: Mehmet Hazar Şeren
Signature :

ABSTRACT

CHEMICAL EXPANSION IN MANGANITES

Şeren, Mehmet Hazar

M.S., Department of Metallurgical and Materials Engineering

Supervisor: Prof. Dr. Cemil Hakan GUR

June 2015, 107 Pages

Manganites are type of manganese oxides having mixed valence states with perovskite structure represented as $\text{Ln}_{1-x}\text{A}_x\text{MnO}_3$ (Ln= rare-earth cation, A= alkaline earth cation) and they have been widely studied due to their potential applications in various important areas and their interesting properties. Numerous investigations have focused on their production, characterization of their properties and solution of problems encountered during their applications. Some of these applications are cathode and electrolyte materials for solid oxide fuel cells (SOFC), piezoelectric sensors or energy harvesting by thermoelectric materials.

In some applications, materials can be in contact with highly oxidizing and/or reducing atmospheres. The possible variations in the stoichiometry of the materials under these conditions may also lead to changes in their lattice parameters. This effect is known as “chemical expansion”. The component made of such a material may malfunction when dimensional stabilities occur. For instance, dimensional

changes cause residual stresses in thin film structures if the film is clamped to a rigid substrate. When these stresses are above a certain limit, some defects like cracks or hillocks are formed and the film loses its function. Therefore it is of cardinal importance to observe these dimensional variations and understand the governing mechanisms.

The aim of this study is to explore chemical expansion coefficients of $\text{La}_{0.5}\text{Ca}_{0.5}\text{MnO}_{3-\delta}$ (LCMO) and $\text{La}_{1-x}\text{Sr}_x\text{MnO}_{3-\delta}$ (LSMO) ($x= 0, 0.1, 0.2, 0.3, 0.4, 0.5, 0.6, 0.7, 0.8, 0.9, 1$) for the first time in literature. In addition, effect of Sr dopant on chemical expansion coefficient is another aim of this study. The chemical expansion in the structure during O loss was determined by combined study of dilatometry, in-situ X-ray diffraction and thermogravimetric analysis. Microstructural and chemical analysis were performed using room temperature X-ray diffraction, scanning electron microscopy and energy dispersive X-ray spectroscopy. With increasing Sr dopant, chemical expansion coefficient and δ values have decreasing trend whereas the absence of La in the structure leads to increase in chemical expansion. Therefore, the lowest chemical expansion coefficient is observed in LSMO9 samples. Slope changes are observed in TGA curves and the reason for this can be explained with the effect of Jahn-Teller distortion due to change in Mn valence state.

Keywords: Manganites, Chemical expansion, Perovskites, Oxygen vacancy

ÖZ

MANGANİTLERDE KİMYASAL GENLEŞME

Şeren, Mehmet Hazar

Yüksek Lisans, Metalurji ve Malzeme Mühendisliği Bölümü

Tez Yöneticisi: Prof. Dr. Cemil Hakan GÜR

Haziran 2015, 107 Sayfa

$Ln_{1-x}A_xMnO_3$ (Ln = nadir toprak elementi katyonu, A = toprak alkali elementi katyonu) şeklinde gösterilen perovskit kristal yapısıyla birlikte karışık değerlik elektronlarına sahip olan mangan oksit çeşitlerine manganit denir. Çeşitli kullanım alanlarındaki potansiyel uygulamalarından dolayı geniş bir şekilde çalışılmaktadır. Pek çok araştırma onların üretimine, özelliklerinin karakterizasyonuna ve uygulamaları sırasında çıkabilecek problemlerin çözümlerine odaklanmışlardır. Bu uygulamaların bazıları, kati oksit yakıt pilleri için katot ve elektrolit malzemeleri, piezoelektrik sensörler ve termoelektrik malzemeler tarafından enerji toplanmasıdır.

Bazı uygulamalarda, malzemeler yüksek derecede indirgeyici ve/veya yükseltgeyici atmosferlerle temas içinde olabilir. Bu şartlar altında malzemenin stokiyometrisindeki çeşitli varyasyonlar, kristal parametrelerinde değişikliğe sebep olabilir. Bu etki “kimyasal genleşme” olarak adlandırılır. Bu malzemelerden yapılan

parçalar boyutsal kararsızlıklar oluştuğu zaman arızalanabilir. Örneğin, film sert altlık üzerine kaplanmışsa boyutsal değişiklikler ince film yapısında kalıntı gerilmelere sebep olur. Bu gerilmeler belli bir limitin üstünde olduğunda, çatlaklar ve tepecikler gibi bazı kusurlar oluşur ve ince film fonksiyonunu kaybeder. Bu yüzden, boyutsal varyasyonları incelemek ve mekanizmalarını anlamak büyük önem taşımaktadır.

Bu çalışmanın amacı $\text{La}_{0.5}\text{Ca}_{0.5}\text{MnO}_{3-\delta}$ (LCMO) ve $\text{La}_{1-x}\text{Sr}_x\text{MnO}_{3-\delta}$ (LSMO) ($x= 0, 0.1, 0.2, 0.3, 0.4, 0.5, 0.6, 0.7, 0.8, 0.9, 1$)' nin kimyasal genleşme katsayılarını literatürde ilk defa araştırmaktır. Ayrıca, Stronsiyum (Sr) dopantının kimyasal genleşmeye etkisi çalışmanın başka bir amacıdır. Oksijen kaybı sırasında yapıdaki kimyasal genleşme, dilatometre, in-situ X-ray kırınımı ve termogravimetrik analizlerinin kombinasyonu ile belirlenmiştir. Mikro yapısal ve kimyasal analizler oda sıcaklığında X-ray kırınımı, taramalı elektron mikroskobu ve enerji ayırıcı X-ray spektrometresi ile yapılmıştır. Artan Sr dopantıyla birlikte, kimyasal genleşme katsayısı ve δ değerleri azalır; ancak yapıda Lantanum (La) eksikliği, kimyasal genleşmenin artmasına yol açar. Bu yüzden, en düşük kimyasal genleşme katsayısı LSMO9 örneklerinde gözlemlenmiştir. TGA eğrilerinde eğim değişiklikleri tespit edilmiştir ve nedeni Mn değerliğinin değişmesinden dolayı görülen Jahn-Teller bozukluğunun etkisiyle açıklanmıştır.

Anahtar kelimeler: Manganitler, Kimyasal Genleşme, Perovskitler, Oksijen boşluğu

To Dr. Yener Kuru...

ACKNOWLEDGEMENTS

This study is financially supported by TUBITAK 112M844 project. I would like to thank Assoc. Prof. Dr. Meltem Asiltürk for providing samples and sharing invaluable experience and information with us throughout the study. I would also like to express my gratitude to Prof. Dr. Mehmet Ali Gülgün and Melike Mercan Yıldızhan for their efforts in dilatometry and SEM experiments.

I am indebted to my advisor Assoc. Prof. Dr. Yener Kuru in the first place for his guidance all the way from the beginning to the end. I would like to thank him for the freedom that he has given me during thesis study. Also, I would never finish my thesis without the guidance of Assoc. Prof. Dr. Yunus Eren Kalay. I count myself very lucky to had such an great advisors who involve each step of the research patiently and willingly and express them my deepest gratitude.

I want to thank my only labmate, Ziya Çağrı Torunoğlu, for his support and help to prepare for this thesis and all the other favors as well. Moreover, I would like to thank Mertcan Başkan, Doğançan Sarı, Bengisu Yaşar, Özgün Acar, Sena Okay, Zeynep Öztürk, Ayşe Merve Genç Ünalın, Burcu Arslan, Ekin Solak, Serkan Yılmaz, Fatih Sıkan, Simge Tülbez, Şafak Doğu, Ezgi Onur, Gözde Yıldırım, Yadigar Seymen, Burçin Kaygusuz, Samet Can and Akın Akgün for their invaluable friendship. I specially thank Barış Alkan for his contributions to Rietveld Refinement Analysis. I would like to express my wholehearted and deepest appreciations to my dear friends Lütfi Ağartan and Mustafacan Kutsal. And I owe them much for always being supportive and helpful. I would like to give my special thanks to Firdevs Gonca Şaşal for entering my life and changing it in a positive manner.

Last but not least, I am thoroughly appreciated to my parents Sema and Ahmet, my sisters Hazal and Sultan and my nephew Patila for keeping their supports by all means since I was born. It is a great pleasure to have parents, sisters and nephew and know they are always with me.

TABLE OF CONTENTS

ABSTRACT.....	v
ÖZ	vii
ACKNOWLEDGEMENTS	x
TABLE OF CONTENTS	xi
LIST OF TABLES	xiv
LIST OF FIGURES	xv
NOMENCLATURE.....	xix
CHAPTERS	
1. INTRODUCTION	1
2. LITERATURE REVIEW.....	5
2.1 Perovskites	5
2.1.1 Crystal Structure of Perovskites.....	5
2.1.2 Distortions in Perovskites	6
2.1.2.1 Jahn-Teller Effects	6
2.1.2.2 Size Effects.....	7
2.1.2.3 Deviations from ABO_3 Compositions.....	8
2.1.3 Examples of Distorted Perovskites	8
2.2 Manganites.....	9

2.2.1 $\text{La}_{1-x}\text{Sr}_x\text{MnO}_{3-\delta}$	10
2.2.2 $\text{La}_{1-x}\text{Ca}_x\text{MnO}_{3-\delta}$	12
2.3 Defect Chemistry	14
2.3.1 Point Defects	14
2.3.2 Notation in Defect Chemistry	16
2.3.3 Non-Stoichiometry in Metal Oxides	16
2.3.4 Defects Related Properties	18
2.4 Chemical Expansion	18
2.4.1 Thermal Expansion	21
2.4.2 Problems Arising from Chemical Expansion.....	23
2.4.3 Examples of Chemical Expansion.....	24
2.5 Methods for Production of LSMO and LCMO Powders.....	24
2.5.1 Solid State Reaction Method.....	24
2.5.2 Pechini Method	25
2.5.3 Solution Combustion Synthesis Method.....	27
2.5.4 Hydrothermal Synthesis Methods	28
2.5.5 Co-precipitation Method	28
2.5.6 Sol-Gel Method.....	29
3. EXPERIMENTAL PROCEDURE	31
3.1 Powder Synthesis	31
3.2 Powder Characterization.....	32
3.2.1 X-Ray Diffraction Analysis	32
3.2.2 Thermogravimetric Analysis (TGA).....	33

3.2.3 Scanning Electron Microscopy (SEM)	34
3.2.4 Dilatometry	34
4. SYNTHESIS OF LCMO5 & LSMO SERIES	35
4.1 Synthesis of $\text{La}_{0.5}\text{Ca}_{0.5}\text{MnO}_{3-\delta}$	35
4.2 Synthesis of LSMO Series	35
5. MEASUREMENT OF CHEMICAL EXPANSION.....	39
5.1 General Remarks.....	39
5.2 Room Temperature Investigation of LCMO5 and LSMO Series.....	39
5.3 Chemical Expansion Coefficient of $\text{La}_{0.5}\text{Ca}_{0.5}\text{MnO}_{3-\delta}$ (LCMO5)	44
6. CHEMICAL EXPANSION IN LSMO SERIES	53
6.1 Thermogravimetric Analysis (TGA) of LSMO Series	53
6.2 In-Situ X-Ray Diffraction Analysis	62
6.3 Scanning Electron Microscope (SEM) Analysis	84
6.4 Discussion about TGA Slope Changes.....	89
6.5 High Temperature Investigation for LCMO5 and LSMO Series	90
7. CONCLUSION & FUTURE RECOMMENDATIONS.....	93
7.1 Conclusion	93
7.2 Future Recommendations	94
8. REFERENCES.....	95

LIST OF TABLES

TABLES

Table 1: Change of Mn valence state with respect to Sr doping amount	11
Table 2: Most significant Kröger-Vink notations.....	17
Table 3: The amount of chemicals needed for the preparation of LSMO solutions .	36
Table 4: 2 θ values of LSMO series	43
Table 5: Amount of Ca by experimental study and theoretical calculation	43
Table 6: Slope changes from LMO to LSMO2	89
Table 7: Slope changes from LSMO4 to SMO	89

LIST OF FIGURES

FIGURES

Figure 1: Schematic view of manganite [7]	2
Figure 2: A site cations (red) with 12-fold oxygen ion coordination(a) and B site cations (yellow) with 6-fold oxygen ion coordination(b)	6
Figure 3: Schematic view of Jahn-Teller distortion on perovskites ((a) and (b))	7
Figure 4: Schematic of basic manganite structure	10
Figure 5: Electronic phase diagram of LSMO ($0 < x < 0.6$)	12
Figure 6: Electronic phase diagram of LCMO	13
Figure 7: Subtracting the ideal structure (middle) from the real structure (left-hand)	15
Figure 8: Oxygen vacancy formation upon heating and exposure to reducing atmosphere in fluorite structure results in chemical expansion [70].....	20
Figure 9: Asymmetric (a) and symmetric (b) potential energy vs. interatomic distance diagrams [72]	21
Figure 10: Thermal and chemical expansions as a function of temperature [76]	23
Figure 11: Effect of time on reaction products [89].....	25
Figure 12: Processing route of Pechini method [91].....	26
Figure 13: Schematic solution combustion synthesis route [95].....	27
Figure 14: Production routes of various types of final products by sol-gel method .	30
Figure 15: Structure of EXSTAR TG/DTA 7300	34
Figure 16: Flowchart of Pechini Method	38
Figure 17: XRD Spectra of LCMO5	40
Figure 18: XRD Spectras of LSMO Series	41
Figure 19: (004) and (220) reflections for tetragonal and (024) reflection for rhombohedral crystal structures	42

Figure 20: Amount of Sr by experimental studies and theoretical calculations.....	44
Figure 21: The percent weight loss versus temperature plot.....	46
Figure 22: The percent strain as a function of temperature.....	47
Figure 23: The relationship between α_{Chem} and δ in LCMO5	48
Figure 24: a_0 change with respect to temperature	49
Figure 25: b_0 change with respect to temperature	49
Figure 26: c_0 change with respect to temperature	50
Figure 27: SEM images of a. LCMO5- Sintered b. LCMO5-After Treatment (1000x)	50
Figure 28: The percent weight loss versus temperature plot of LMO.....	53
Figure 29: The percent weight loss versus temperature plot of LSMO1	54
Figure 30: The percent weight loss versus temperature plot of LSMO2	55
Figure 31: The percent weight loss versus temperature plot of LSMO3	56
Figure 32: The percent weight loss versus temperature plot of LSMO4	57
Figure 33: The percent weight loss versus temperature plot of LSMO5	57
Figure 34: The percent weight loss versus temperature plot of LSMO6	58
Figure 35: The percent weight loss versus temperature plot of LSMO7	59
Figure 36: The percent weight loss versus temperature plot of LSMO8	60
Figure 37: The percent weight loss versus temperature plot of LSMO9	61
Figure 38: The percent weight loss versus temperature plot of SMO.....	62
Figure 39: a_0 change with respect to temperature in LMO	63
Figure 40: c_0 change with respect to temperature in LMO	63
Figure 41: The relationship between α_{Chem} and δ in LMO	64
Figure 42: a_0 change with respect to temperature in LSMO1	65
Figure 43: c_0 change with respect to temperature in LSMO1	65
Figure 44: The relationship between α_{Chem} and δ in LSMO1.....	66
Figure 45: a_0 change with respect to temperature in LSMO2	67
Figure 46: c_0 change with respect to temperature in LSMO2	67
Figure 47: The relationship between α_{Chem} and δ in LSMO2.....	68

Figure 48: a_0 change with respect to temperature in LSMO3	69
Figure 49: c_0 change with respect to temperature in LSMO3	69
Figure 50: The relationship between α_{Chem} and δ in LSMO3	70
Figure 51: a_0 change with respect to temperature in LSMO4	70
Figure 52: c_0 change with respect to temperature in LSMO4	71
Figure 53: The relationship between α_{Chem} and δ in LSMO4	71
Figure 54: a_0 change with respect to temperature in LSMO5	72
Figure 55: c_0 change with respect to temperature in LSMO5	73
Figure 56: The relationship between α_{Chem} and δ in LSMO5	73
Figure 57: a_0 change with respect to temperature in LSMO6	74
Figure 58: c_0 change with respect to temperature in LSMO6	75
Figure 59: The relationship between α_{Chem} and δ in LSMO6	75
Figure 60: a_0 change with respect to temperature in LSMO7	76
Figure 61: c_0 change with respect to temperature in LSMO7	77
Figure 62: The relationship between α_{Chem} and δ in LSMO7	77
Figure 63: a_0 change with respect to temperature in LSMO8	78
Figure 64: c_0 change with respect to temperature in LSMO8	79
Figure 65: The relationship between α_{Chem} and δ in LSMO8	80
Figure 66: a_0 change with respect to temperature in LSMO9	80
Figure 67: c_0 change with respect to temperature in LSMO9	81
Figure 68: The relationship between α_{Chem} and δ in LSMO9	81
Figure 69: a_0 change with respect to temperature in SMO	82
Figure 70: c_0 change with respect to temperature in SMO	83
Figure 71: The relationship between α_{Chem} and δ in SMO	83
Figure 72: SEM images of a. LMO-As synthesized b. LMO-After experiment.....	84
Figure 73: SEM images of a.LSMO2-As synthesized b.LSMO2-After experiment	85
Figure 74: SEM images of a. LSMO4-As synthesized b. LSMO4-After experiment c. LSMO5-As synthesized d. LSMO5-After experiment e. LSMO6-As synthesized b. LSMO6-After experiment.....	86

Figure 75: SEM images of a. LSMO7-As synthesized b. LSMO7-After experiment c. LSMO8-As synthesized d. LSMO8-After experiment.....	87
Figure 76: SEM images of a. LSMO9-As synthesized b. LSMO9-After experiment c. SMO-As synthesized d. SMO-After experiment.....	88
Figure 77: δ with respect to Sr %	91
Figure 78: α_{Chem} changes with respect to Sr %	92

NOMENCLATURE

CTE	: Coefficient of Thermal Expansion
CMR	: Colossal Magnetoresistance
DTA	: Differential Thermal Analysis
EDS	: Energy Dispersive X-ray Spectroscopy
HTXRD	: High Temperature X-Ray Diffraction
δ	: Oxygen Deficiency
RE	: Rare-earth Elements
SEM	: Scanning Electron Microscope
SOFC	: Solid Oxide Fuel Cell
TGA	: Thermogravimetric Analysis
XRD	: X-Ray Diffraction
LCMO5	: $\text{La}_{0.5}\text{Ca}_{0.5}\text{MnO}_{3-\delta}$
LSMO_x	: $\text{La}_{1-x}\text{Sr}_x\text{MnO}_{3-\delta}$

CHAPTER 1

INTRODUCTION

Manganites take great interests is many applications due to their excellent properties such as colossal magnetoresistance (CMR) [1], multiferroic effects [2] and high mixed ionic and electrical conductivity [3]. These properties make them suitable candidates for electronic devices and industrial applications in energy field [4, 5].

ABO_3 is the chemical formula of perovskite materials where A and B are metal cations and O is nonmetallic anion respectively. In perovskite system, A is larger metallic cation and radius of A is close to radius of O^{2-} . B is a smaller metallic cation creating octahedral coordinates with oxygen atoms. In Figure 1, the rare-earth elements placed in A site and B site filled with 3d transition element, manganese. In normal perovskite cubic structures, and, A and B atoms have 3+ valence states as illustrated in Figure 1. However, by doping divalent cation in B site, the structure can be distorted. Jahn & Teller effect, cation size mismatch and double exchange cause change of structure in order to lower the free energy of the system. Moreover, the electrical properties are altered by interaction of many mechanisms such as Jahn & Teller effect, double exchange concept, spin ordering and charge states [6].

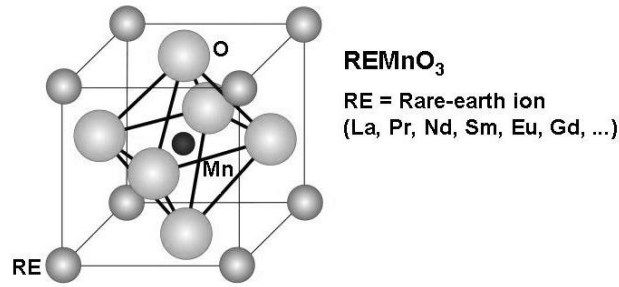


Figure 1: Schematic view of manganite [7]

Manganites employed as cathode of solid oxide fuel cells (SOFCs), oxygen permeation membranes and gas conversion/reformation catalysis [8, 9, 10, 11]. Under high temperature and low oxygen partial pressure (pO_2), which is a typical operating environment of SOFCs, these materials have ability to undergo thermal and chemical expansion due to the asymmetry of the potential energy versus interatomic distance curve and process competition [12]. Formation of oxygen vacancy create lattice contraction due to electronic effects. Size of the O vacancy in the non-stoichiometric oxide lattice is determined as a result of interaction between positively charged O vacancy and the neighboring ions. During this process, some cations are reduced in order to maintain charged neutrality in the crystal. Increase of cation radius change leads to lattice expansion. These two competing processes determine the sign and magnitude of the chemical expansion [13].

Chemical expansion creates significant change in crystalline lattice and eventually leads to catastrophic stresses and strains. For example, under large oxygen partial pressure gradient, chemical expansion leads to cracking of Ceria (CeO_2) membranes [14, 15, 16]. Also it is suspected that deviation from thermodynamic equilibrium and electronic properties result from chemical expansion [17, 18].

$La_{1-x}Sr_xMnO_{3-\delta}$ (LSMO), where ($x= 0, 0.1, 0.2, 0.3, 0.4, 0.5, 0.6, 0.7, 0.8, 0.9, 1$), and $La_{1-x}Ca_{1-x}MnO_{3-\delta}$ (LCMO) where ($x= 0.5$) are primarily used in magnetic storage

systems because of their electrical properties. These materials have also been investigated as a cathode materials in SOFCs [8, 9, 10, 11]. The doping of Sr and Ca makes electronic conductivity possible due to thermally activated hopping process of small polarons [19]. With ionic conductivity, LSMO and LCMO are called mixed ionic and electronic materials. The amount of doping of Sr and Ca increases the oxygen semi-permeation and decrease reactivity of LSMO and LCMO in the electrolyte [20], as well.

Various synthesis techniques involving solid state reaction [21], Pechini method [22], solution combustion [23], hydrothermal synthesis [24], co-precipitation [25] and sol-gel have been applied to synthesize bulk manganites. Pechini method offers scientists to produce, homogeneity, low temperature processing, nanocrystalline phases and high purity. The value of chemical expansion seems to be accurate and realistic because of gathering high surface area with Pechini method [26].

In this study, the chemical expansion of manganites, LCMO and LSMO, were explored in details. Within the frame of this study, Pechini sol-gel synthesized powder were characterized by X-ray Powder Diffraction (XRD), Scanning Electron Microscope (SEM) and Energy Dispersive X-ray Spectroscopy (EDS). Thermogravimetric Analysis (TGA), Dilatometry and High Temperature X-ray Powder Diffraction (HTXRD) were used complementarily to evaluate chemical expansion accurately, understand the underlying mechanisms of expansion and propose ways to stabilize the expansion for a safe operation of SOFCs and other devices.

CHAPTER 2

LITERATURE REVIEW

2.1 Perovskites

Many engineering ceramics are in the form of perovskite crystal structure [27]. Attributed primarily to its unique electronic, optical and chemical properties, perovskites have been used widely in various important applications such as SOFCs, piezoelectric sensors and thermoelectric devices [5, 28, 29]. Perovskite structure has been attracted much attention because almost all periodic table elements have flexibility to adjust itself to perovskite and distort the lattice. This is because perovskites have various properties such as electric, electronic, optical and chemical [27].

In the following sections, properties and examples of perovskites will be presented.

2.1.1 Crystal Structure of Perovskites

Crystal structure of perovskites is represented as ABX_3 . X represents generally oxygen but there are some other cases where X can be F^- and Cl^- . In ABO_3 , A and B atoms are positively charged ions. The ionic radius of A atom is larger than ionic radius of B. Three O^{2-} anions and A cation forms mixed fcc packing which is the basis of crystal structure of ABO_3 . In Figure 2, larger A cations are coordinated 12 fold cuboctahedrally with O^{2-} anions and small B cations are coordinated

octahedrally with O^{2-} anions. The crystal structure of ideal ABO_3 is cubic however, because of the distortions, orthorhombic and tetragonal bravais lattices can be formed [6]. Jahn-Teller effects, size effects and deviation from ABO_3 compositions are three main effect of distortions in lattice [27].

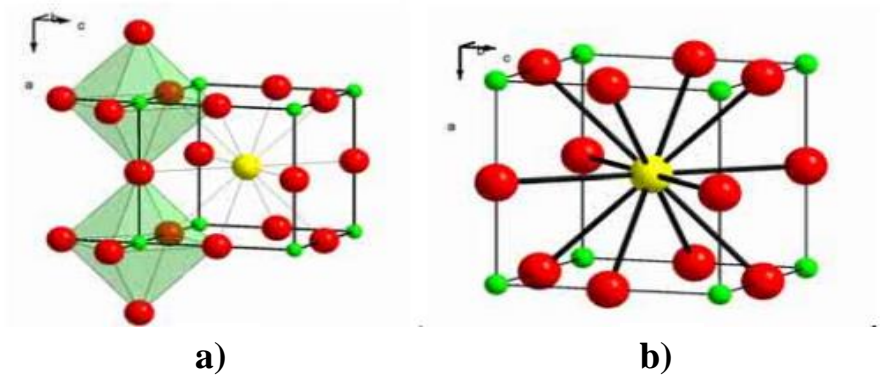


Figure 2: A site cations (red) with 12-fold oxygen ion coordination(a) and B site cations (yellow) with 6-fold oxygen ion coordination(b)

2.1.2 Distortions in Perovskites

Jahn-Teller effects, size effects and deviation from compositions are three main reasons of distortions in lattice.

2.1.2.1 Jahn-Teller Effects

Jahn-Teller effects are described as reducing symmetry and energy of non-linear molecule system by geometric distortion [30]. In other words, when a molecule has orbital degeneracy and degenerate electrons involve the binding of molecule, the forces which tend to destroy symmetry of system become significant [30]. Electronic state of the system is important parameter for Jahn-Teller effects. Commonly, this type of distortions is seen in octahedral complexes [31, 32]. B atoms in perovskites

coordinated as octahedrally with oxygen ions. That is why it is seen mostly in perovskite structures. For example, in LaMnO_3 with Mn^{3+} ions $3d^4$ electrons divided into 3 t_g and 1 e_g electron. Odd numbers of e_g electron creates an elongation in $[\text{MnO}_6]$ octahedron and distortion made up called as Jahn-Teller distortion [27, 33]. Figure 3 demonstrates the schematic view of Jahn-Teller distortion in LaMnO_3 .

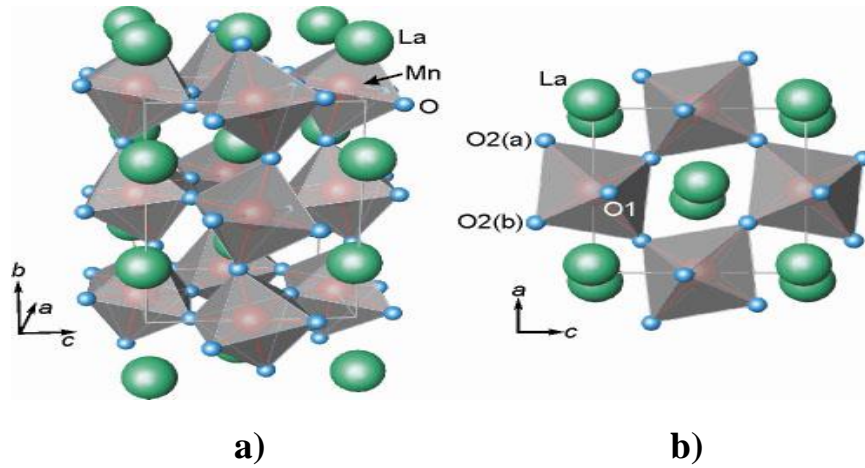


Figure 3: Schematic view of Jahn-Teller distortion on perovskites ((a) and (b))

2.1.2.2 Size Effects

In ideal cubic perovskite, the lattice parameter is directly related with ionic radius, Goldschmidt presented tolerance factor (t) in order to estimate the amount of distortion as given in Equation 1 [34].

$$t = \frac{(r_A + r_O)}{\sqrt{2}(r_B + r_O)} \quad \text{Equation 1}$$

where r_A , r_B and r_O are ionic radius of atoms in perovskite structures. It can be seen that, the change in ionic radius of A results in a decrease of tolerance factor. If t is smaller than one the $[\text{BO}_6]$ octahedra will tilt to cover empty space and symmetry will be reduced. Large A ions with small B ions yield with tolerance factor higher than one. In that case, close packed layers are stacked as hexagonal but not cubical.

Goldschmidt tolerance factor gives accurate results when structure is purely ionic since perovskites are not truly ionic. Thus, in perovskites, tolerance factor can not be estimated accurately [34].

2.1.2.3 Deviations from ABO₃ Compositions

Under reducing or oxidizing environments, formation of oxygen vacancies lead to change in valence state of B ions [35]. With double valence states, the oxygen vacancies can be ordered and this results in distortion of structure [36]. Also, doping with another C element deviates from ABO₃ to (A_{1-x}C_x)BO₃. The change in radius of A sites and double valence states in B sites deviate less symmetrical structure due to the mutual charge of ions from their original positions within the stable cubic structure [35].

2.1.3 Examples of Distorted Perovskites

As it is mentioned previously that with no distortions, perovskite structure is cubic. It is previously reported that orthorhombic, tetragonal, hexagonal, rhombohedral and monoclinic structures have been seen as distorted perovskites [37, 38, 39]. Distortions affect several properties of materials in perovskites. For examples,

- I. PbVO₃ is tetragonally distorted from cubic structure and it shows unusual VO₅ pyramids instead of VO₆ octahedrons. PbVO₃ is a semiconductor which have $\rho(T)$ dependence down to 2 K [37].
- II. La_{1-x}Sr_xCoO_{3- δ} ($x= 0 \leq x \leq 0.8$) has different crystal structures depending on x value. Values larger than 0.5 shows long range cubic perovskite symmetry and values lower than 0.5 show rhombohedrally distorted perovskite. At x=0.7 value, ideal cubic structure is attained. The change in structure directly affects the ionic conductivity [38].

III. BiMnO_3 has monoclinically distorted perovskite crystal structure. These distortions bring both ferroelectric and ferromagnetic properties. It also demonstrates magnetodielectric anomaly temperature close to the ferromagnetic transition [39].

These examples clearly reveal that the alteration of structure with distortions results in remarkable change in behaviour of materials. Most of the distorted perovskites structures have unique properties.

2.2 Manganites

Manganites are type of manganese oxides having mixed valence states with perovskite structure represented as $\text{Ln}_{1-x}\text{A}_x\text{MnO}_3$ (Ln= rare-earth cation, A= alkaline earth cation) in Figure 4. They have been widely investigated in the literature as because they exhibit a rich variety of crystallographic, magnetic and electronic phases [40]. The current researchs on manganites are originated from a phenomenon so called colossal magnetoresistance (CMR) [4, 41]. New physical concepts were presented such as Jahn-Teller polaron and double exchange theory while studying CMR on manganites [42, 43]. There are several research areas where manganites are seen as potential engineering materials [5, 11, 20]. One example can be shown as cathode materials used in SOFCs [20]. The cathode materials should be stable under oxidizing and reducing environments, and they should have ionic conductivity and sufficient catalytic activity in order to reduce oxygen under operating conditions [44]. Manganites perform effectively under operating environment of SOFCs as a cathode material [5].

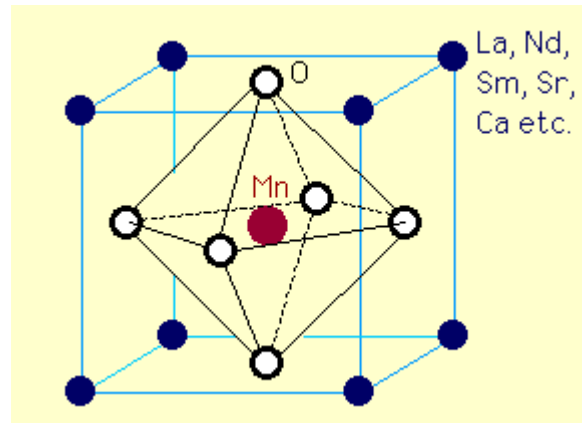


Figure 4: Schematic of basic manganite structure

As previously mentioned before $\text{Ln}_{1-x}\text{A}_x\text{MnO}_3$ has perovskite structure. Rare-earth (RE) cation (Ln) and alkaline earth cation (A) occupy in A site of perovskite. Manganese occupies B site of perovskite and has multi valence such as Mn^{3+} and Mn^{4+} . The replacement of rare-earth cation by divalent alkaline earth cation results with distortion of perovskite structure due to Jahn & Teller effect and cation radius change. The crystal structure of distorted perovskites are orthorhombic, hexagonal, monoclinic and rhombohedral [6]. $\text{La}_{1-x}\text{Sr}_x\text{MnO}_{3-\delta}$ and $\text{La}_{1-x}\text{Ca}_x\text{MnO}_{3-\delta}$ are among the other potential candidates for cathode materials of SOFCs.

2.2.1 $\text{La}_{1-x}\text{Sr}_x\text{MnO}_{3-\delta}$

$\text{La}_{1-x}\text{Sr}_x\text{MnO}_{3-\delta}$ (LSMO), where ($x = 0, 0.1, 0.2, 0.3, 0.4, 0.5, 0.6, 0.7, 0.8, 0.9, 1$) have different properties with respect to amount of Sr dopant in the structure [25]. The ionic radii of La and Sr are calculated as 117.2 pm and 132 pm, respectively [45]. A site filled with La is doped with Sr having relatively larger radius. The amount of Sr dopant leads to change in manganese (Mn) valence state by creating a mixed valence state in order to preserve charge neutrality. This is because trivalent La is doped with divalent Sr [46]. Table 1 shows the Mn valence state when Sr

doping occurs. When A site is filled with Sr only, the valence state of Mn is +4 whereas in LaMnO_3 , the valence state of Mn is +3.

The relative percentages of the Mn^{4+} and Mn^{3+} are determined by strontium doping and oxygen vacancies of the system. LMO demonstrates strong Jahn-Teller effect and increasing Sr doping changes this effect [47, 48].

Table 1: Change of Mn valence state with respect to Sr doping amount

Doping Amount (x)	Mn Valence State	Amount of Mn^{3+} and Mn^{4+}
0	3+	100 % 3+
0.1	3.1+	90% 3+ and 10% 4+
0.2	3.2+	80% 3+ and 20% 4+
0.3	3.3+	70% 3+ and 30% 4+
0.4	3.4+	60% 3+ and 40% 4+
0.5	3.5+	50% 3+ and 50% 4+
0.6	3.6+	40% 3+ and 60% 4+
0.7	3.7+	30% 3+ and 70% 4+
0.8	3.8+	20% 3+ and 80% 4+
0.9	3.9+	10% 3+ and 90% 4+
1	4+	100% 4+

LMO, LSMO1, LSMO2, LSMO3, LSMO4, LSMO5, LSMO6, LSMO7, LSMO8, LSMO9 and SMO are different materials. This results in different material properties. At room temperature, various crystal structures of stoichiometric and non-stoichiometric LMO was reported such as cubic, orthorhombic and monoclinic [6, 49, 50, 51]. Depending on the synthesis method, LSMO1 has orthorhombic and

rhombohedral crystal structures [6, 49, 50]. Between $0.2 \leq x \leq 0.5$, mostly rhombohedral phases are observed however, some authors reported cubic structure for LSMO4 and LSMO5 [6, 49, 50, 51] as well. In the range of $0.6 \leq x \leq 0.8$, tetragonal structures are reported [49]. LSMO9 is mostly reported in hexagonal form [52]. For SMO, cubic, orthorhombic and hexagonal structures depending on final sintering temperature and oxygen stoichiometry, were detected [49, 53]. The magnetic and electrical properties of LSMO series change with Sr dopant addition. The electronic phase diagram of LSMO is illustrated in Figure 5. At room temperature, up to $x < 0.15$ region, paramagnetic insulator behaviour is reported. On the other hand, $x > 0.15$ range, the materials behave as a ferromagnetic metal [50].

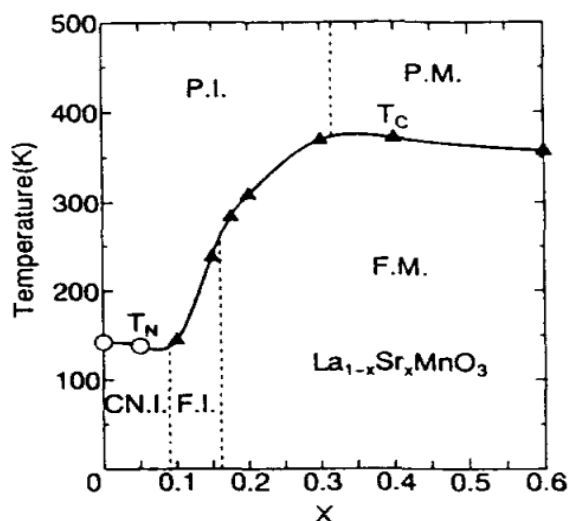


Figure 5: Electronic phase diagram of LSMO ($0 < x < 0.6$)

2.2.2 $\text{La}_{1-x}\text{Ca}_x\text{MnO}_{3-\delta}$

In Calcium (Ca) doping, just in the case of LSMO, different structures are formed and increasing the Ca doping amount results in different properties [54]. Ca is alkaline earth metal having 2+ valence state. Lanthanum (La) is substituted by Ca

having an ionic radius of 114 pm [45]. As a result of substitution, the crystal structure of $\text{La}_{1-x}\text{Ca}_x\text{MnO}_{3-\delta}$ (LCMO) contracts due to substituted Ca having smaller radius than La ion. Like LSMO, amount of Ca doping results change in valence state of Mn due to preserve charge neutrality [46]. Table 1 is also valid for LCMO.

The doping by Ca changes the crystal structure of LCMO series. The Ca doped lanthanum manganites, the phase composition could be rather complex. From neutron diffraction data at 80K, LMO has monoclinic, LCMO2 and LCMO4 have rhombohedral, and LCMO6 and LCMO8 have tetragonal crystal structures, respectively. The intermediate phases have crystal structure mixing of two neighbouring phases [55]. For CMO, more than 15 intermediate phases were found between CaMnO_3 and $\text{Ca}_2\text{Mn}_2\text{O}_5$ [56]. For LCMO5, the structure found as orthorhombically distorted perovskite structure with Pnma space group [57].

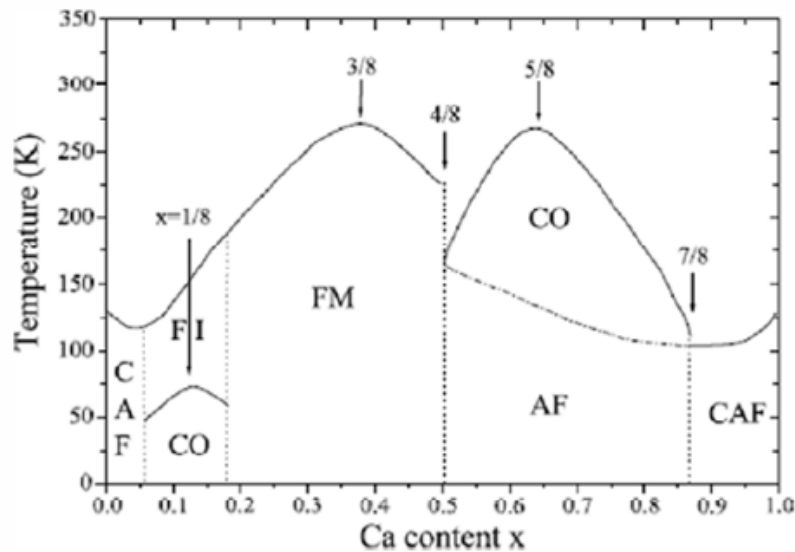


Figure 6: Electronic phase diagram of LCMO

In Figure 6, the electronic structure of LCMO series are illustrated. The doping with Ca changes the electronic structure of LCMO materials. LMO and CMO are anti-

ferromagnetic insulators. In the range of $0.06 \leq x \leq 0.18$, ferromagnetic insulator behaviors were observed in ground state. Between 0.18 and 0.50, in ground state, ferromagnetic metal behaviour was seen. Above 0.5 doping amount, charge ordering and anti-ferromagnetic spin ordering were observed simultaneously [58].

2.3 Defect Chemistry

In perfect crystals, atoms and structural units were located in structures where all lattice points were occupied. Scientists believed that the synthesized inorganic materials have exact stoichiometric compounds. However, in real life, synthesizing and creating perfect crystal is almost impossible. It was shown by Schottky and Wagner that crystal structures of inorganic materials are not perfect and ideal [59]. There might be vacancies and also interstitial atoms between lattice sites. Although it is accepted that under equilibrium conditions, exact stoichiometry can be gained there will be always deviation from stoichiometry and crystal structure due to defects at non-equilibrium conditions. Crystalline solids have different types of structural defects. If a defect is presented in lattice site it is called point defects (i.e. vacancies, interstitial and substitutional atoms). Line and plane defects are also presented into the compound. Dislocations are line defects and grain boundaries, stacking faults and surfaces are plane defects. Defect chemistry is expressed as investigating point defects and their interactions in solid state .

2.3.1 Point Defects

The main role of point defects are formed from interstitial and substitutional atoms and vacancies. The isolated area of lattice is affected by point defects.

In Figure 7, the lefthand column demonstrates the actual and middle column shows the perfect structure. The subtraction of these two columns gives us defects presented in the actual structure. Figure 7 is illustrated the four major mechanisms generating point defects. The remained defects identify the behavior of the system [60].

In Figure 7-a, water molecules are demonstrated and the remaining defects are extra proton and missing proton (proton vacancy). The missing proton makes up system negatively charged whereas the extra proton produces a positive charge. Eventually, total charge will be zero. In Figure 7-b, typical AgCl solid substance is illustrated and in perfect AgCl phase, the lattice points are fixed. However in actual AgCl, some Ag^+ ions have left their fixed lattice sites to occupy interstitial positions. The number of Ag^+ ions determines how many vacancies are formed. This mechanism is called Frenkel defect [61].

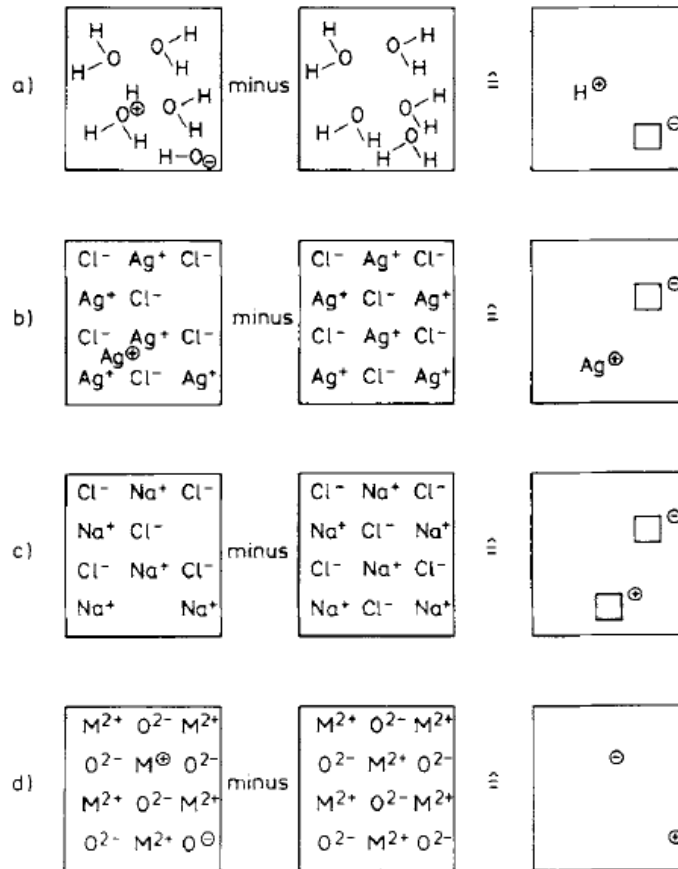


Figure 7: Subtracting the ideal structure (middle) from the real structure (left-hand)

In Figure 7-c, in closed pack alkali metal halides, Schottky defects are observed. Both positive and negative charged ions were released from crystal structures. The vacancies change their signs when release of ions. In Figure 7-d, the atoms in crystal structure are in fixed positions. Without changing their lattice positions, the charge of atoms can be altered. In this mechanism, formation of one extra electron are neutralized by formation of one electron hole. This mechanism presents electronic conductivity and creates mixed ionic and electronic conductive compounds. Above four defect mechanisms, some requirements should be maintained. Charge neutrality and mass have to be preserved and the lattice sites must be balanced. The first three mechanisms represent the ionic defects formed by vacancies, interstitials and impurities whereas last mechanism demonstrates electronic defects resulting from change in orbital state of valence electrons [60].

2.3.2 Notation in Defect Chemistry

Some notations were developed by Kröger-Vink to demonstrate changes in defect chemistry. Table 2 shows the Kröger-Vink notations used in defect chemistry. Assume M is cation and X is anion. In Kröger-Vink notations, “.” (dot) means positive charge and “ ‘ ” (prime) means negative charge. Amount of dots and primes represents the negativity or positivity of the ions. X written as superscript means neutral site [62].

2.3.3 Non-Stoichiometry in Metal Oxides

Presence of point defects and their aggregates are directly involved in forming of non-stoichiometry in substances. Metal oxides might have excess or deficit metal and oxygen. These non-stoichiometry results from the temperature, chemical potentials of elements, properties of metal oxides themselves. In that manner, four main non-stoichiometric metal oxides exist [63].

Table 2: Most significant Kröger-Vink notations

M cation in normal cation site	M_m
X anion in normal anion site	X_x
Foreign cation on normal cation site	M_{fm}
Foreign cation on interstitial site	M_{fi}
Foreign Cation	M_f
M element as interstitial	M_i
X element as interstitial	X_i
Vacant interstitial site	V_i
Vacancy of M element	V_m
Vacancy of X element	V_x
Zero effective charge cation and anion	M_M^x and X_X^x
Charged cation and anion vacancy	V_M'' and $V_X\ddot{}$
Charged cation and anion interstitial	$M_i\dot{}$ and X_i''
Zero effective charge cation and anion vacancies	V_M^x and V_X^x
Electrons and holes	e' and $h\cdot$

- i. Metal deficient oxides ($M_{1-\delta}O$) are p-type conductors and conduction occurs due to holes. Majority of the defects are metal vacancies.
- ii. Metal excess oxides ($M_{1+\delta}O$) are typical n-type conductors and conduction occurs owing to transport of electrons. Quasi-free electrons can be created by formation of extra charge ion. Metal interstitials are prevalent defects.
- iii. Oxygen excess oxides ($MO_{2+\delta}$) are p-type conductors. Oxygen interstitials defects prevale.

- iv. Oxygen deficient oxides ($\text{MO}_{2-\delta}$) oxygen vacancies dominate. Due to defect reactions, formation of electrons or reduction of metal ions might be observed.

2.3.4 Defects Related Properties

Defects determine several major physical and chemical properties of materials. In solid materials, presence of defects plays significant role in lattice diffusion mechanisms. The grain boundaries, dislocations and interfaces increases the mechanical properties of solids. Also, these two dimensional defects affect transport properties. Electronic and magnetic properties are determined by electronic defects in solids, as well.

As an example, point defects in manganites are originated from aliovalent cation doping and oxygen non-stoichiometry. The doping affects the structural properties and changes goldschmidt tolerance factor [35]. Doping also alters the electronic properties of solid materials. The oxygen non-stoichiometry changes the electronic properties of manganites such as curie temperature, electric behavior and magnetoresistance response [64].

Another example is $\text{YBa}_2\text{Cu}_3\text{O}_{7-\delta}$ (YBCO) providing significant information about effects of oxygen non-stoichiometry. The changes of oxygen deficiency (δ) between 0 and 1 results with structural and also electronic properties change. If δ is smaller than 0.65 superconductivity is observed. At higher δ values, the compound become semi-conductor [65]. Among material properties which is affected by defects and their interactions, chemical expansion is one of the most significant properties where lattice diffusion is a crucial parameter [5].

2.4 Chemical Expansion

Chemical expansion is often referred to defect-induced expansion or chemical strain in solid materials [66, 67]. In fact , chemical expansion results from two competing

processes namely as: cation radius change and formation oxygen vacancy. At low oxygen partial pressures (pO_2) and relatively high temperatures, losses of lattice oxygen is inevitable process because of large oxygen chemical potential gradient between lattice and outside atmosphere. This loss of lattice oxygen means creation of oxygen vacancy. With this, oxidation states of cations change to maintain charge neutrality. As a result of these processes, chemical expansion in lattice occurs [68]. In other words, cation radius change means that reducing cation has larger radius than unreduced state thus, the lattice expands upon this process. Because of the electrostatic charges of oxygen vacancies, repulsion of surrounding atoms are inevitable. Oxygen vacancies behave as positively charged particles and repel surrounding cations and the reduced cations have negative charge that repels surrounding oxygen atoms. Due to these mechanisms, chemical expansion occurs at the lattice. In some systems such as in ceria, chemical expansion value can be determined from the interaction of defects [69].

In perovskites, during oxygen vacancy formation, B cation is reduced to lower valence state [46]. Figure 8 is represented the chemical expansion and it can be expressed as defect reaction in perovskites given in Equation 2.



This is the overall reaction demonstrating chemical expansion where B_B^X , O_O^X , $V_O^{\cdot\cdot}$ and B_B' are B atoms in B sites, oxygen on oxygen sites, oxygen vacancy with net positive charge of 2+ with respect to lattice and reduced B atoms in B site.

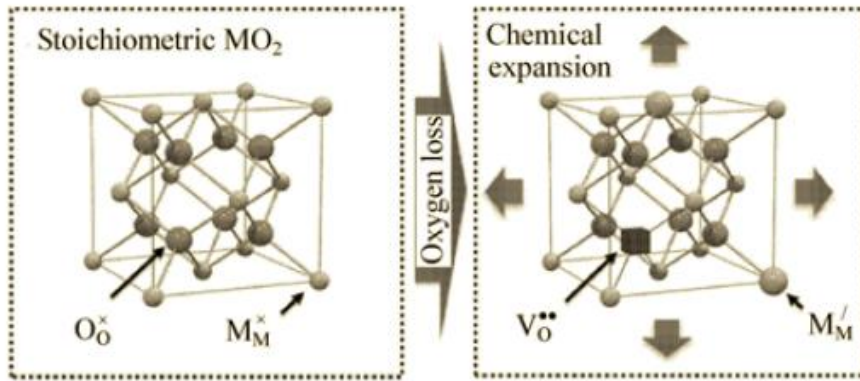


Figure 8: Oxygen vacancy formation upon heating and exposure to reducing atmosphere in fluorite structure results in chemical expansion [70]

$$\varepsilon = \frac{\Delta l}{l_0} = \alpha_{Chem} * \Delta\delta \quad \text{Equation 3}$$

As a result of chemical expansion, strain occurs between lattices. These strains can be classified as microstrains given in Equation 3 where Δl , l_0 , ε , $\Delta\delta$ and α_{Chem} are length change, initial length of sample, chemical strain, oxygen deficiency change and coefficient of chemical expansion, respectively.

Chemical strain can be found by multiplying the coefficient of chemical expansion with change in oxygen deficiency ($\Delta\delta$) [70].

Chemical expansion in compounds have been observed at relatively high temperatures because kinetics of oxygen vacancy formation is not allowed to release oxygens at lower temperatures. Reduction of cations do not occur at low temperatures. Under reducing atmosphere, the oxygen vacancy formation is inevitable because of the chemical potential gradient [71]. Thermal expansion causes the lattice expansion at all temperatures. When chemical expansion is calculated, total expansion is found and then subtracted from thermal expansion value. It also should be noted that at low temperatures because of stated reasons, chemical expansion are not seen so only thermal expansion has to be considered [70].

2.4.1 Thermal Expansion

Thermal expansion is the increase of the average distance between atoms with the increase of temperature at constant pressure. Potential energy vs. interatomic distance diagram should be drawn in order to understand thermal expansion better [72].

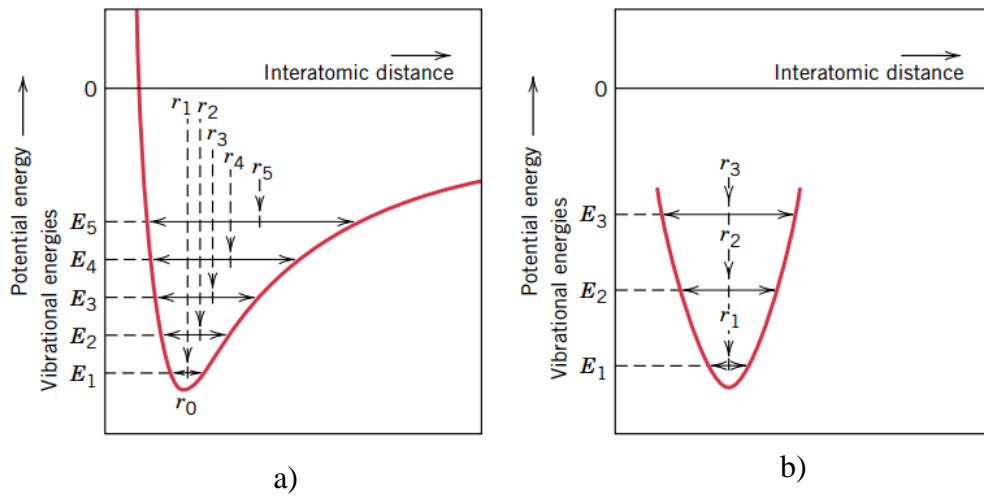


Figure 9: Asymmetric (a) and symmetric (b) potential energy vs. interatomic distance diagrams [72]

Figure 9-a and Figure 9-b illustrate the asymmetric and symmetric behaviour of potential energy with respect to interatomic distance. The heating of substance results in increasing vibrational energy of atoms. However, not every increase of vibration energy causes thermal expansion. In order to detect that, there should be net change in the interatomic separation. Figure X b demonstrates that if the potential energy curve is symmetric during heating there is no thermal expansion observed [73]. Thermal expansion is expressed as uniaxial strain with Equation 4.

$$\varepsilon = \frac{\Delta l}{l_0} = \alpha_{Them} * \Delta T \quad \text{Equation 4}$$

where ΔT and α_{Them} are temperature gradient and coefficient of chemical expansion. Normally, coefficient of thermal expansion (CTE) increases with an increase in temperature. However, between temperature change and thermal strain, CTE is independent of temperature. There are significant differences between thermal expansion and chemical expansion [72].

The most significant difference is that chemical expansion is irreversible process so that after high temperature and reducing atmosphere conditions, the compounds will stay with most of the defects that already caused the chemical expansion [74]. It should be noted that thermal expansion occurs almost all temperature regime however, due to oxygen vacancy formation mechanism, chemical expansion is observed relatively at high temperature [75]. The reducing atmosphere creates chemical potential gradient favors oxygen vacancy formation and it results in chemical expansion. As it was stated previously that thermal expansion does not depend on temperature however, chemical expansion changes with the temperature due to increase oxygen vacancies at higher temperatures.

Figure 10 illustrates the thermal and chemical expansions as a function of temperature. As it can be seen strong deviation that at high temperature CTE is much more higher than low temperature CTE. This increase can be related to chemical expansion [76]. Chemical expansion is the difference between the undoped ceria having no chemical expansion and powder praseodymium (Pr) doped ceria.

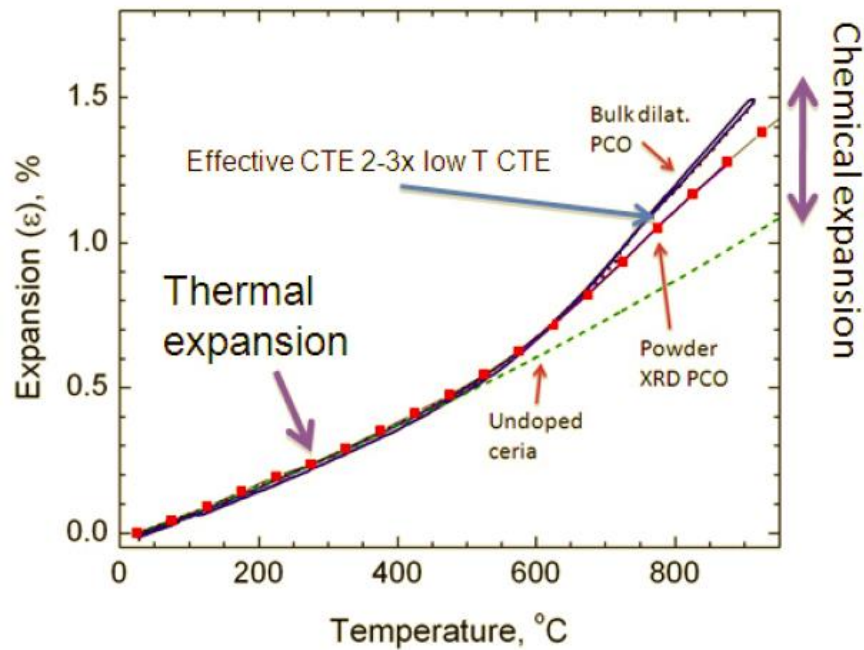


Figure 10: Thermal and chemical expansions as a function of temperature [76]

2.4.2 Problems Arising from Chemical Expansion

As previously stated, chemical expansion has been generally observed in materials performed under high temperatures and low oxygen partial pressures. SOFCs, oxygen permeation membranes and three way catalysis have these type of operating conditions [8, 9, 10, 11]. Under severe atmospheres, chemical expansion leads to decrease in mechanical, electrical and chemical properties of compounds.

Formation of cracks in cerium oxide membranes have been observed due to chemical expansion [14, 77, 78]. Also, it is observed that in some cases modulus of elasticity and strength of interatomic bonds decreases due to an increase in oxygen vacancy [79]. Whether or not chemical expansion leads to an increase in ionic conductivity at highly strained heterostructure films has not been clarified yet in the literature [80].

2.4.3 Examples of Chemical Expansion

The $\text{La}_{0.6}\text{Sr}_{0.4}\text{Co}_{0.2}\text{Fe}_{0.8}\text{O}_{3-\delta}$ is investigated by Adler and α_{Chem} is found out to be 0.032 in the temperature range between 700 °C and 890 °C [81]. In addition, Bishop et al. report α_{Chem} of $\text{La}_{0.597}\text{Sr}_{0.398}\text{Co}_{0.2}\text{Fe}_{0.8}\text{O}_{3-\delta}$ as 0.031 between 700 °C and 900 °C [75]. Wang et al. state that α_{Chem} of $\text{La}_{0.6}\text{Sr}_{0.4}\text{Co}_{0.8}\text{Fe}_{0.2}\text{O}_{3-\delta}$ is 0.022 at 800 °C [82]. It is reported by Chen et al. that α_{Chem} for $\text{La}_{1-x}\text{Sr}_x\text{CoO}_{3-\delta}$ takes values between 0.023 and 0.024 while x parameter and the temperature vary from 0.2 to 0.7 and from 600 °C up to 900 °C, respectively [83]. McIntosh et al. study $\text{Ba}_{0.6}\text{Sr}_{0.4}\text{Co}_{0.8}\text{Fe}_{0.2}\text{O}_{3-\delta}$ composition between 600 °C and 900 °C. Then, they report that the obtained α_{Chem} values are between 0.026 and 0.016 [84]. Miyoshi et al. demonstrate that α_{Chem} of $\text{LaMnO}_{3-\delta}$ is 0.024 between 600 °C and 1000 °C [85]. On the other hand, Vracar et al. investigate $\text{SrTi}_{1-x}\text{Fe}_x\text{O}_{3-\delta}$ (x varies between 0.3 and 0.75) and calculate α_{Chem} as 0.03 at ambient temperature [86]. α_{Chem} of $\text{La}_{0.25}\text{Sr}_{0.75}\text{FeO}_{3-\delta}$ is determined by Kharton et al. in a temperature range between 650 °C ($\alpha_{\text{Chem}}=0.017$) and 875 °C ($\alpha_{\text{Chem}}=0.047$) [87].

2.5 Methods for Production of LSMO and LCMO Powders

Throughout the years since the first production of LSMO and LCMO powders, many methods have been developed by researchers in order to obtain single phase nanopowders. In this section, methods commonly used to produce LSMO and LCMO powders will be discussed.

2.5.1 Solid State Reaction Method

It is the most common, basic and well-known production technique to produce mixed oxide ceramics such as manganites. Starting materials are generally oxides of the cations and in some cases carbonates. After weighing of starting materials, the mixture is wet ball-milled and after milling resulting slurry is dried. Annealing of mixture at high temperatures in order to increase mobility of atoms and reaction rate

is the final step of solid state synthesis method. It is a suitable technique for large scale production but it has some disadvantages such as time dependency, high annealing temperature and excess contamination during ball milling [88]. Figure 11 demonstrates the effect of time on reaction products.

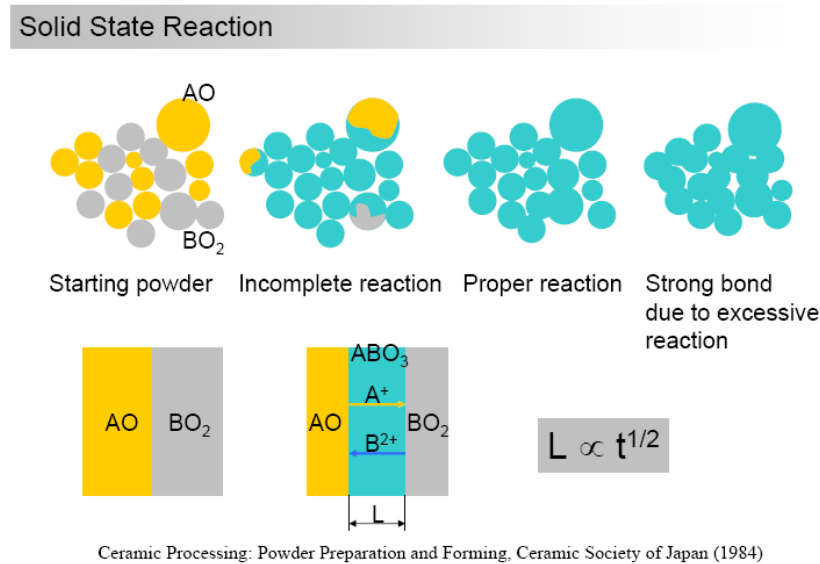


Figure 11: Effect of time on reaction products [89]

La_2O_3 , MnO_2 and $SrCO_3$ are mixed stoichiometricly and heated at high temperatures in order to remove carbonate. Then powders are pressed in order to produce pellets and reheated. The resultant pellets are regrinded and eventually, single phase LSMO are produced. For LCMO, instead of $SrCO_3$, $CaCO_3$ are used as starting materials [31, 88].

2.5.2 Pechini Method

Pechini method is common polymerization technique. It is one of the most successful process to obtain single phase mixed oxide ceramic compounds [90]. In this technique, there are various mechanisms affecting final products. The main

stabilizing mechanism of this process is chelation of cations by organic acids providing homogenous distribution of metal-organic complexes [90]. Polyesterification reaction occurs when solution is heated at elevated temperatures. In this reaction, the organic acids surround the metal cations and this results in homogeneous distribution of cations in polymeric resin. After the calcination of this polymeric resin, the single phase mixed oxide ceramic powders are obtained [90].

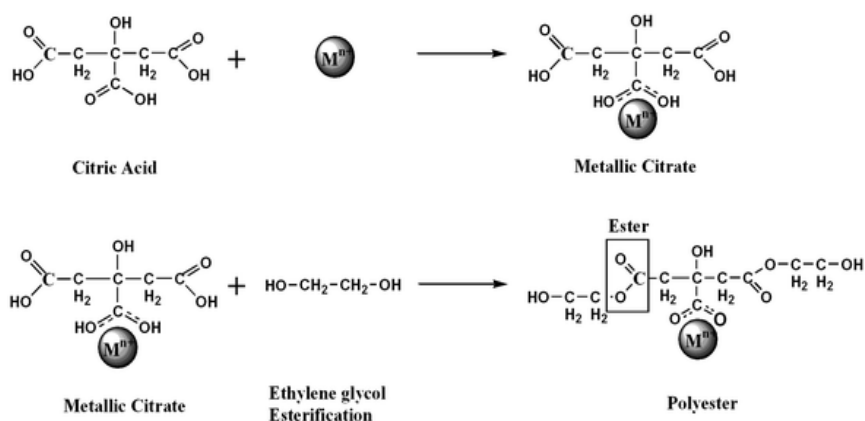


Figure 12: Processing route of Pechini method [91]

Generally, sulfates or nitrates of cations are used as starting material. Starting materials are added into organic acids such as acetic acid, citric acid and so on. As it can be seen from Figure 12, ethylene glycol is put into solution to start polyesterification reaction and remaining is water. Solution is heated between 120°C and 200°C to remove water from system. After calcination at high temperatures, single phase mixed oxide ceramic powders are obtained [92].

$\text{La}(\text{NO}_3)_3 \cdot 6\text{H}_2\text{O}$, $\text{Sr}(\text{NO}_3)_2$ and $\text{Mn}(\text{NO}_3)_3 \cdot 6\text{H}_2\text{O}$ are mixed stoichiometricly and citric acid is added into solution. Ethylene glycol is added and used to initiate the polyesterification reaction. Precursors, ethylene glycol and citric acid are added together in various amounts. Water is added independently from the stoichiometry.

Solution was mixed at constant stirring. Resulting resin is calcinated at high temperature and single phase powders are obtained [93].

2.5.3 Solution Combustion Synthesis Method

Solution combustion synthesis is a rapid and basic process to produce synthesis of nanopowders effectively. Depending of the starting materials, combustion occurs either layer by layer or as a whole volume. Doping of trace amount impurity atoms is very simple and succesful in this process [94].

The metal nitrate precursors ($\text{La}(\text{NO}_3)_3 \cdot 6\text{H}_2\text{O}$, $\text{Sr}(\text{NO}_3)_2$ and $\text{Mn}(\text{NO}_3)_3 \cdot 6\text{H}_2\text{O}$) are mixed with water and then stoichiometric amount polyvinyl alcohol was added. Until ignition, solution is heated under a thermal plate. After combustion, resulted powders are calcined at high temperatures [95].

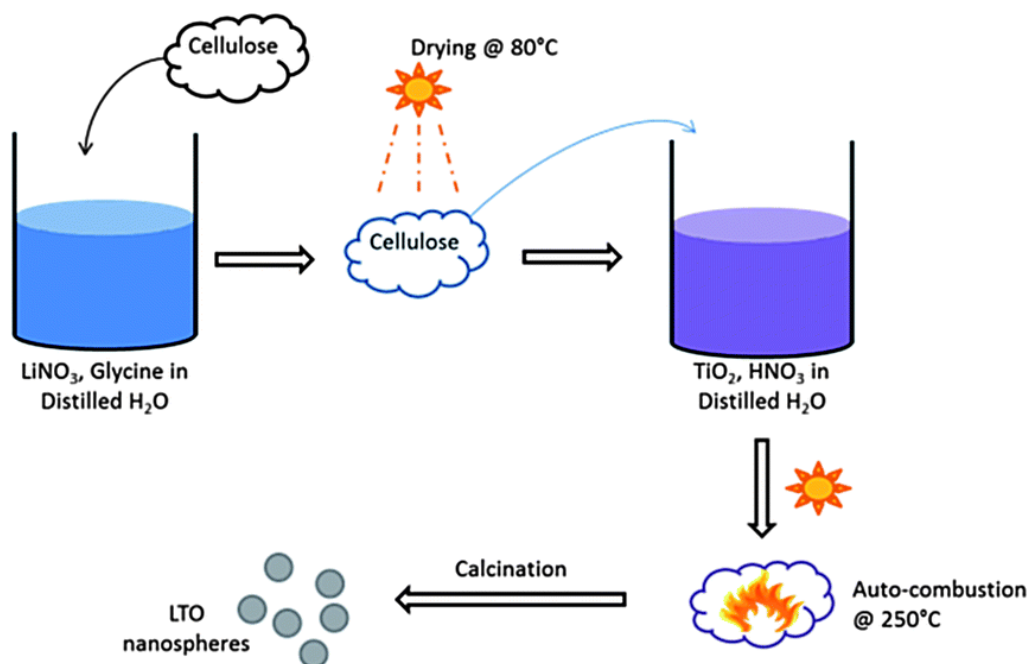


Figure 13: Schematic solution combustion synthesis route [96]

2.5.4 Hydrothermal Synthesis Methods

In hydrothermal synthesis methods, starting materials are metal oxides, metal salts, hydroxides and metal powders. Starting materials are mixed with water. By heating the solution and applying pressure, ceramic powders are produced. The use of pressure and heat enables the production of sub-micron sized oxides, non-oxides and metallic particles. The main advantages of this technique is the low temperature synthesis capability and usage of impure starting materials. Moreover, it offers a better control over diffusion kinetics, particle size distribution and phase purity [97].

$\text{MnCl}_2 \cdot 4\text{H}_2\text{O}$, $\text{LaCl}_2 \cdot 7\text{H}_2\text{O}$, $\text{SrCl}_2 \cdot 6\text{H}_2\text{O}$ and KMnO_4 are starting materials of this process. As a surfactant, $((\text{C}_{16}\text{H}_{33})\text{N}(\text{CH}_3)_3\text{Br})$ is used commonly. KMnO_4 was added to ensure alkalinity. Solution is mixed to obtain homogeneity and after that placed in autoclave and heated 240°C for one day. The resulting solution is washed with ethanol and deionized water to remove residual surfactant and chloride and potassium ions. At the end, product was reheated to 80°C to increase the yield of small size particles [98].

2.5.5 Co-precipitation Method

In co-precipitation method, starting materials are nitrates or chlorides of cations and mixed with liquid such as water. After precipitation process, hydroxides of cations are obtained. During precipitation, urea and ammonia are used commonly as a precipitant. Before the next step, hydroxides are washed and dried. After calcination of hydroxides, fine oxide powders are produced.

La_2O_3 , manganous nitrate and strontium carbonate are used as starting material. Nitric acid treatment performed for dissolution of carbonates and lanthanum oxide. Appropriate amounts are prepared for stoichiometric LSMO. The mixture is added into precipitation bath. Precipitator is aqueous solution of ammonium carbonate and for complete precipitation it has to be 50% excess. The pH of the precipitating bath kept by adding ammonia. Drying of precipitates takes 3 hours at 65°C . Resulting product was grinded and calcined at high temperatures [99].

2.5.6 Sol-Gel Method

Under wet chemical synthesis processes, sol-gel method is the most common method due to its advantages such as good homogeneity, better purity, fine particles and adequate composition control. It is a cost effective process due to its capability to be synthesized at low temperatures. The advantages of sol-gel method attract scientists to produce mixed oxide ceramics [100], as well.

Ceramic materials should be as pure as possible with well-controlled microstructure and nominal compositions in order to be used in industrial applications. Sol-gel method provides the purification of precursors by distillation which results in a highly pure final product.

The most important advantage of sol-gel method is the ability of mixing of precursors, which are the source of cations. This provides a decrease in diffusion length in molecular level. Eventually, the stable phases can be gained easily.

Dense thin films, ceramics, uniform particles, aerogels and fibers can be obtained by sol-gel method. Figure 14 describes the production routes of final products obtained by sol-gel method. Typically, there are two kinds of sol-gel methods. Those methods are named as particulate sol-gel method (known as non-alkoxide method) and polymeric sol-gel method (known as alkoxide method). In particulate sol-gel method, inorganic salts of cations are mainly consumed. The final products must be washed out to remove the inorganic anions. In polymeric sol-gel method, metal alkoxide precursors are the starting materials to produce a gel with continuous network. For two these sol-gel methods, the process occurs in same steps: hydrolysis, condensation, oxolation, and oxide network.

The common disadvantages of sol-gel method can be listed as: (i) excessive porosity, (ii) residual carbon and (iii) relatively long process times.

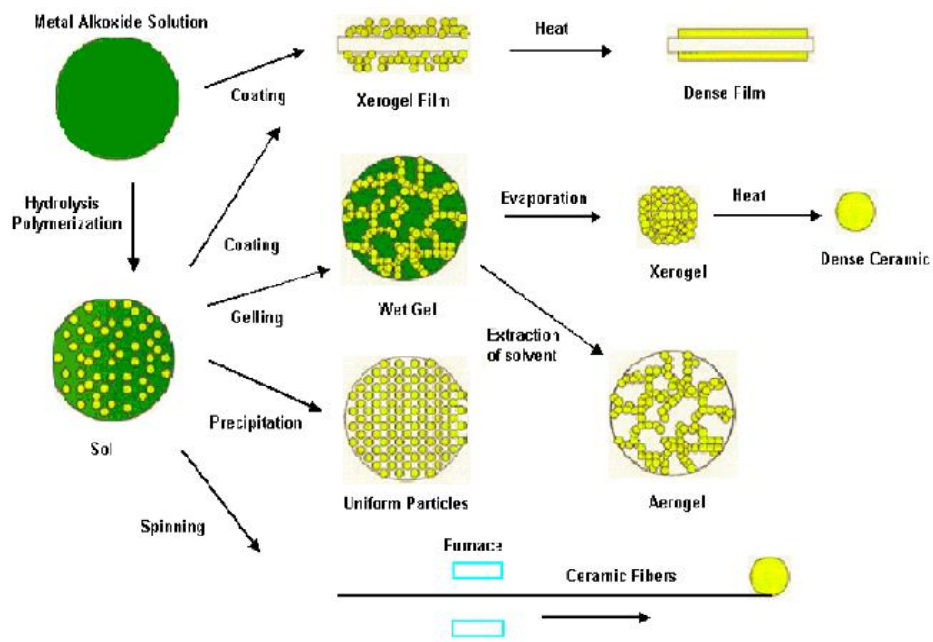


Figure 14: Production routes of various types of final products by sol-gel method

CHAPTER 3

EXPERIMENTAL PROCEDURE

In this research, Pechini method was employed as the production technique. Variety of characterization techniques were performed including X-ray Powder Diffraction (XRD), Scanning Electron Microscope (SEM) and Energy Dispersive X-ray Spectroscopy (EDS). Thermogravimetric Analysis (TGA), Dilatometry and High Temperature X-ray Powder Diffraction (HTXRD).

3.1 Powder Synthesis

Manganese (II) nitrate tetrahydrate ($\text{Mn}(\text{NO}_3)_2 \cdot 4\text{H}_2\text{O}$), lanthanum (III) nitrate hexahydrate ($\text{La}(\text{NO}_3)_3 \cdot 6\text{H}_2\text{O}$) and strontium nitrate ($\text{Sr}(\text{NO}_3)_2$) were supplied from Merck[®] and they were used as metal sources for all of powder production. Citric acid ($\text{C}_6\text{H}_8\text{O}_7 \cdot \text{H}_2\text{O}$) was employed as an agent for formation of polymer-metal complexes. Ethylene glycol ($\text{C}_2\text{H}_6\text{O}_2$) was used to form polymeric resin and start polyesterification reaction. Deionized water was used to prevent involvement of impurity ions and provided from ELGA Process Water. All of the used chemicals were analytical grade and no other purification was further employed.

Manganese, lanthanum and strontium were dissolved in water and citric acid was added into the solution. Solution was mixed with magnetic stirrer at various speeds. Temperature was risen to 80°C in order to provide bonding between metal ions and

citric acid. This process was taken approximately 4 hours. Ethylene glycol was added into the solution to form polymeric resin. For gelation process, temperature was risen up to 110°C and kept constant between 6 and 8 hours. The gel was dried by heat-treatment at 110°C and ground in agate mortar. Calcination was then performed in alumina crucibles at various temperatures.

3.2 Powder Characterization

3.2.1 X-Ray Diffraction Analysis

In this research, X-ray diffraction analyses were performed many for two purposes. The first one is to confirm phases whether it is fully crystalline or not and identify the phases after calcination. The other purpose being the most important one is calculating chemical expansion by conducting high temperature X-ray diffraction experiments (HTXRD). Analysis was carried out using a Bruker AXS GmbH D8 Advance diffractometer. The X-ray generator voltage and current were set-up and kept constant at 40kV and 40mA, respectively. Cu K_α target with a Ni filter was used as X-ray source to create a wavelength of 1.54056 Å.

DIFFRAC PLUS Evaluation software was used to analyze diffraction data. For HTXRD measurements, Anton Paar HTK16N chamber was mounted on the diffractometer and Anton Paar HTK 2000N controller was used. The heating strip of the chamber is platinum a filament which can be heated up to 1600°C. In our experiments, the chamber is heated upto 900°C under nitrogen (N₂) atmosphere.

It should be noted that calibration of Anton Paar heating chamber is significant. After mounting of chamber, X-ray tube and detector is taken zero position so that the coming beam is only transmitted to the detector. Then, the intensity of coming X-ray is adjusted to be the half of intensity of transmitted X-ray. The other half is hit to the edge of heating strip and be lost.

The samples were resistance-heated in the chamber with a rate of 2°C/min. The temperature of samples were determined by two thermocouples placed above and below of the heating strip. Heating sequence is used to determine the chemical expansion and evolving phases. All samples were held isothermally with 100°C step and diffraction data were collected between 5° and 120° in continuous scan mode with rate of 2°/min in parallel beam geometry under N₂ protective atmosphere. At the end of experiments, powders were cooled to room temperature with 5°C/min. At all isothermal step, the samples were held 10 minutes for homogeneous distribution of heat in heating strip.

Diffraction patterns were constructed by Origin 8.0 and CMPR softwares. Crystal structure of samples were determined from ICDD database. Linear least square method was performed in order to calculate lattice parameter of each sample at every temperature step.

3.2.2 Thermogravimetric Analysis (TGA)

Thermogravimetric analysis (TGA) was carried out by an EXSTAR TG/DTA 7300 to measure the mass change in controlled atmosphere. Schematics of device is illustrated in Figure 15. It has dual beam for measurement and horizontal device. Left one is used for reference samples whereas right one is for actual samples. The detectors measure the difference of masses at beams with micron errors. The furnace has a heating capacity up to 1500°C with a maximum heating rate 100 °C/min. The calibration of device was carried out by the manufacturer.

In this research, LCMO sintered samples were ground to prepare fine powders of the samples. Each experiment were repeated four times in order to detect, the experimental error. Alumina crucibles were used for TGA measurements. No reaction were observed between the alumina crucibles and LSMO or LCMO powders. Thermogravimetric measurements were performed between 30 °C and 900 °C with a rate of 2 °C/min under N₂ atmosphere using 8 mg of powders. It is assumed that the weight loss is only related to oxygen loss.

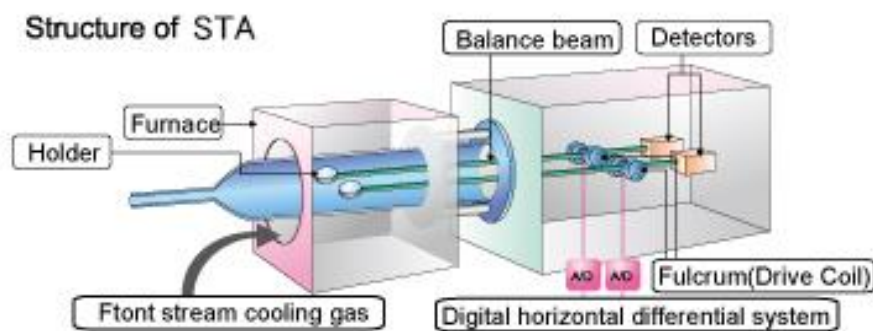


Figure 15: Structure of EXSTAR TG/DTA 7300

TGA gives mass loss with increasing temperature. Weight loss (TG), derivative of weight loss (DTG), differential temperature changes (DTA) are measured with respect to temperature. TGA data were significant for the conducted study because of the fact that oxygen deficiency (δ) is related to weight loss.

3.2.3 Scanning Electron Microscopy (SEM)

FEI Nova Nano SEM 430 Field Emission Scanning Electron Microscope was used to conduct SEM analysis in order to examine surface morphology. Energy Dispersive X-ray Spectroscopy (EDS) was performed to check nominal composition of the samples. Powder specimens were coated with gold (Au) to enhance conductivity.

3.2.4 Dilatometry

Dilatometry analysis was conducted in the Central Laboratory of Middle East Technical University. The experiment was executed between 30 °C and 900 °C with a heating rate of 2 °C/min under N₂ atmosphere using a Setaram Labsys dilatometer.

CHAPTER 4

SYNTHESIS OF LCMO5 & LSMO SERIES

4.1 Synthesis of $\text{La}_{0.5}\text{Ca}_{0.5}\text{MnO}_{3-\delta}$

Synthesis of bulk $\text{La}_{0.5}\text{Ca}_{0.5}\text{MnO}_{3-\delta}$ was performed by Pechini method in Max Planck Institute for Solid State Research in Stuttgart by Prof. Hanns-Ulrich Habermeier.

4.2 Synthesis of LSMO Series

Synthesis of LSMO series starts with the preparation of precursors. Manganese (II) nitrate tetrahydrate, lanthanum (III) nitrate hexahydrate and strontium nitrate are the main precursors of metal ions. The amount of chemicals needed for the preparation of LSMO solutions is given in Table 3.

As it can be seen from Table 3, at all LSMO series, the manganese is one mole and the amount of manganese precursor is constant. The amount of strontium and lanthanum precursor changes with doping amount of strontium. The calculations are based on molar value and the produced LSMOs are assumed as fully stoichiometric. There is a molar ratio between the amounts of chemicals used in production. The mole of ethylene glycol is twelve times larger than the total mole of metal cations in precursors and four times larger than citric acid. Between citric acid and metal cations, the mole of citric acid is 3 times larger than the total mole of metal cations.

The ratio can be represented as 1:3:12. The amount of water used is arbitrary since water is evaporated during production.

Table 3: The amount of chemicals needed for the preparation of LSMO solutions

Solution Name	La(NO ₃) ₂ ·6H ₂ O (g)	Mn(NO ₃) ₂ ·4H ₂ O (g)	Sr(NO ₃) ₂ (g)	Ethylene Glycol(g)	Citric Acid (g)
LMO	1.361	0.8	0	1.559	1.319
LSMO1	1.225	0.8	0.0664	4.668	3.963
LSMO2	1.089	0.8	0.133	4.668	3.963
LSMO3	1.036	0.8	0.199	4.668	3.963
LSMO4	0.816	0.8	0.266	4.668	3.963
LSMO5	0.681	0.8	0.332	4.668	3.963
LSMO6	0.545	0.8	0.399	4.668	3.963
LSMO7	0.408	0.8	0.465	4.668	3.963
LSMO8	0.272	0.8	0.531	4.668	3.963
LSMO9	0.136	0.8	0.600	4.668	3.963
SMO	0	0.8	0.800	3.754	3.177

The preparation of LSMO series started with the mixing of manganese, lanthanum and strontium precursors in stoichiometric amounts. Arbitrary amount of deionized water was added with mixture of precursors in the beaker while continuous magnetic stirring was performed. After citric acid was introduced to solution and the magnetic stirring was continued, the temperature was risen up to 80°C. The purpose of heating is to provide better homogeneity and bonding between citric acid and metal cations in solution. After 3-4 hours, ethylene glycol was added into the solution. Temperature was increased to 110°C to start polyesterification reaction. Polyesterification is the reaction between chelated metallic complex and ethylene glycol to form

polymeric resin. As a result of polyesterification, the segregation of cations are prevented due to immobilize cations in polymeric resin. The formation of gel was completed after 6-8 hours. The gel was dried in the furnace at 110°C. After drying, the resultant samples were ground. Calcination of grinded polymeric resins formed the mixed oxide ceramic powders. The calcination temperatures have been altered with the amount of Sr doping. At LMO, LSMO1, LSMO2, LSMO3, LSMO4 and LSMO5, calcination temperature was 700°C whereas with higher Sr doping 1450°C was employed for calcination in a box furnace. During calcination, the heating rate of substances in the furnace was 5°C/min and substances were waited 3 hours after heating. At the end, furnace cooling was performed. TGA and all other XRD experiments were performed with calcined powders. Powders should be pressed and sintered at various temperatures for dilatometry experiments. The LSMO powders were pressed uniaxially 125 MPa and resulted pellet sintered at 1450°C for densification. The heating rate during sintering was 5°C/min and substances were waited 12 hours after heating. At the end, furnace cooling was performed. Figure 16 shows the flowchart of experimental procedure of LSMO production.

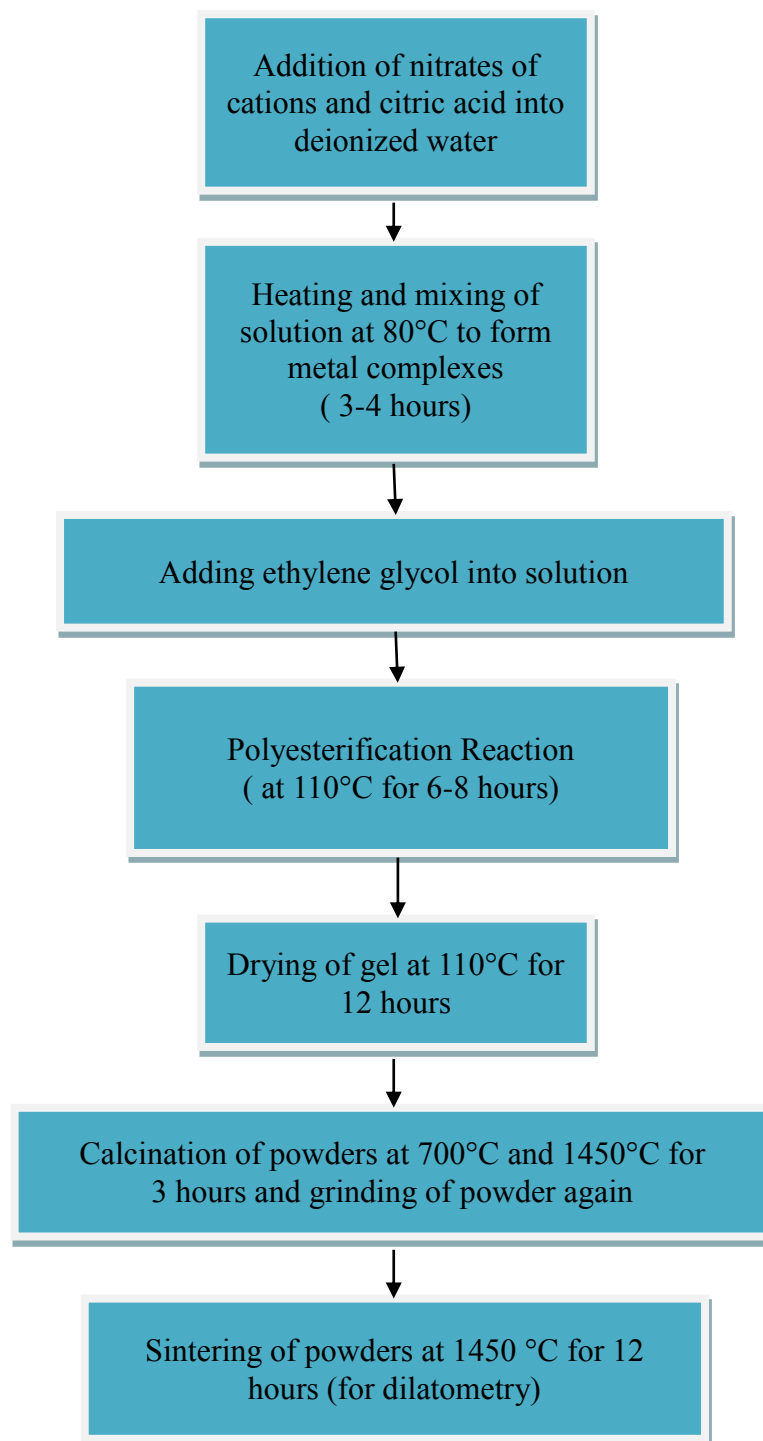


Figure 16: Flowchart of Pechini Method

CHAPTER 5

MEASUREMENT OF CHEMICAL EXPANSION

5.1 General Remarks

Different amount of Sr doped LSMO, LMO, SMO and LCMO5 samples were synthesized by Pechini method and various calcination regimes were applied to obtain single phase materials. Corresponding process was previously described in Section 4.1 and 4.2 for different samples.

In order to determine chemical expansion coefficient of all samples, samples were characterized by in-situ X-ray diffraction (HTXRD), thermogravimetry analysis (TGA) and dilatometry. Powders before and after TGA experiments were investigated under SEM.

In this part of the thesis, the data obtained from the experimental study were presented and the results were discussed in details.

5.2 Room Temperature Investigation of LCMO5 and LSMO Series

In order to calculate correct chemical expansion coefficient, LSMO and LCMO5 powders should be produced as single phase [80, 81]. Room temperature XRD spectra of LSMO and LCMO5 samples are illustrated in Figure 17 and Figure 18. All

samples are assumed to be fully stoichiometric which means that no cation and oxygen deficiency at room temperatures.

XRD indicates a perfect single phase structure for LCMO5 as shown in Figure 17. The crystal structure and space group of LCMO5 was observed as orthorhombic and Pnma from ICDD database and literature [101].

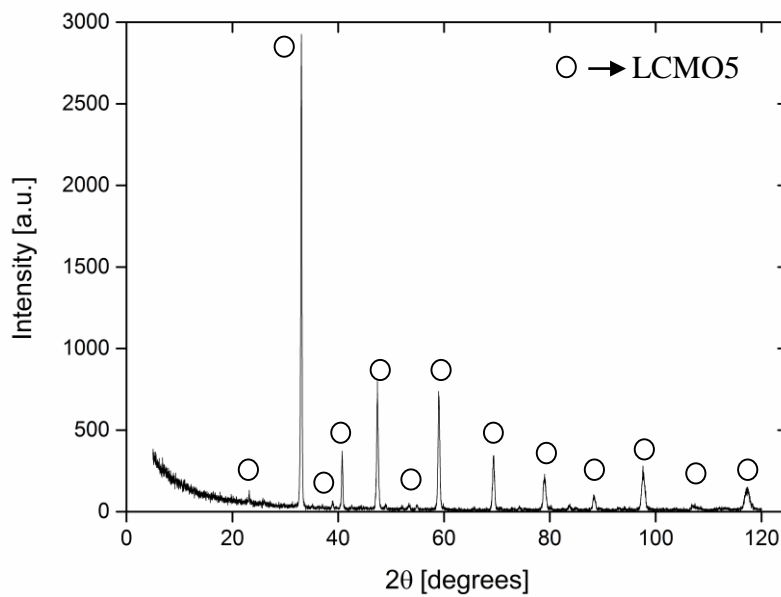


Figure 17: XRD Spectra of LCMO5

At first glance, from LMO to LSMO8 samples, no additional peaks representing a second phase formation were observed. The crystal structure seems to be the same with respect to Sr doping. However, when it was carefully investigated the peak around 47° for LSMO5 and LSMO6 indicates a possible difference in crystal structure. Figure 19 illustrates that rhombohedral (024) reflection is separated into tetragonal (004) and (220) peaks [31].

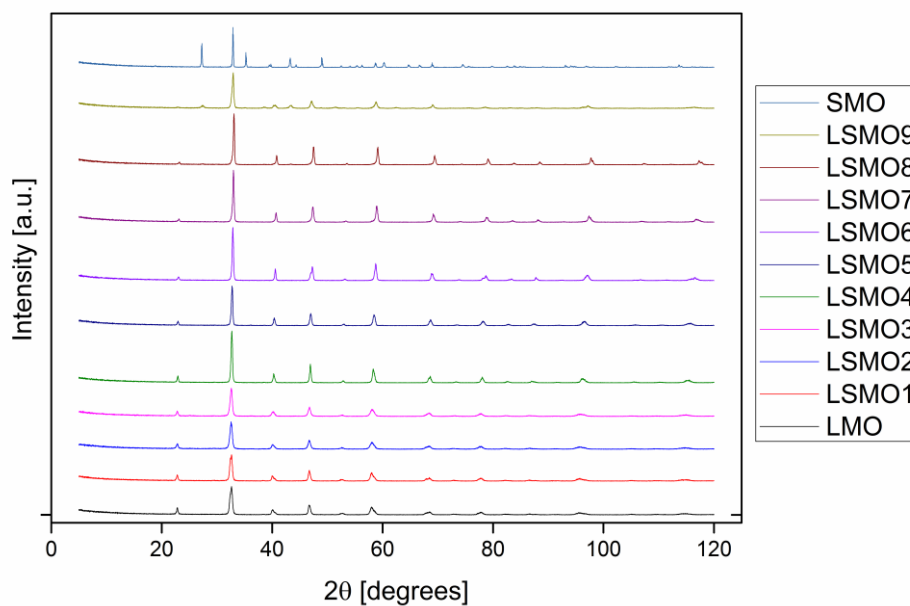


Figure 18: XRD Spectras of LSMO Series

From LMO to LSMO5, the XRD spectras demonstrate the same single (024) peak around 47° . Whereas LSMO6, LSMO7 and LSMO8 have two peaks representing (004) and (220) reflections. Rhombohedral structure ($R\bar{3}c$) is seen from LMO to LSMO5 and tetragonal structure ($I4/mcm$) is observed in LSMO6, LSMO7 and LSMO8. The difference between orthorhombic and tetragonal phases can not be observed in XRD spectras thus, to determine whether it is tetragonal or orthorhombic, ICDD database were used [46]. At LSMO9 and SMO, additional peaks were detected and crystal structure is found out to be hexagonal having $P63/mmc$ space group.

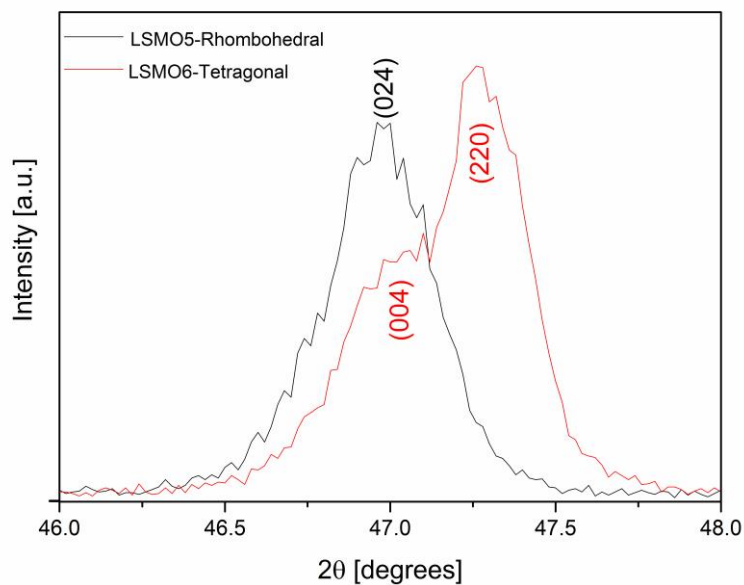


Figure 19: (004) and (220) reflections for tetragonal and (024) reflection for rhombohedral crystal structures

There are significant peak shifts in the two-theta values of LSMO peaks within the experimental error limits (Table 4). Besides lowest and highest Sr amount, from LSMO2 to LSMO8, there is an increasing order with respect to 2θ values.

Table 4: 2θ values of LSMO series

Sr Amount	2θ (Degrees)
Pure LMO	68.313 ± 0.005
LSMO1	68.295 ± 0.005
LSMO2	68.281 ± 0.005
LSMO3	68.328 ± 0.005
LSMO4	68.536 ± 0.005
LSMO5	68.665 ± 0.005
LSMO6	68.978 ± 0.005
LSMO7	69.229 ± 0.005
LSMO8	69.432 ± 0.005
LSMO9	69.073 ± 0.005
SMO	68.965 ± 0.005

The amount of Sr and Ca doping was detected using EDS analysis. Table 5 demonstrates experimental La/Sr ratio gathered from EDS and theoretical La/Sr ratio. Each EDS analysis was performed four times.

Table 5: Amount of Ca by experimental study and theoretical calculation

Experimental La/Ca	Theoretical La/Ca
0.85 ± 0.10	1

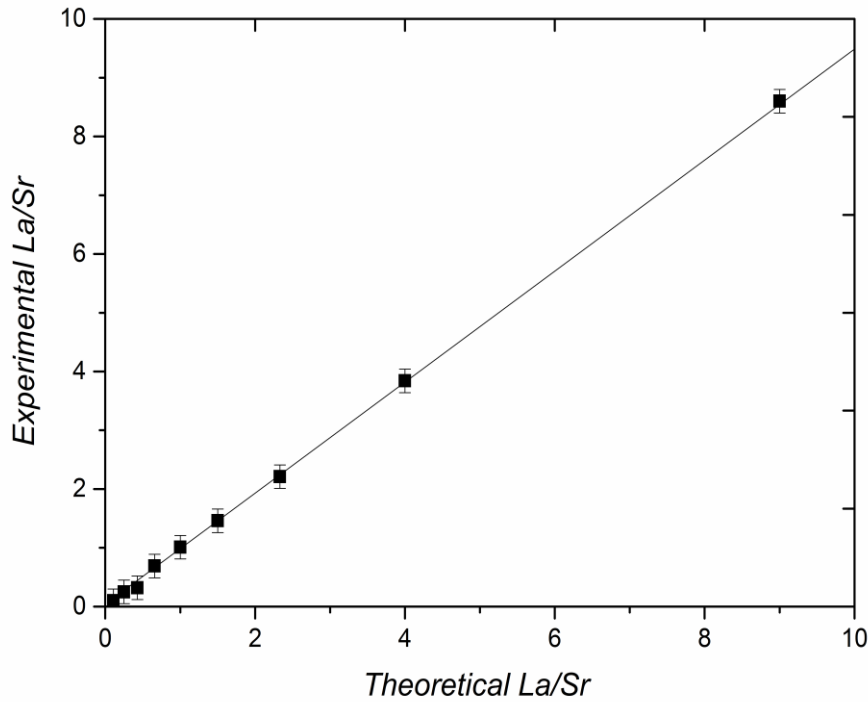


Figure 20: Amount of Sr by experimental studies and theoretical calculations

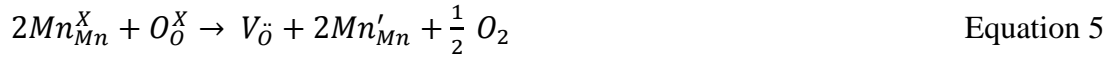
Figure 20 shows that the amount of Sr doping is in good agreement with theoretical amount. As it can be seen from Table 5 the amount of Ca doping is also fitted with the theoretical amount in LCMO5.

5.3 Chemical Expansion Coefficient of $\text{La}_{0.5}\text{Ca}_{0.5}\text{MnO}_{3-\delta}$ (LCMO5)

LCMO5 was synthesized as single phase orthorhombic structure according to XRD experiments. Oxygen deficiency (δ) and strain occurred from oxygen deficiency (ε) should be known to calculate chemical expansion coefficient. Equation 3 shows the corresponding relation.

$$\varepsilon = \frac{\Delta l}{l_0} = \alpha_{Chem} * \Delta\delta \quad \text{Equation 3}$$

Half of the aliovalent Mn cations are in 3+ and the remainings are 4+ valence state when the oxygen deficiency (δ), is 0. Some oxygen vacancies may be generated in the lattice if temperature is increased and/or oxygen partial pressure is reduced. During formation of oxygen vacancies, the following defect reaction occurs (written in Kröger-Vink notation) to maintain charge neutrality.



where Mn_{Mn}^X and O_O^X are Mn and O ions at their original locations. $V_O^{\bullet\bullet}$, Mn'_{Mn} , O_2 are the O vacancy, reduced Mn and O_2 molecule. This defect reaction is mainly the reason of chemical expansion.

TGA experiments were performed in order to calculate oxygen deficiency under N_2 atmosphere. During calculations, all weight loss assumed to stem from oxygen. TGA results are illustrated in Figure 21.

As it can be seen from Figure 21, no weight loss was observed up to 100°C. The start of weight loss corresponds to 100°C. The weight loss reaches up to 1.6 % when temperature is increased to 900°C. From calculations, δ term was found out 0.19. From this value, average Mn valency was calculated as 3.1+.

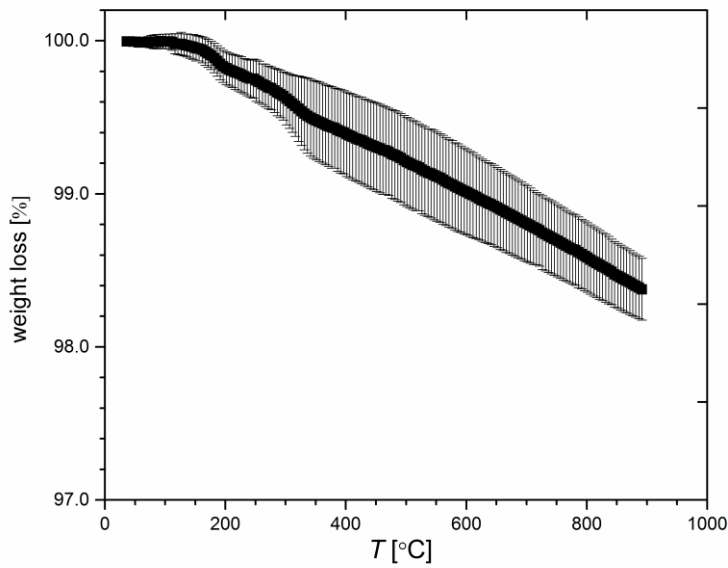


Figure 21: The percent weight loss versus temperature plot

Total strain can be found from dilatometry and in-situ XRD data. Figure 22 is total strain, ε , versus temperature, T , plot. ε can be represented by the following equation.

$$\varepsilon = \varepsilon_{Ther} + \varepsilon_{Chem} = \alpha_{Ther} * \Delta T + \alpha_{Chem} * \Delta \delta \quad \text{Equation 6}$$

where α_{Ther} and α_{Chem} are thermal and chemical expansion coefficient, respectively. Total ε reaches up to 1.06 % when T is increased to 900 °C under N_2 reducing atmosphere. It is seen from Figure 22 that the onset of weight loss corresponds to an approximately similar temperature range with the one where the linear ε - T plot found at low temperature range is lost.

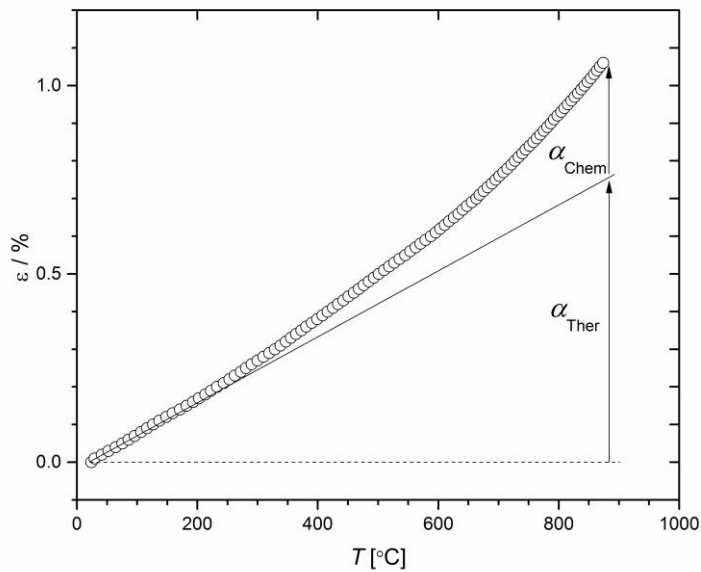


Figure 22: The percent strain as a function of temperature

From in-situ XRD experiments, it has been sure that there is only LCMO5 phase before and after the heat treatment. The reduction (i.e. O loss from the material) is responsible for the dilation (note that thermal strain is always taken into account during calculations) and for the accompanying weight loss. Moreover, α_{Chem} of LCMO5 has been identified to be 0.016. The α_{Chem} is plotted against δ in Figure 23 and three regions are indicated. In region 1, the points on the graph are very scattered and sporadic, a linear relationship is observed in region 2 and the slope of the line increases in region 3. This value, where the increase in slope occurs, corresponds to Mn valency of 3.25+. Finally, the Mn increases of 3.1+ at the end of region 3. LCMO5 becomes more compliant with an increase in δ (by either increasing T or reducing oxygen partial pressure).

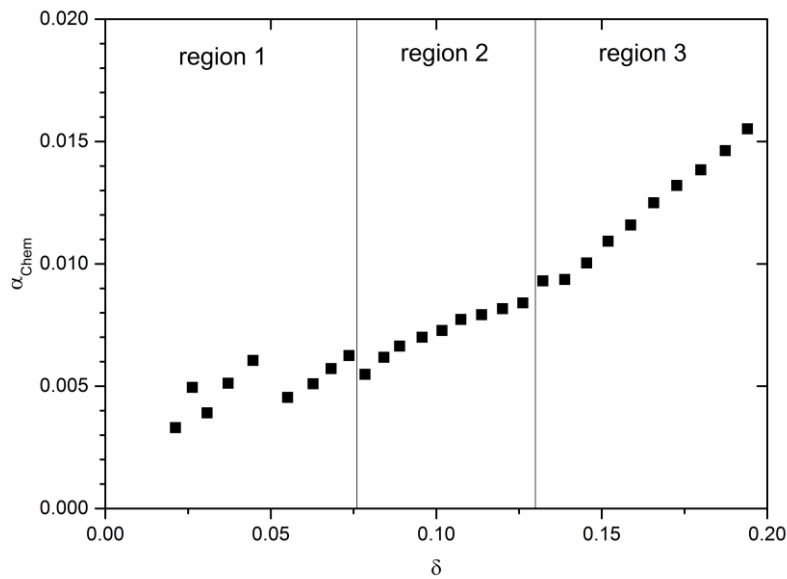


Figure 23: The relationship between α_{Chem} and δ in LCMO5

Also, in-situ XRD was performed in order to obtain data about total strain. The total strain can be expressed by following equation.

$$\alpha_{Chem} = \frac{1}{a} * \frac{\partial a}{\partial \delta} \quad \text{Equation 7}$$

where a , ∂a and $\partial \delta$ are lattice parameter of crystal structure, infinitesimal change in lattice parameter and oxygen deficiency.

It was previously stated that LCMO5 has an orthorhombic structure. As a result of in-situ XRD experiments, lattice parameters versus temperature behaviours were determined. By looking at the three lattice parameter values, there is an anisotropy in expansion values. According to Figure 25 and Figure 26, the chemical expansion coefficients are almost zero. In Figure 24, α_{Chem} was calculated as 0.014 which is very close to value obtained from dilatometry data.

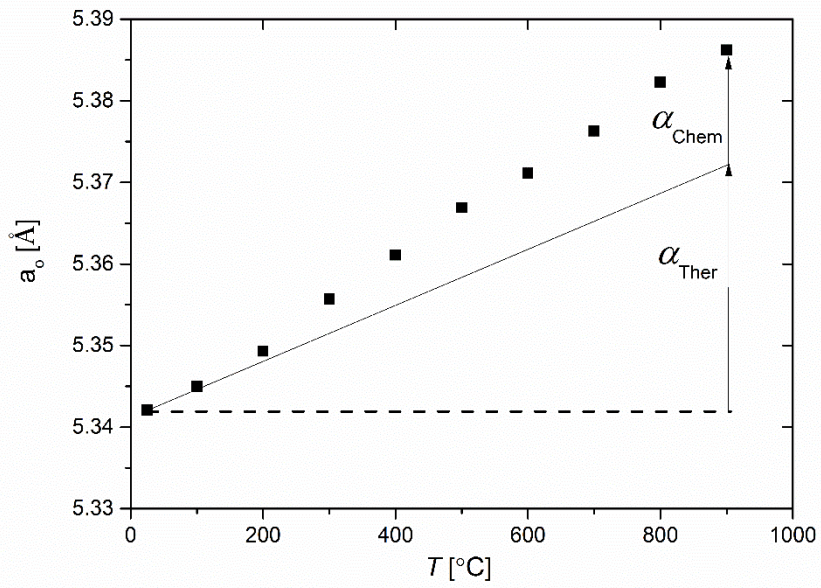


Figure 24: a_0 change with respect to temperature

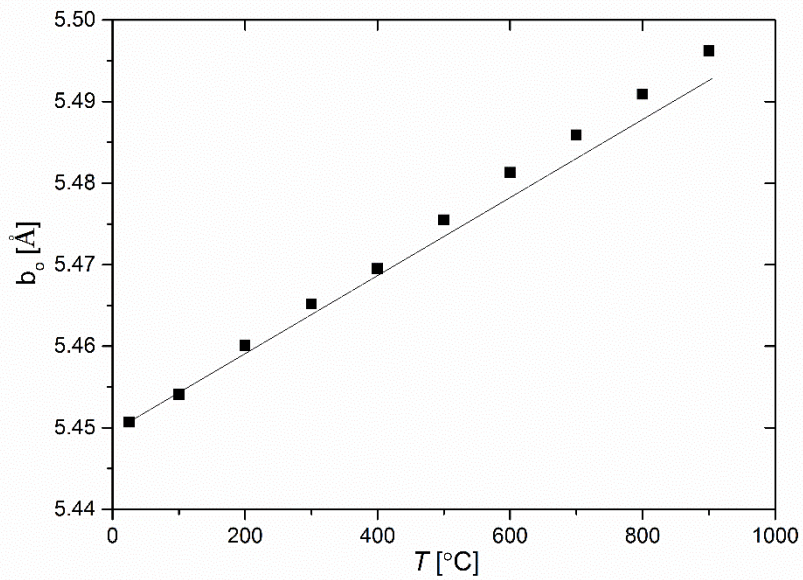


Figure 25: b_0 change with respect to temperature

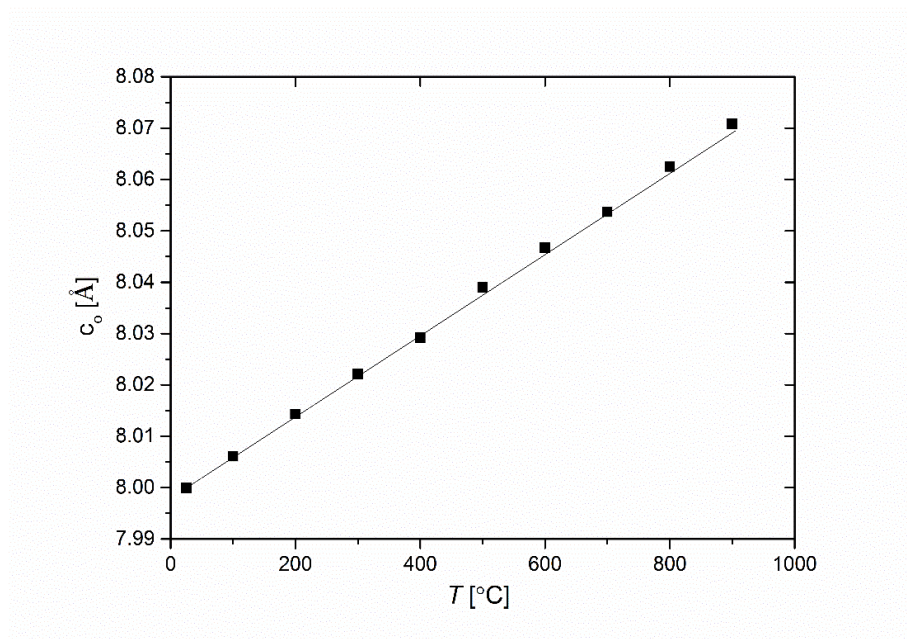


Figure 26: c_0 change with respect to temperature

The reason for this anisotropy can be explained with thermal expansion. In thermal expansion concept, materials are expanded or contracted anisotropically. The atomic positions, electronic interactions, bond strength of atoms can be the reasons for the anisotropy in chemical expansion values [102].

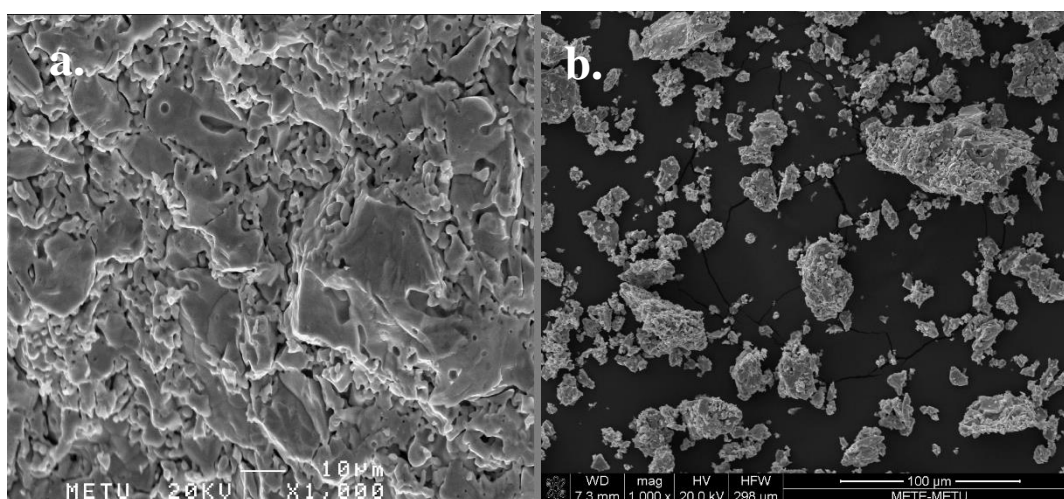


Figure 27: SEM images of a. LCMO5- Sintered b. LCMO5-After Treatment (1000x)

Surface morphologies of LCMO5 powders were investigated under SEM. SEM analyses revealed that powders were sintered due to be held high temperatures during experiments. After the high temperature experiments, there is no observable difference in particle morphologies. Moreover irregular shapes of agglomerates caused level differences in the powders being examined.

CHAPTER 6

CHEMICAL EXPANSION IN LSMO SERIES

Room temperature investigations of powders indicate that all samples are produced as single phase. From room temperature to 900°C, in-situ XRD proved that LSMO series do not undergo any phase transformation. In this section, TGA, In-Situ XRD analysis and SEM analysis will be shown in order for clarification.

6.1 Thermogravimetric Analysis (TGA) of LSMO Series

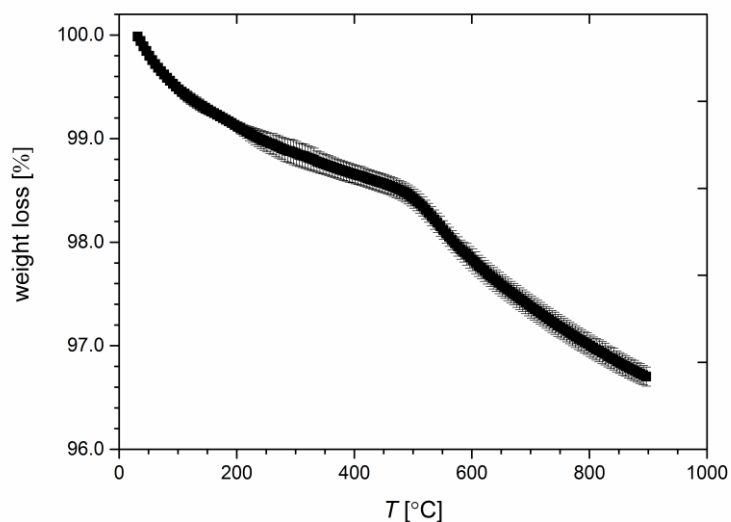


Figure 28: The percent weight loss versus temperature plot of LMO

As it can be seen from Figure 28, the weight loss starts immediately at room temperature. The reason for this can be explained that even though weight loss is observed close to room temperature kinetics of reaction do not allow to start at room temperature. Oxygen vacancy formation energy could be too low to create these oxygen vacancies. This explanation is valid for all LSMO samples. Tracer amount of oxygen were released close to room temperature. Also, around 485°C, the slope of TGA curve alters and as a result, the oxygen vacancy formation increases due to slope change. During this change, δ is close to 0.25 and Mn valency is approximately 2.5+. Half of the aliovalent Mn cation becomes Mn 3+ and the rest is Mn 2+. The weight loss reaches up to 3.3 % when temperature is increased 900°C. From calculations, δ term was found out 0.5. From this value, average Mn valency was calculated as 2+.

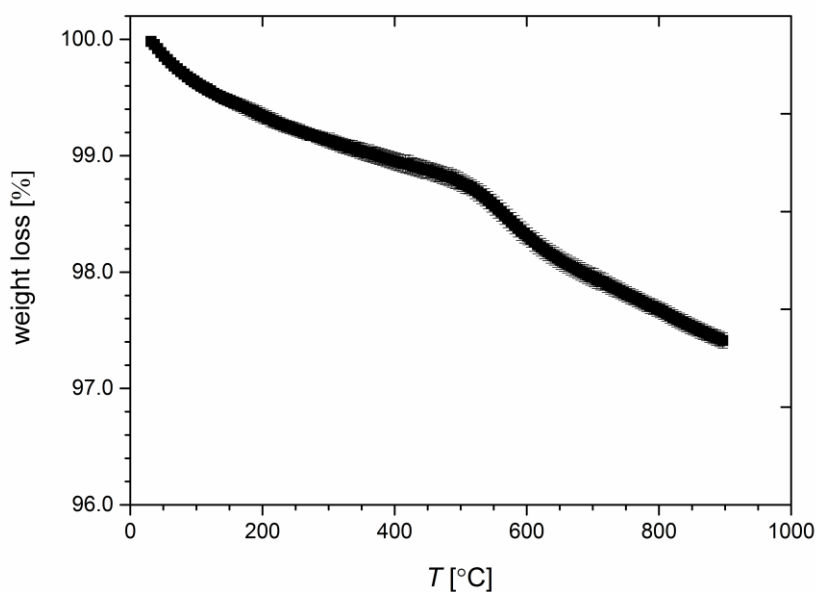


Figure 29: The percent weight loss versus temperature plot of LSMO1

In LSMO1, the weight loss reaches up to 2.6 % when temperature is increased to 900°C and δ approaches to 0.38. At 900°C, Mn valence state was found out 2.34+. It can be seen from Figure 29, same slope change seen in LMO was observed. At 485°C, the slope change is occurred. δ and Mn valence state at that temperature are 0.176 and 2.75.

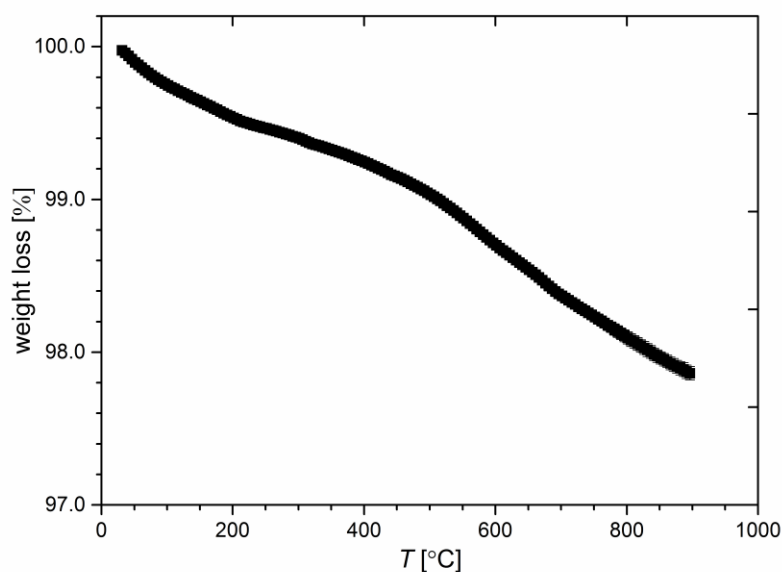


Figure 30: The percent weight loss versus temperature plot of LSMO2

In LSMO2 (Figure 30), around 470°C, the slope of TGA curve alters and as a result, the oxygen vacancy formation increases due to slope change. During this change, δ is close to 0.13 and Mn valency is approximately 2.94+. From in-situ XRD and DTA experiments, it is proven that there is no phase change at all. The weight loss reaches up to 2.2 % when temperature is increased 900°C. From calculations, δ term was found out 0.31. From this value, average Mn valency was calculated as 2.58+.

In Figure 31, between 285°C and 325°C, the slope of TGA curve alters and as a result, the oxygen vacancy formation increases due to slope change. However, after

325°C, the slope is going to be same with slope before 285°C. During this change, δ is between 0.15 and 0.20. Mn valency is approximately between 3+ and 2.9+. Up to 800°C, the slope of TGA curve increases and after 800°C, the weight loss stops. Almost no weight loss is seen. At 800°C, δ is 0.65 and Mn valency is 2+. The weight loss reaches up to 4.7 % when temperature is increased 900°C.

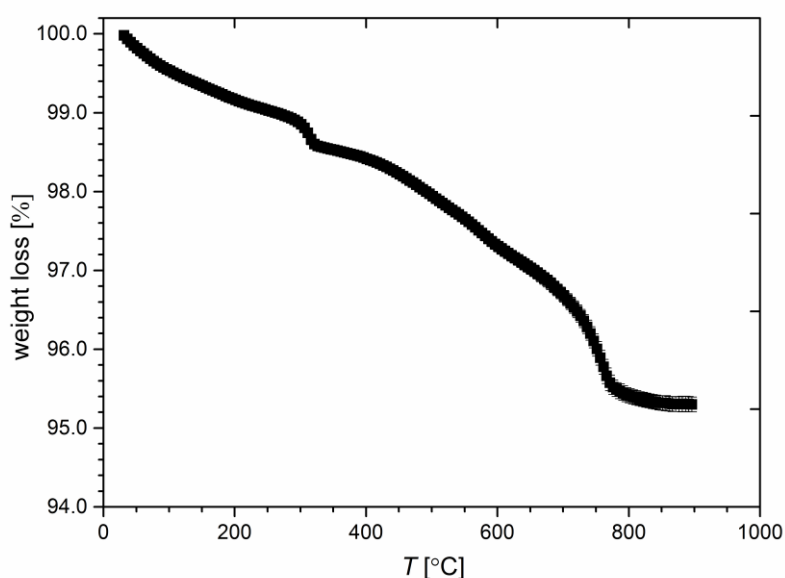


Figure 31: The percent weight loss versus temperature plot of LSMO3

In LSMO4, there are two important temperature values where slope of TGA curve changes. First value is 185°C. At this temperature, δ is 0.088 and Mn valency is approximately 3.22+. Second temperature value is 730 °C where δ is 0.318 and Mn valency is approximately 2.76+. Between 185 °C and 730 °C, the slope changes at 475 °C where δ is 0.17 and Mn valency is calculated as 3.05+. The weight loss reaches up to 2.6 % when temperature is increased 900°C. From calculations, δ term was found out 0.365. From this value, average Mn valency was calculated as 2.67+.

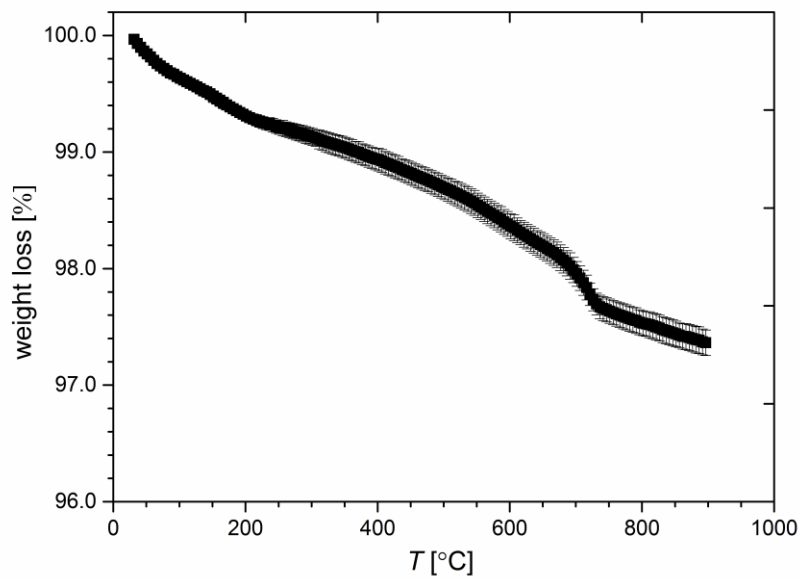


Figure 32: The percent weight loss versus temperature plot of LSMO4

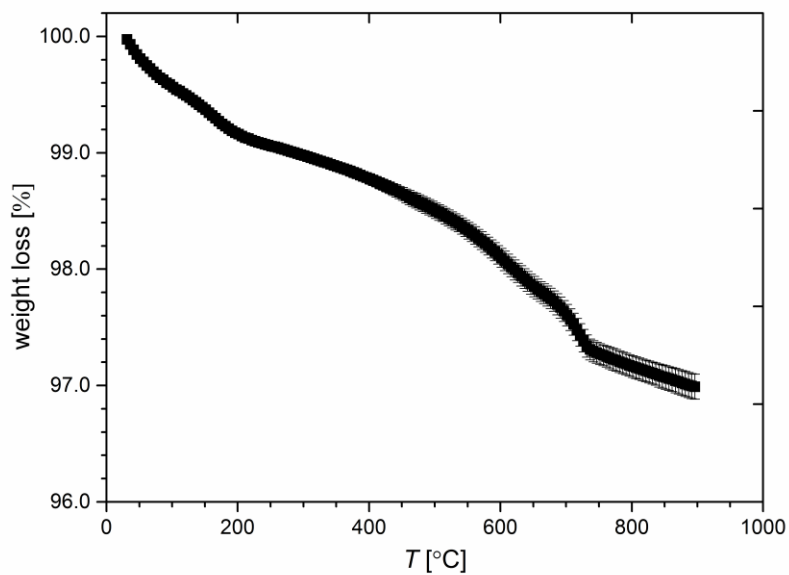


Figure 33: The percent weight loss versus temperature plot of LSMO5

In LSMO5, there two important temperature values where slope of TGA curve changes. First temperature value, 185 °C can be observed in Figure 33. At this temperature, δ is 0.106 and Mn valency is approximately 3.29+. Second temperature value is 730 °C where δ is 0.358 and Mn valency is approximately 2.78+. Between 185 °C and 730 °C, the slope changes at 540 °C where δ is 0.23 and Mn valency is calculated as 3.03+. Reason for slope change is the same for LSMO4.

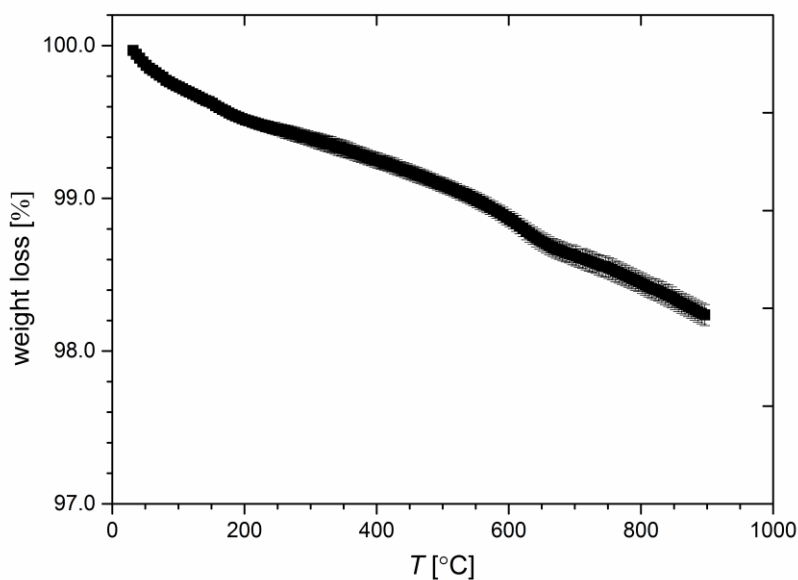


Figure 34: The percent weight loss versus temperature plot of LSMO6

As it can be seen in Figure 34, There are two important temperature values where slope of TGA curve deviates. First value is 185°C. At this temperature, δ is 0.06 and Mn valency is approximately 3.48+. Second temperature value is 680°C where δ is 0.177 and Mn valency is approximately 3.25+. From in-situ XRD experiments, it is proven that there is no phase change. The weight loss reaches up to 1.8 % when

temperature is increased 900°C. From calculations, δ term was found out 0.234. From this value, average Mn valency was calculated as 3.13+.

In Figure 35, TGA curve of LSMO7 is represented and there are two temperature values where slope of curve alters. First value is around 205°C. At this temperature, δ is 0.07 and Mn valency is approximately 3.56+. Second temperature value is around 640°C where δ is 0.176 and Mn valency is approximately 3.35+. From in-situ XRD experiments, it is proven that there is no phase change at all. The weight loss reaches up to 1.9 % when temperature is increased 900°C. From calculations, δ term was found out 0.246. From this value, average Mn valency was calculated as 3.21+.

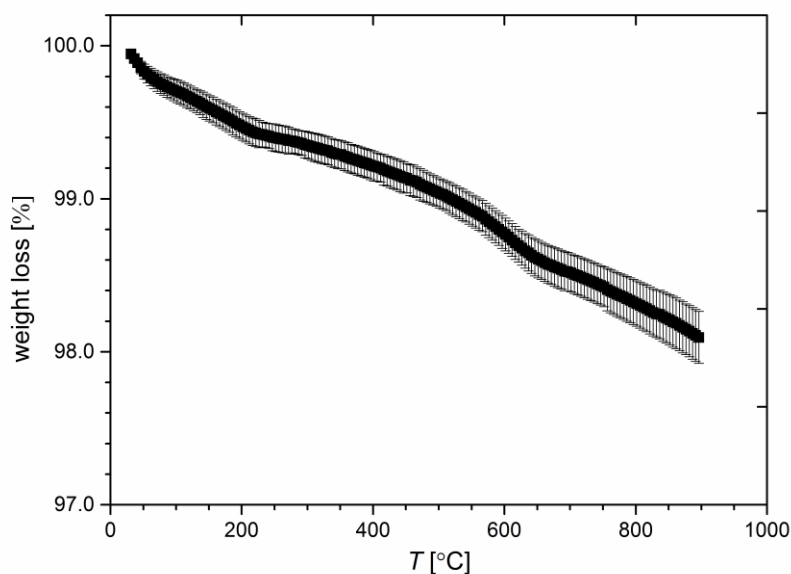


Figure 35: The percent weight loss versus temperature plot of LSMO7

As it can be seen from Figure 36, up to 100°C, no weight loss was observed and start of weight loss corresponds to 100°C. The weight loss reaches up to 1.7 % when temperature is increased 900°C for LSMO8. From calculations, δ term was found out

0.22. From this value, average Mn valency was calculated as 3.36+. There are two important temperature values where slope of TGA curve changes. First value is around 325°C. At this temperature, δ is 0.05 and Mn valency is approximately 3.7+. Second temperature value is around 780°C where δ is 0.15 and Mn valency is approximately 3.5+.

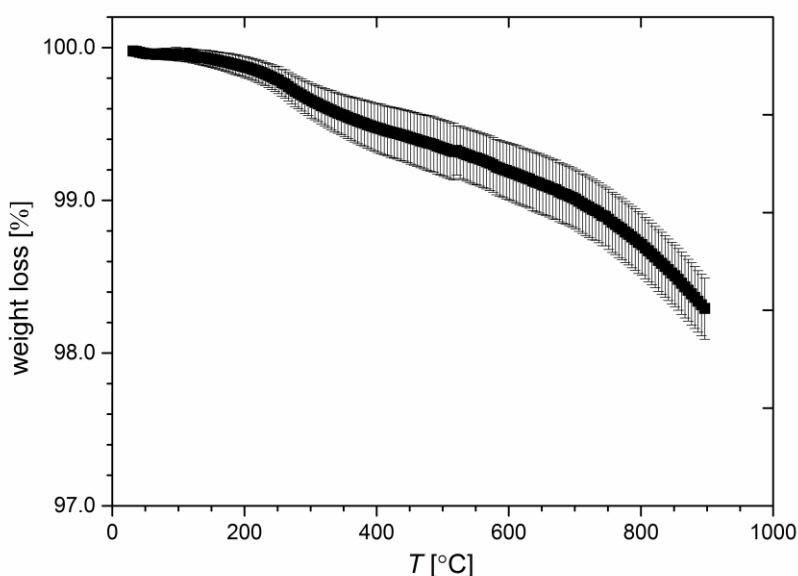


Figure 36: The percent weight loss versus temperature plot of LSMO8

In LSMO9, up to 100°C, no weight loss was observed and start of weight loss corresponds to 100°C. The weight loss reaches up to 1.25 % when temperature is increased 900°C. From calculations, δ term was found out 0.15. From this value, average Mn valency was calculated as 3.6+. Figure 37 demonstrates that there are two important temperature values where slope of TGA curve changes. First value is around 325°C. At this temperature, δ is 0.035 and Mn valency is approximately 3.83+. Second temperature value is around 780°C where δ is 0.11 and Mn valency is

approximately 3.70+. From in-situ XRD experiments, it is proven that there is no phase change at all.

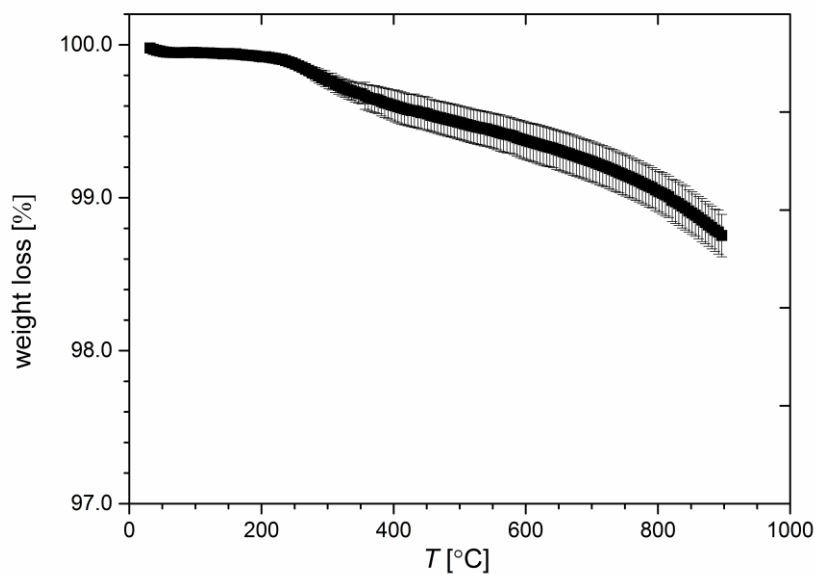


Figure 37: The percent weight loss versus temperature plot of LSMO9

As it can be seen from Figure 38, up to 100°C, no weight loss was observed and start of weight loss corresponds to 100°C. The weight loss reaches up to 1.25 % when temperature is increased 900°C. From calculations, δ term was found out 0.15. From this value, average Mn valency was calculated as 3.7+. There are two important temperature values where slope of TGA curve changes. First value is around 325°C. At this temperature, δ is 0.045 and Mn valency is approximately 3.91+. Second temperature value is around 780°C where δ is 0.11 and Mn valency is approximately 3.78+ in SMO.

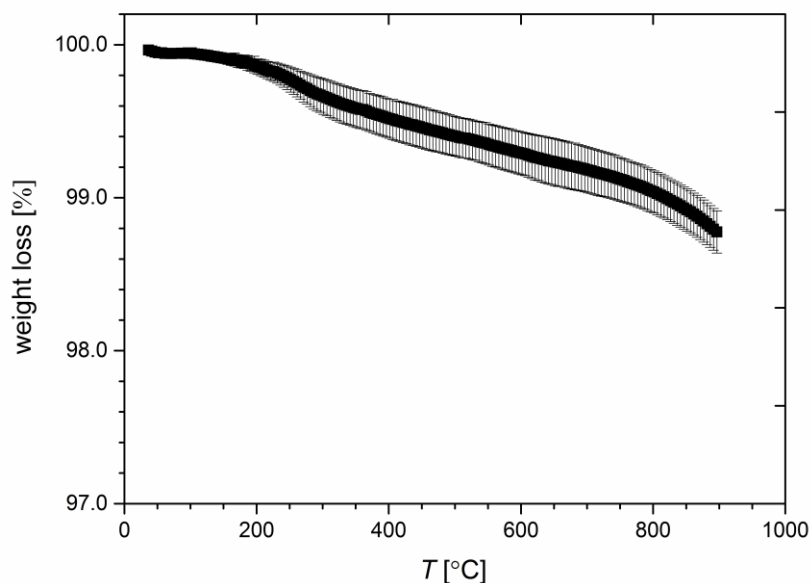


Figure 38: The percent weight loss versus temperature plot of SMO

6.2 In-Situ X-Ray Diffraction Analysis

In-situ XRD was employed to find out total strain at elevated temperatures. As a result of in-situ XRD experiments, lattice parameters versus temperature behaviour are determined. By looking at the lattice parameter values, one can argue that there is an anisotropy in expansion values just like thermal expansion. The reasons for anisotropy was previously explained in Chapter 4.3. Therefore, it is observed that chemical strain occurs only a site of structures in all LSMO series. It is previously stated that from in-situ XRD experiments and DTA experiments (conducted simultaneously with TGA experiments), it has been sure that there is only room temperature phase both before and after the heat treatment. Reduction (i.e. O loss from the material) is responsible from the dilation (note that thermal strain is always taken into account during calculations) and the accompanying weight loss.

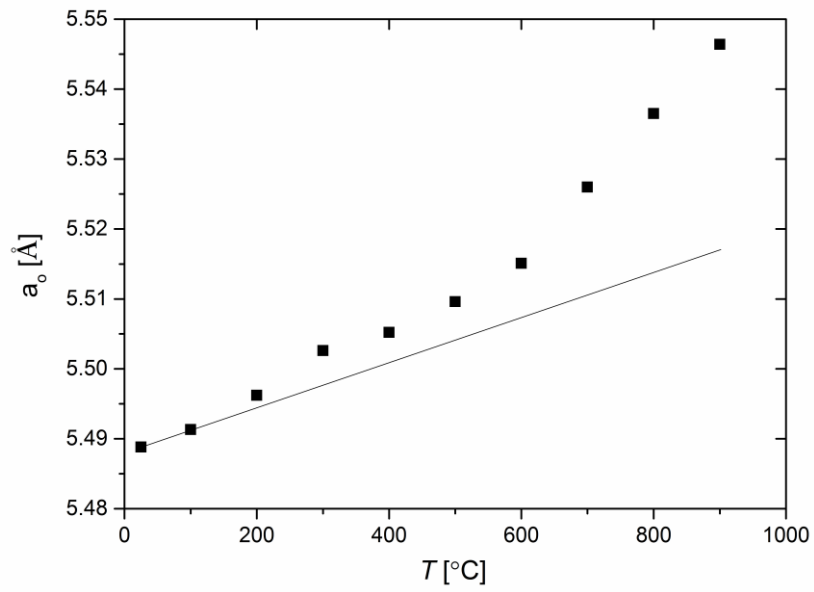


Figure 39: a_0 change with respect to temperature in LMO

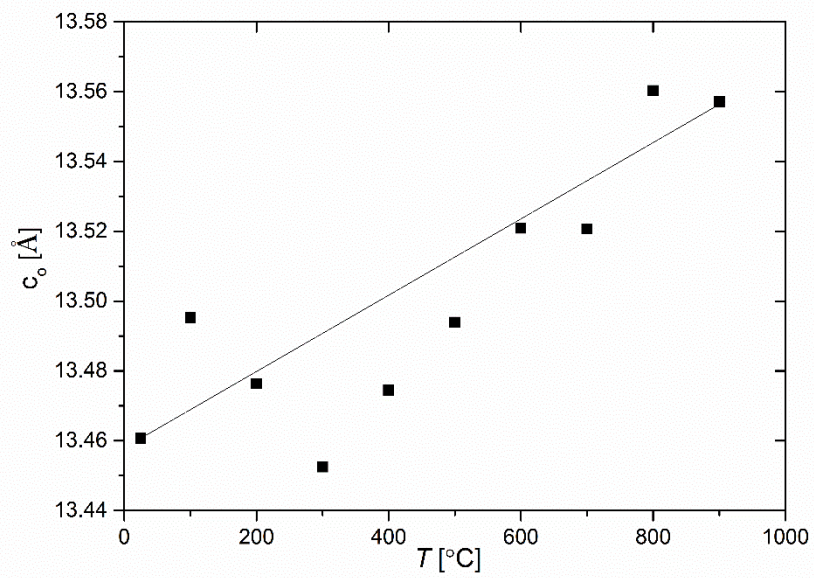


Figure 40: c_0 change with respect to temperature in LMO

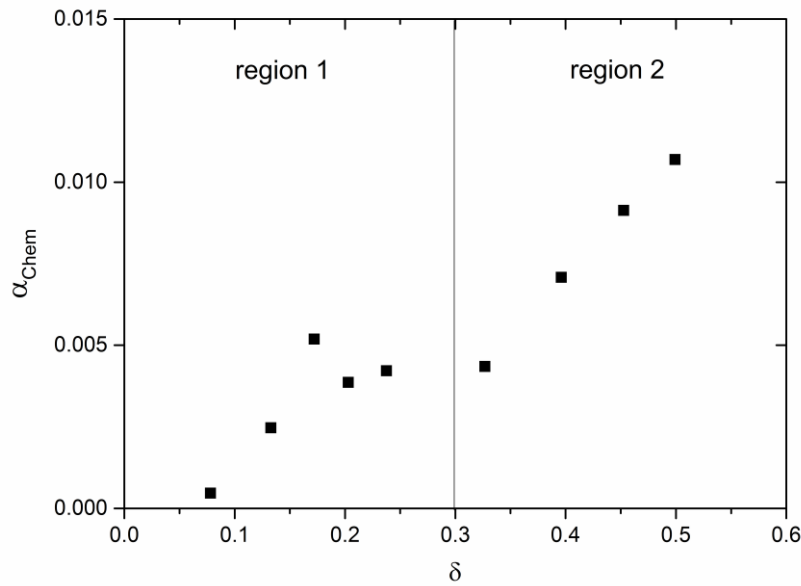


Figure 41: The relationship between α_{Chem} and δ in LMO

Due to anisotropy, α_{Chem} is calculated as 0.011 from a site of structure shown in Figure 39. In Figure 40, c site is shown and data is inharmonic to calculate α_{Chem} . Two regions are indicated in Figure 41. In region 1, the points on the graph are very scattered and sporadic, a linear relationship is observed in region 2 with an increasing slope. This value, where the increase in slope occurs, corresponds to Mn valency of 2.35+. Finally, the Mn increases of 2+ at the end of region 2.

In Figure 43, the chemical expansion coefficients could not be found because there is no order in c_0 values. However, in Figure 42, α_{Chem} was calculated as 0.006.

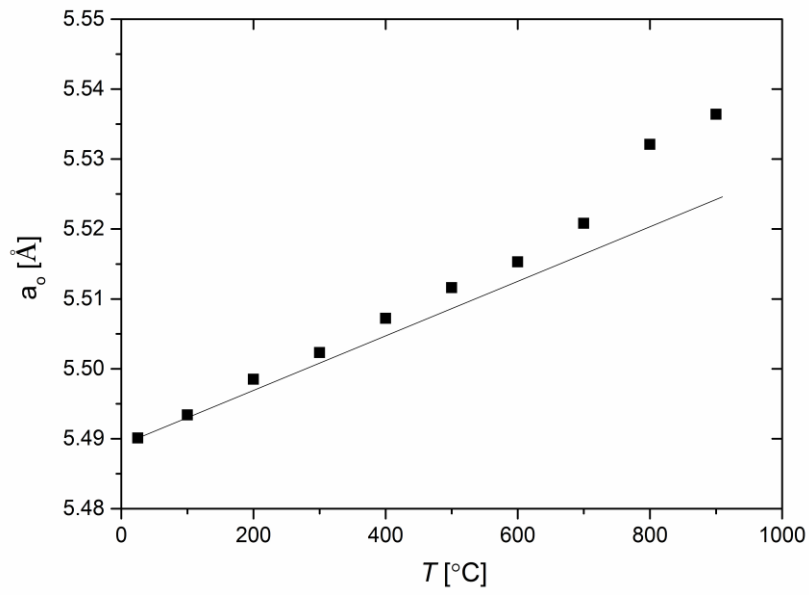


Figure 42: a_0 change with respect to temperature in LSMO1

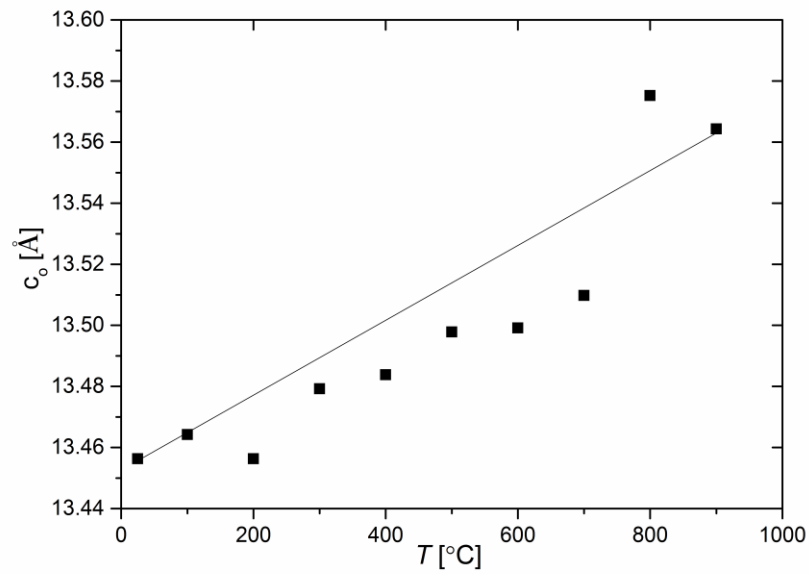


Figure 43: c_0 change with respect to temperature in LSMO1

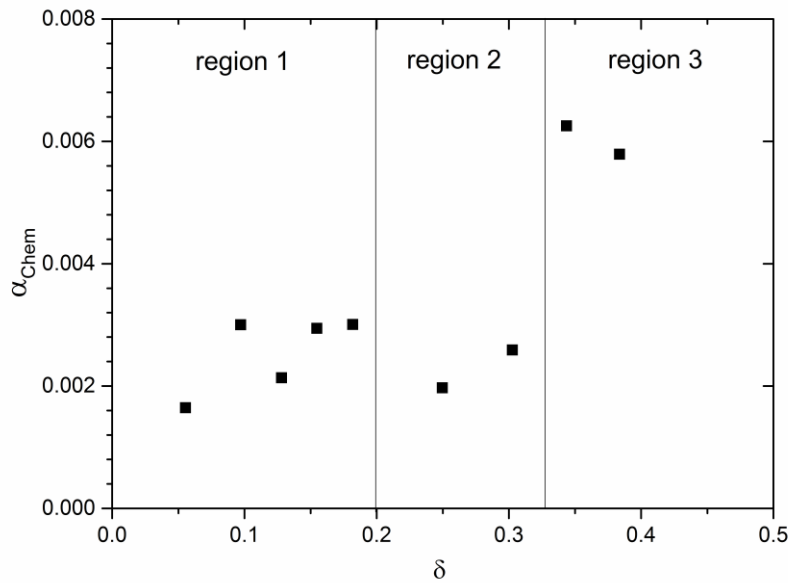


Figure 44: The relationship between α_{Chem} and δ in LSMO1

Three regions are indicated in the Figure 44. In region 1, the points on the graph are very scattered and sporadic, a linear relationship is observed in region 2 and the slope of the line increases. In region 3, there is a decrease in chemical expansion with increasing δ . Mn valence state becomes 2.34+ at the end of region 3. The decrease in chemical expansion in region 3 is experimental error.

In Figure 46, the chemical expansion coefficients could not be found because there is no order in c_0 values. However, in Figure 45, α_{Chem} was calculated as 0.009.

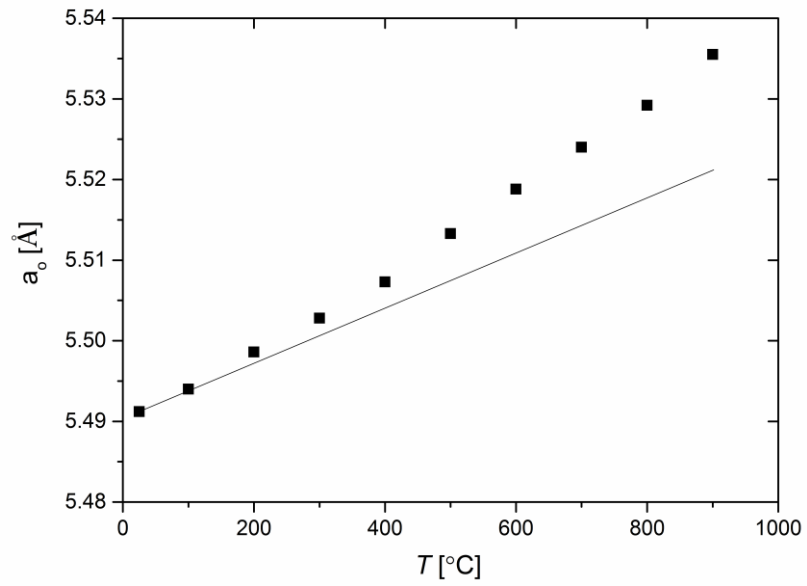


Figure 45: a_0 change with respect to temperature in LSMO2

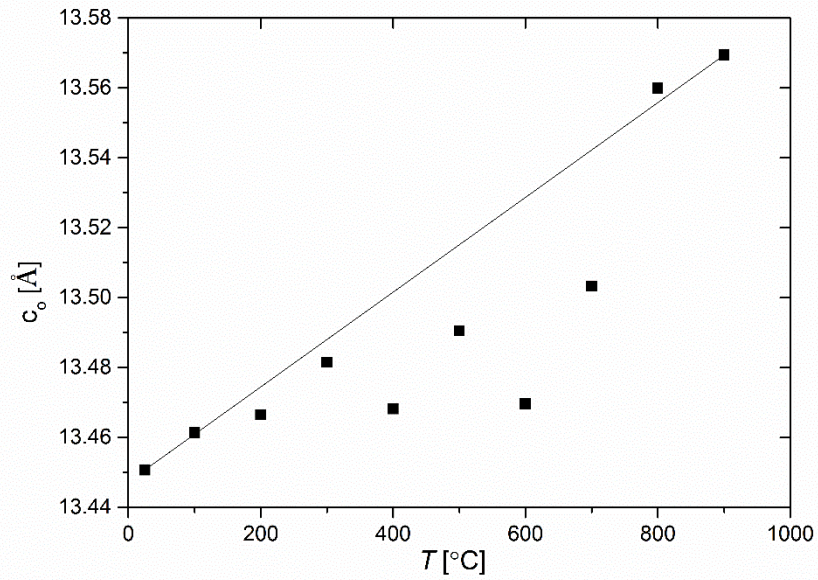


Figure 46: c_0 change with respect to temperature in LSMO2

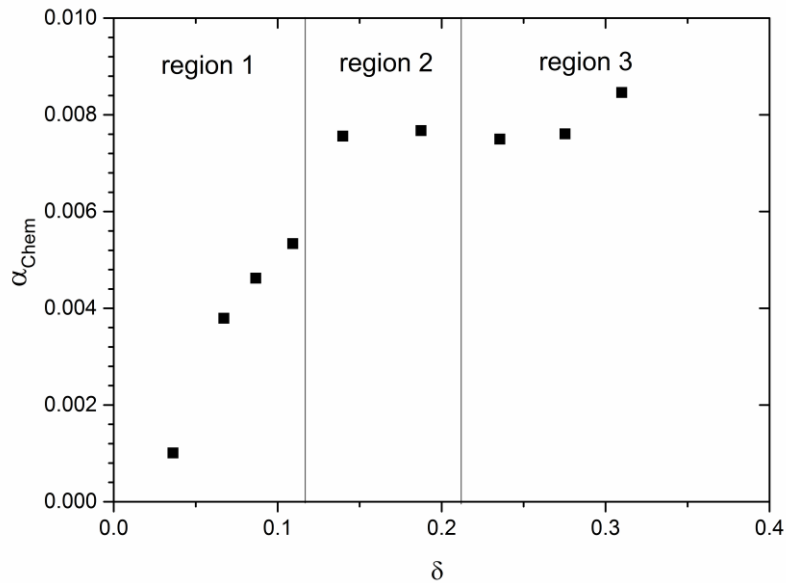


Figure 47: The relationship between α_{Chem} and δ in LSMO2

Three regions are indicated in the Figure 47. In region 1 and 2, a linear relationship is observed at different slopes and region 1 has higher slope than region 2. In region 3, increase in chemical expansion is parabolic. Mn valence state becomes 2.58+ at the end of region 3.

In Figure 49, the chemical expansion coefficients could not be found because there is no order in c_0 values. However, in Figure 48, α_{Chem} was calculated as 0.002. Two regions are indicated in the Figure 50. In region 1, the points on the graph are very scattered and sporadic, a linear relationship is observed in region 2 and the slope of the line is almost constant. Mn valence state becomes 2+ at the end of region 2.

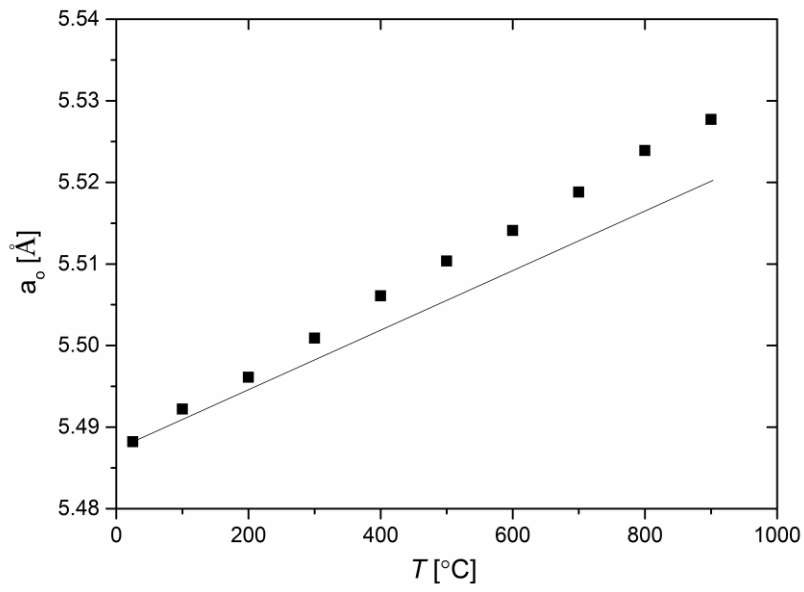


Figure 48: a_0 change with respect to temperature in LSMO3

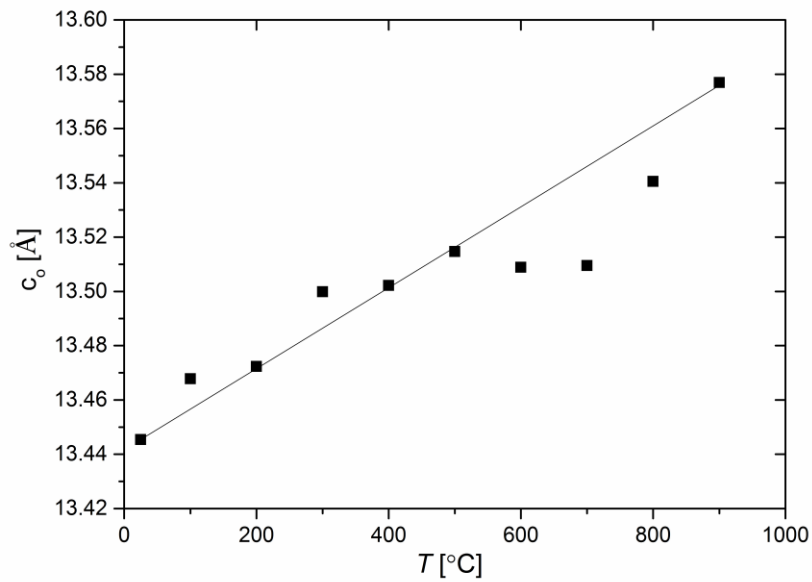


Figure 49: c_0 change with respect to temperature in LSMO3

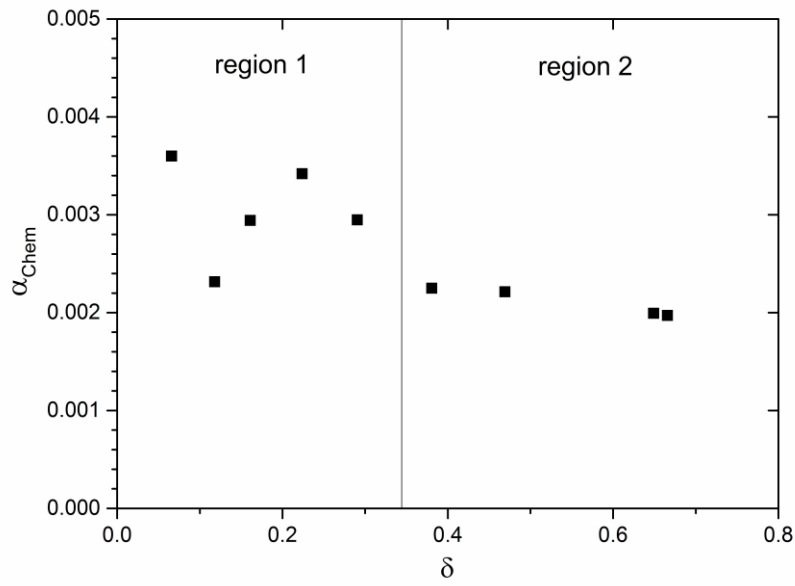


Figure 50: The relationship between α_{Chem} and δ in LSMO3

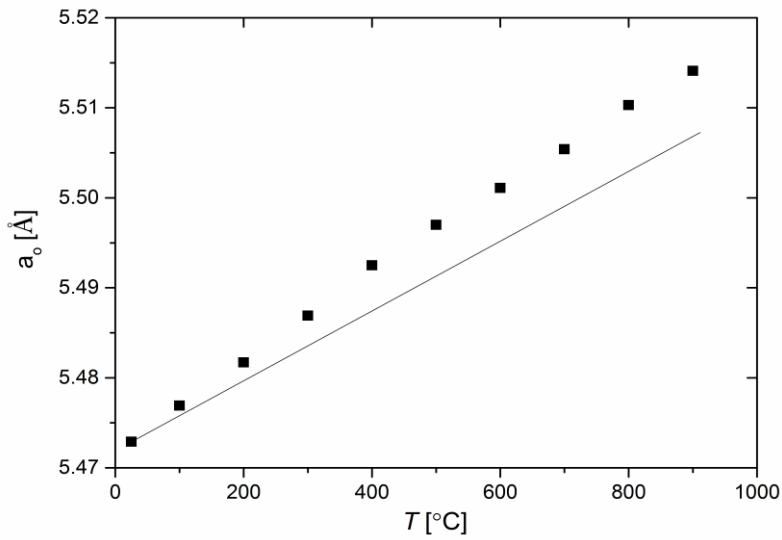


Figure 51: a_0 change with respect to temperature in LSMO4

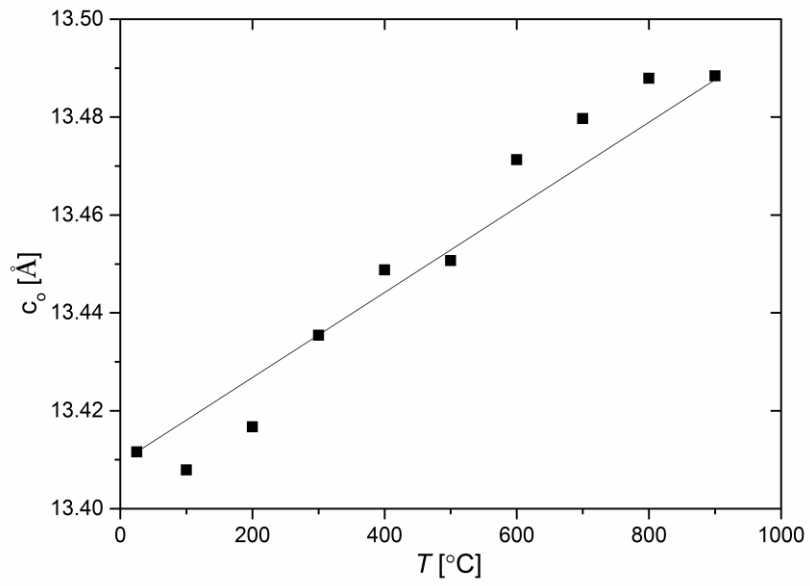


Figure 52: c_0 change with respect to temperature in LSMO4

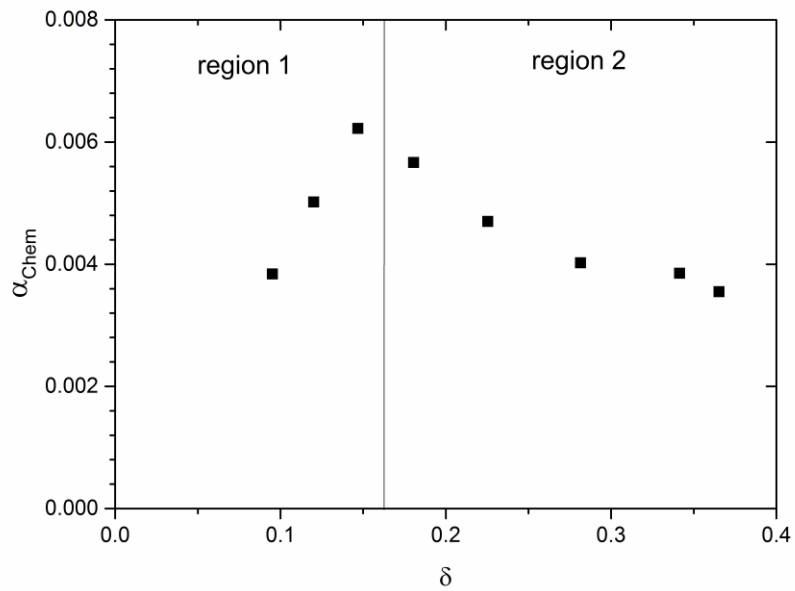


Figure 53: The relationship between α_{Chem} and δ in LSMO4

In-situ XRD was employed to find out total strain when it is heated up. Figure 52, the chemical expansion coefficients could not be found because there is no order in c_0 values. However, in Figure 51, α_{Chem} was calculated as 0.004.

Two regions are indicated in the Figure 53. In region 1, a linear relationship is observed with increasing slope and in region 2, there is almost linear relationship and it has decreasing slope. Mn valence state becomes 2.67+ at the end of region 2.

α_{Chem} in a site of crystal structure is calculated as 0.007 which is shown in Figure 54. However, in Figure 55, values are sporadic for calculation of chemical expansion coefficient.

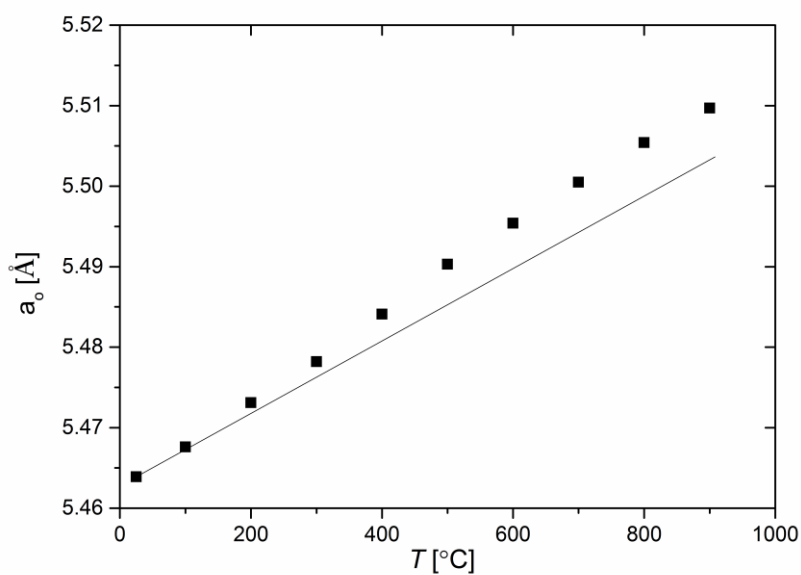


Figure 54: a_0 change with respect to temperature in LSMO5

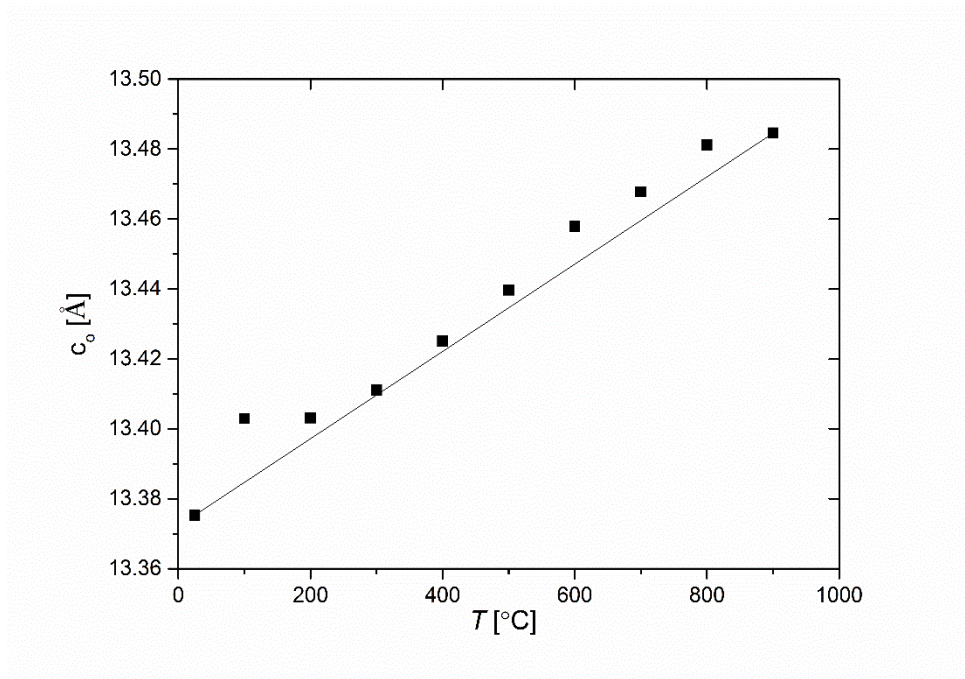


Figure 55: c_0 change with respect to temperature in LSMO5

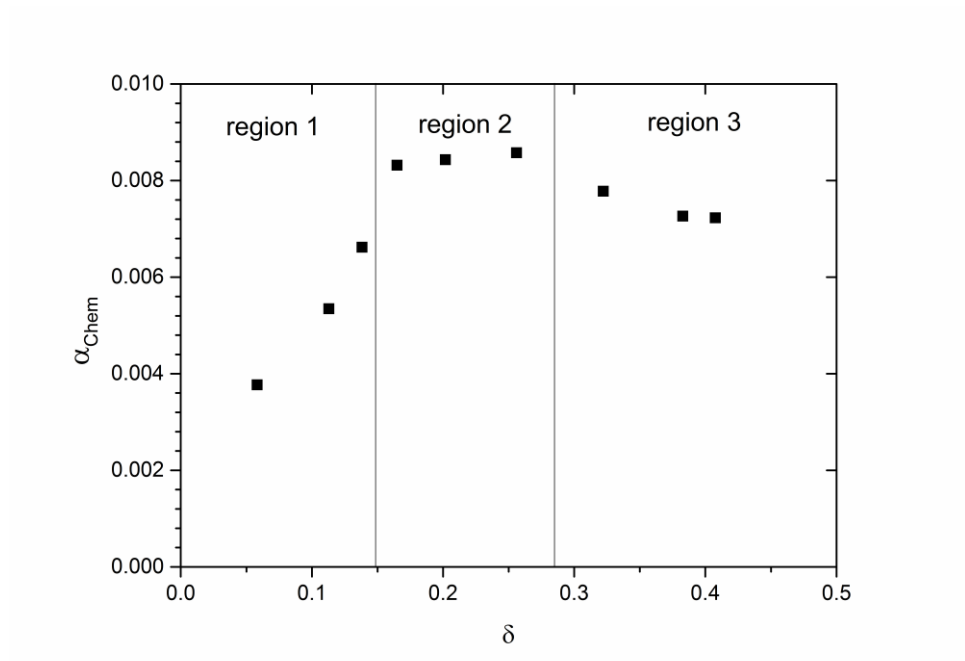


Figure 56: The relationship between α_{Chem} and δ in LSMO5

Three regions are indicated in Figure 56. In region 1, a linear relationship is observed with increasing slope and in region 2, slope is almost zero and it has constant value. In region 3, decreasing slope is observed. Mn valence state becomes 2.68+ at the end of region 3.

In Figure 58, the chemical expansion coefficients are zero because the only change in c_0 values is due to thermal expansion. However, in Figure 57, α_{Chem} was calculated as 0.005.

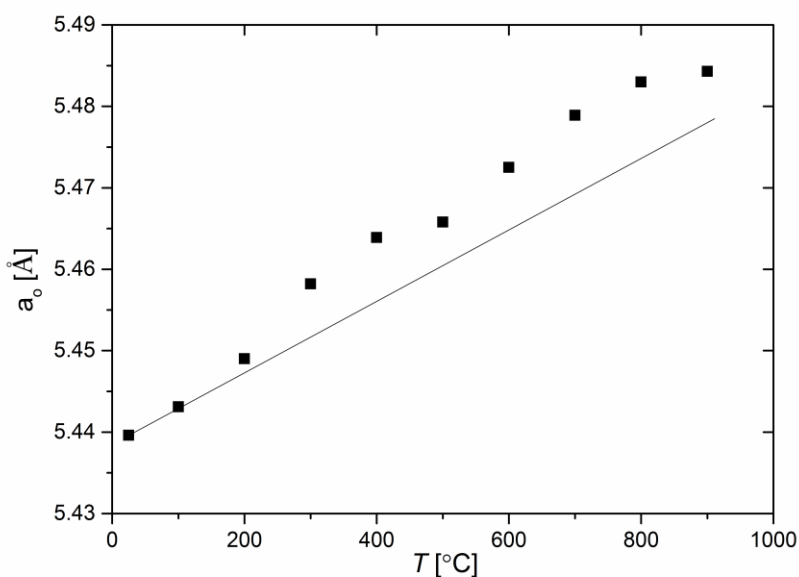


Figure 57: a_0 change with respect to temperature in LSMO6

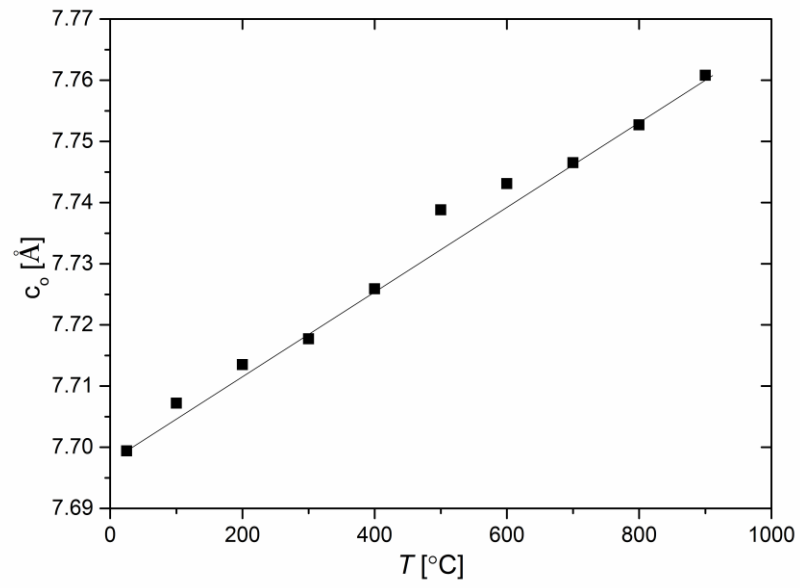


Figure 58: c_0 change with respect to temperature in LSMO6

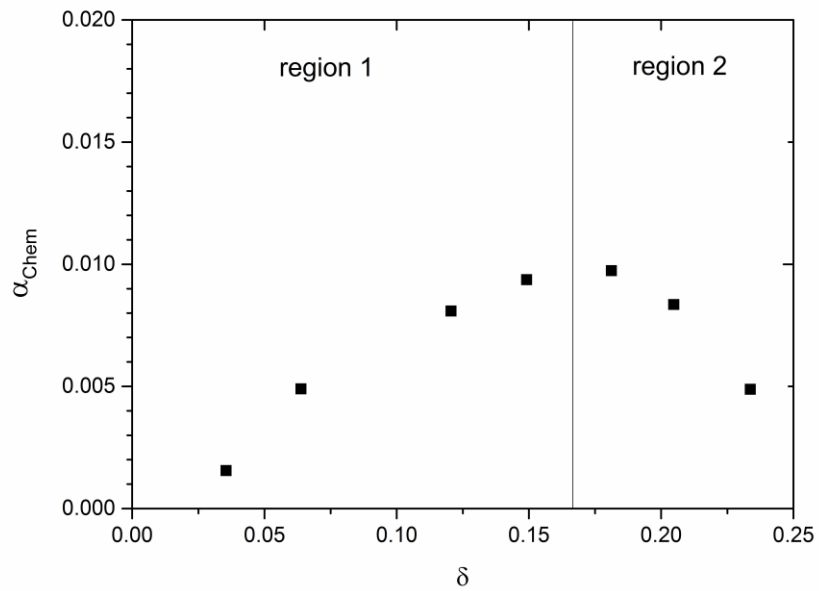


Figure 59: The relationship between α_{Chem} and δ in LSMO6

Two regions are indicated in the Figure 59. In region 1, a linear relationship is observed with increasing slope and in region 2, linear and decreasing slope is observed. Mn valence state becomes 3.13+ at the end of region 2.

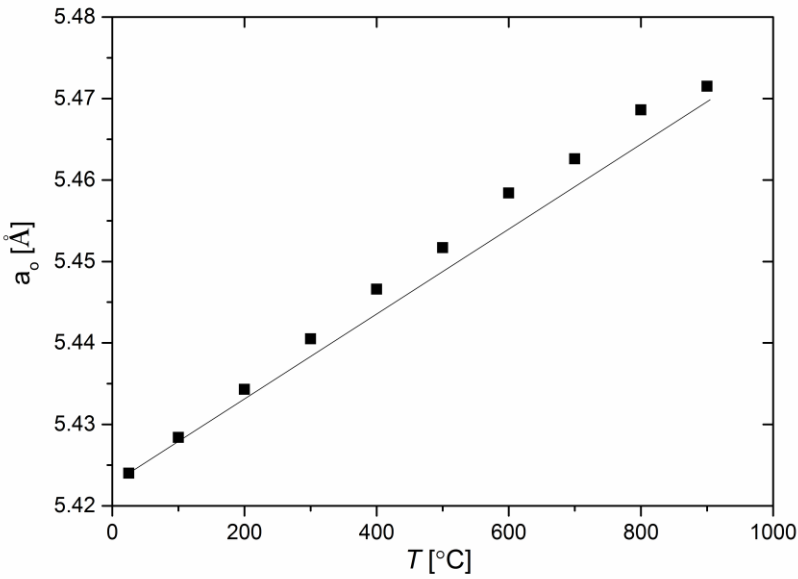


Figure 60: a₀ change with respect to temperature in LSMO7

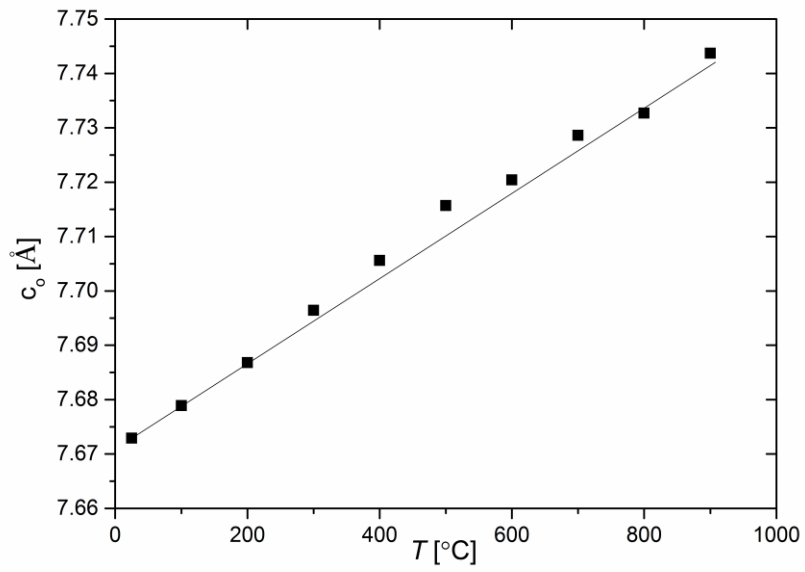


Figure 61: c_0 change with respect to temperature in LSMO7

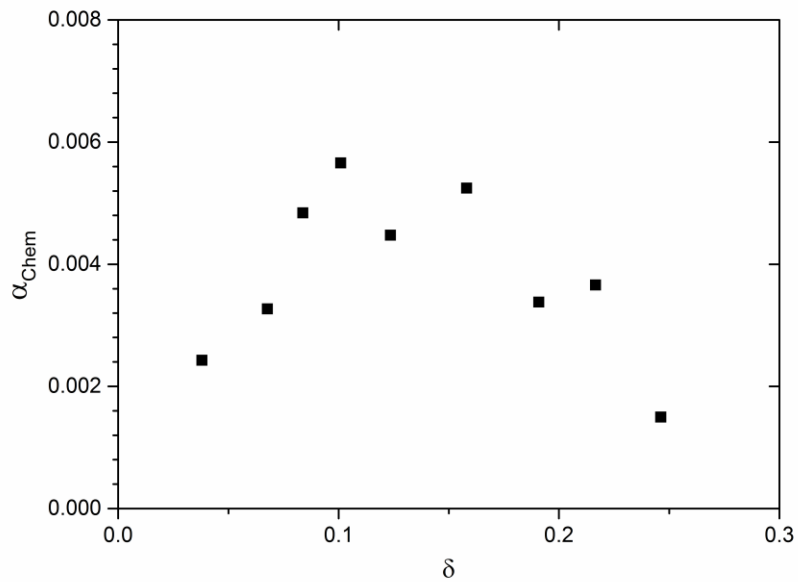


Figure 62: The relationship between α_{Chem} and δ in LSMO7

In Figure 61, the chemical expansion coefficients are zero because the only change in c_0 values is due to thermal expansion. However, in Figure 60, α_{Chem} was calculated as 0.002.

Figure 62 demonstrates the relationship between α_{Chem} and δ . It can be seen that there is no clear region and all graphs have sporadic points. Mn valence state becomes 3.21+ at the end of region 2.

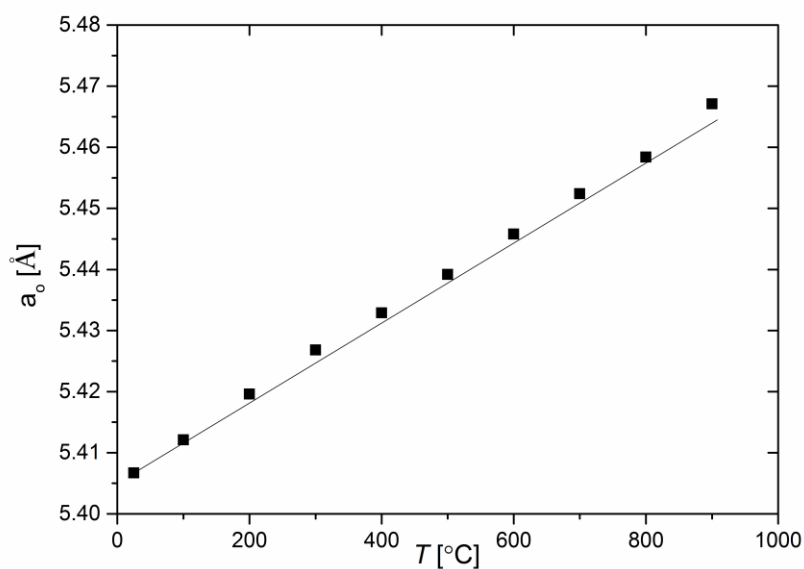


Figure 63: a_0 change with respect to temperature in LSMO8

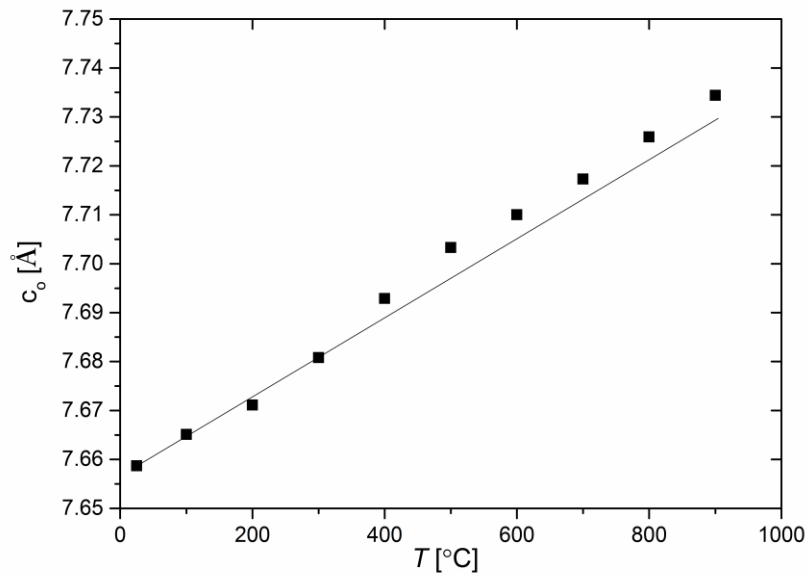


Figure 64: c_0 change with respect to temperature in LSMO8

In Figure 64, the chemical expansion coefficients are zero because the only change in c_0 values is due to thermal expansion. However, in Figure 63, α_{Chem} was calculated as 0.002.

Figure 65 demonstrates the relationship between α_{Chem} and δ . There is two main region at the figure. Region 1 shows experimental error because lower δ do not result with increasing chemical expansion. Region 2 is constant chemical expansion region and Mn valence state becomes 3.36+ at the end.

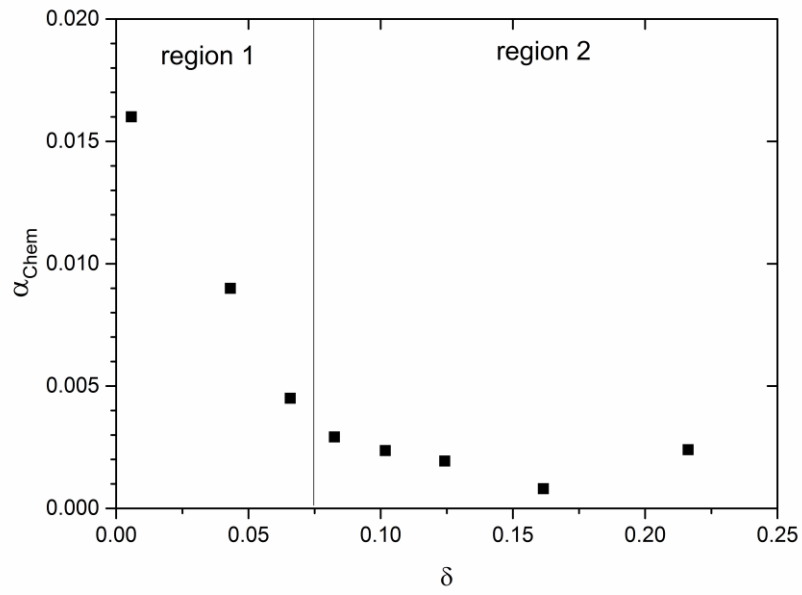


Figure 65: The relationship between α_{Chem} and δ in LSMO8

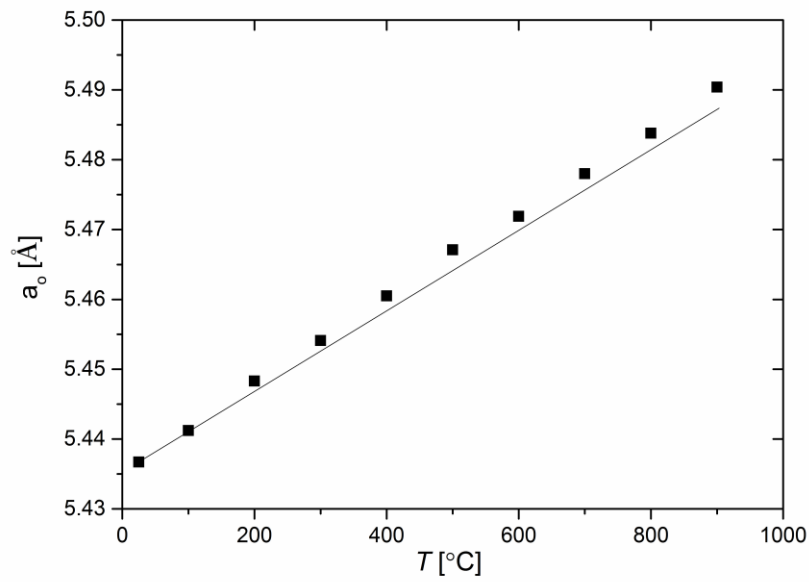


Figure 66: a_0 change with respect to temperature in LSMO9

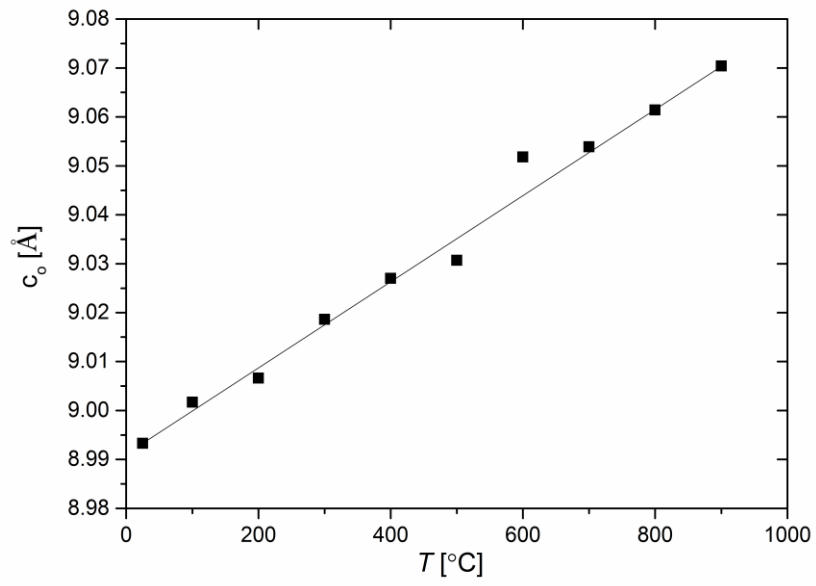


Figure 67: c_0 change with respect to temperature in LSMO9

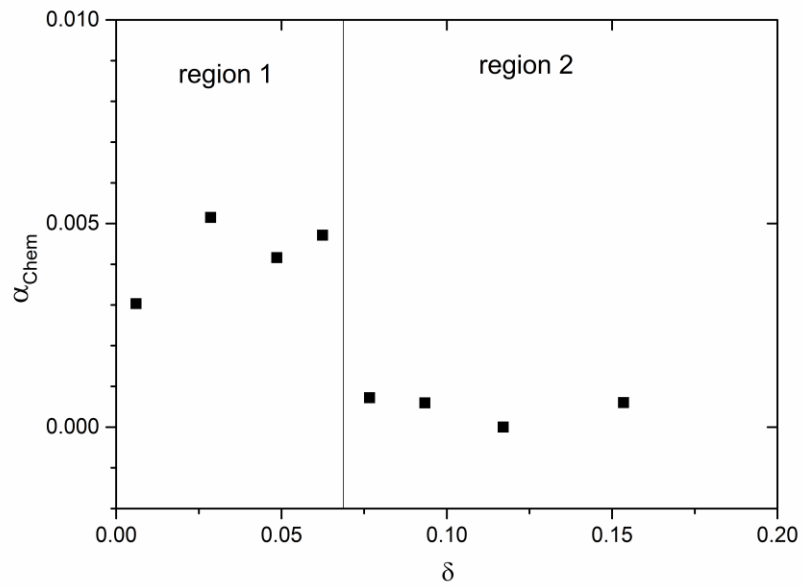


Figure 68: The relationship between α_{Chem} and δ in LSMO9

In Figure 67, the chemical expansion coefficients are zero because the only change in c_0 values is due to thermal expansion. However, in Figure 66, α_{Chem} was calculated as 0.0004 which is almost 0.

Figure 68 demonstrates the relationship between α_{Chem} and δ . There is two main region at the figure. Region 1 shows experimental error because lower δ do not result with increasing chemical expansion. Region 2 is constant chemical expansion region and Mn valence state becomes 3.6+ at the end.

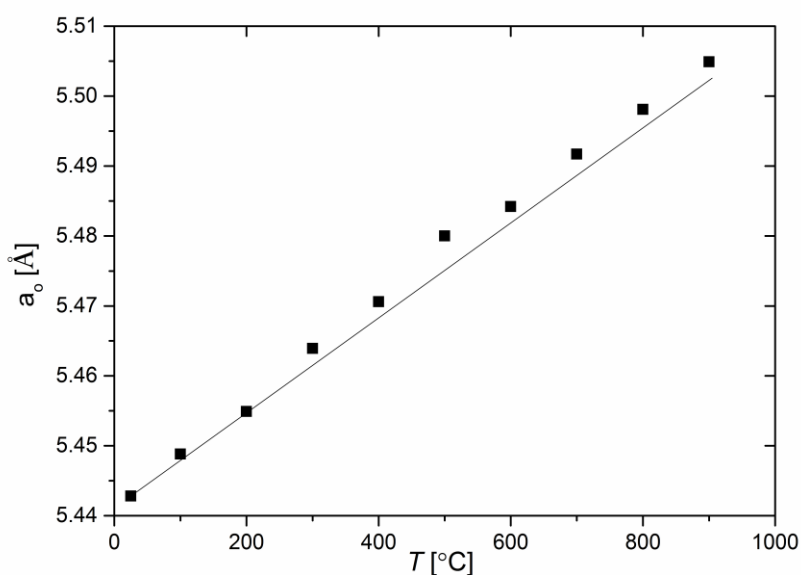


Figure 69: a_0 change with respect to temperature in SMO

In Figure 70, the chemical expansion coefficients could not be found because there is no order in c_0 values. However, in Figure 69, α_{Chem} was calculated as 0.003.

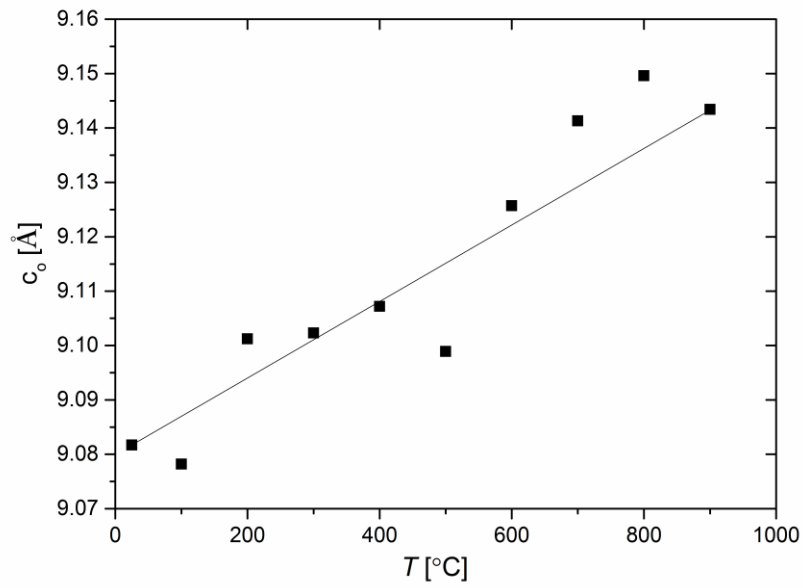


Figure 70: c_0 change with respect to temperature in SMO

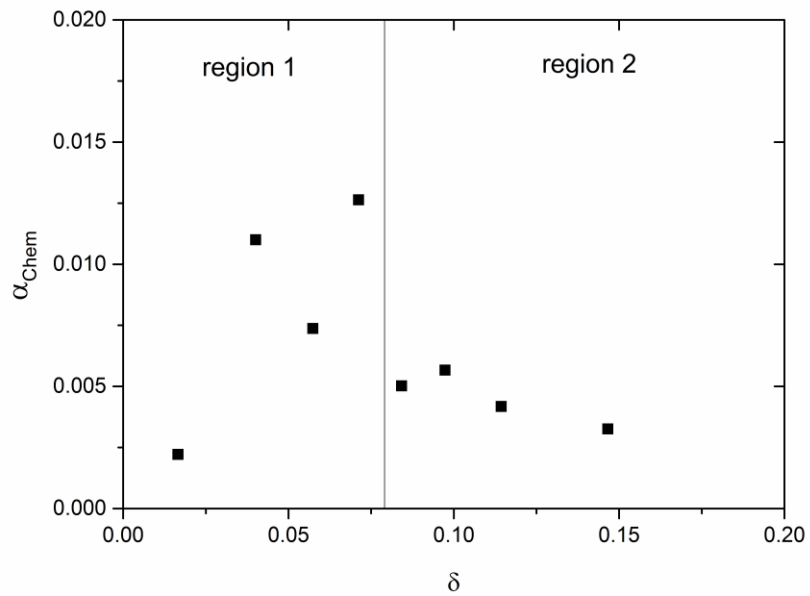


Figure 71: The relationship between α_{Chem} and δ in SMO

Figure 71 demonstrates the relationship between α_{Chem} and δ . There is two main region at the figure. Region 1 shows experimental error. Region 2 is constant chemical expansion region and Mn valence state becomes 3.7+ at the end.

6.3 Scanning Electron Microscope (SEM) Analysis

SEM analysis is employed to reveal the morphological changes before and after during in-situ XRD experiments.

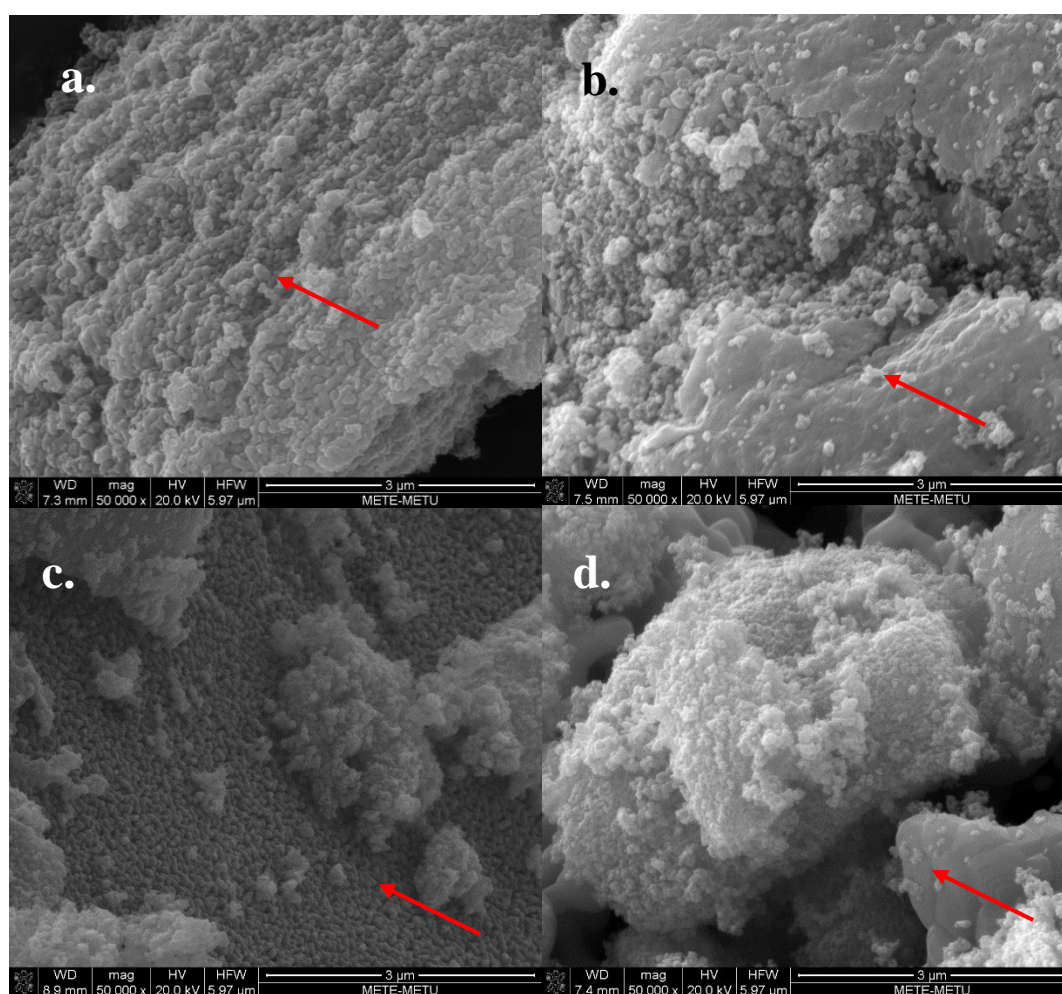


Figure 72: SEM images of a. LMO-As synthesized b. LMO-After experiment
c. LSMO1-As synthesized d. LSMO1-After experiment

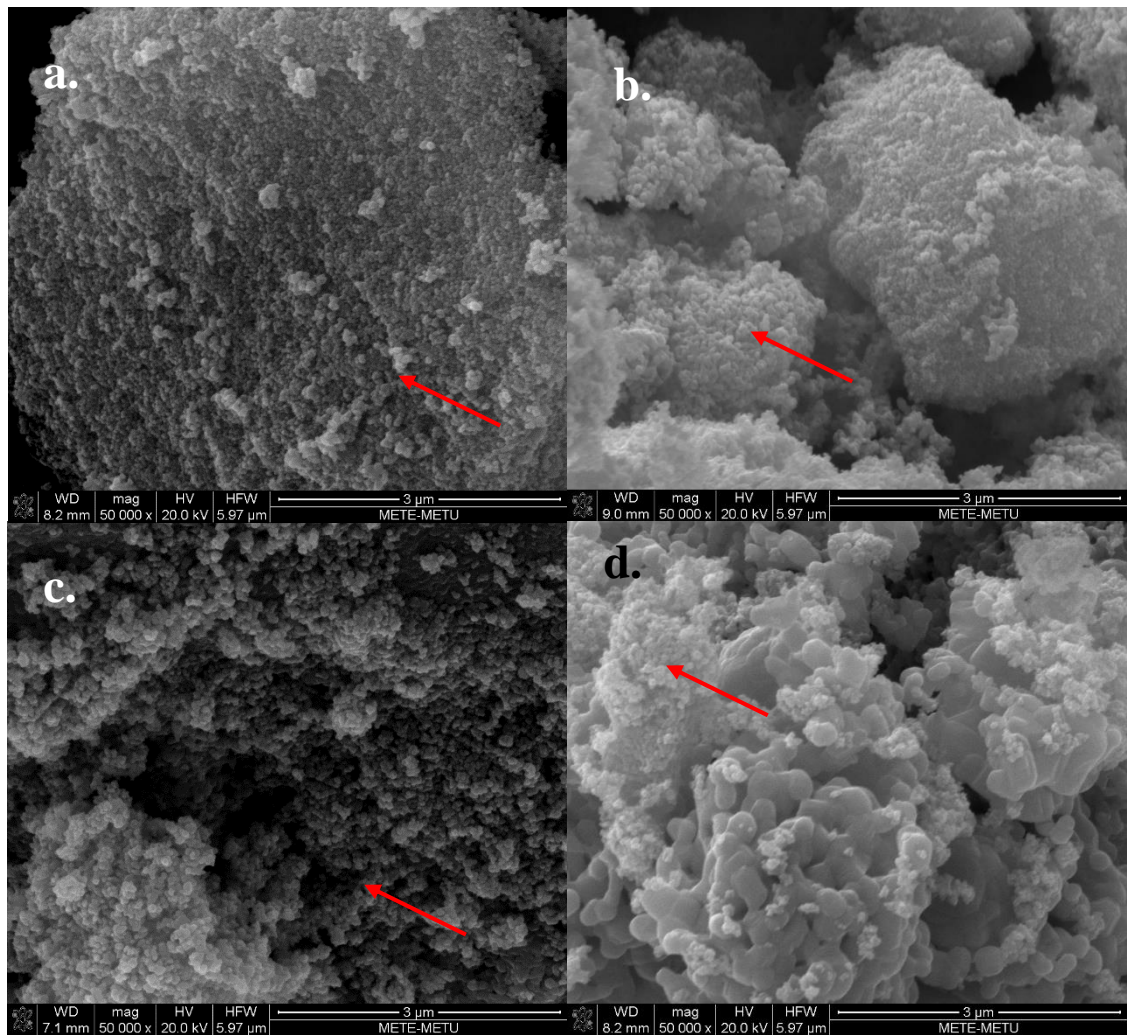


Figure 73: SEM images of a.LSMO2-As synthesized b.LSMO2-After experiment
c.LSMO3-As synthesized d.LSMO3-After experiment

As it can be observed from Figure 72 and Figure 73, calcined LMO, LSMO1, LSMO2 and LSMO3 nanopowders can be synthesized because lower calcination temperature was applied those powders. After treatment, nanopowders and some sintered region have been found. This is because temperatures higher than calcination temperature will cause sintering of nanopowders. Moreover, SEM images demonstrates that there are more surface area and it provides large area for oxygen release.

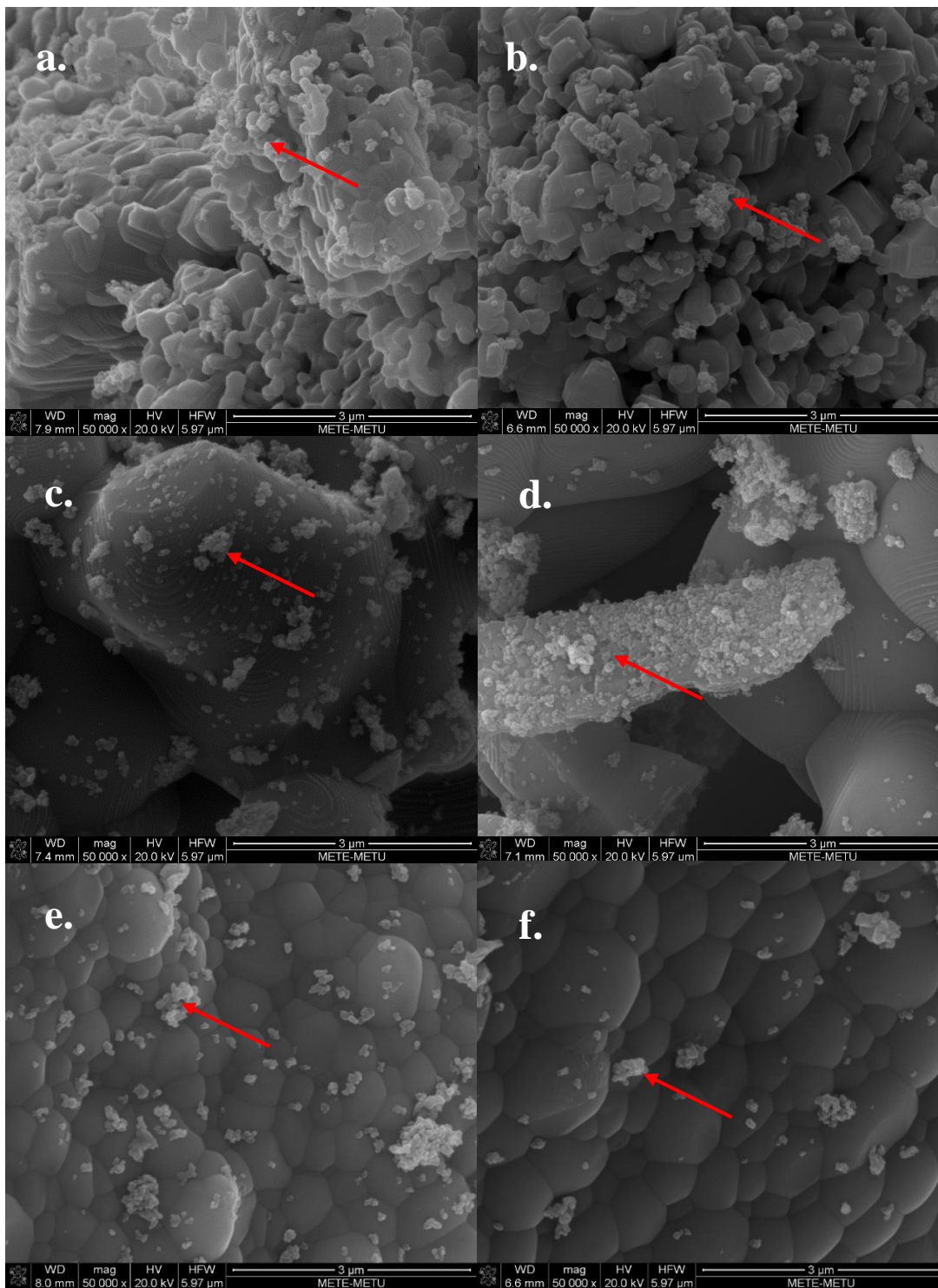


Figure 74: SEM images of a. LSMO4-As synthesized b. LSMO4-After experiment c. LSMO5-As synthesized d. LSMO5-After experiment e. LSMO6-As synthesized f. LSMO6-After experiment

LSMO4, LSMO5 and LSMO6 as synthesized samples are produced as mixture of sintered and nanopowders. LSMO4 samples are calcined lower temperature than LSMO5 and LSMO6. It can be observed in Figure 74. At same magnification LSMO5 and LSMO6 have more sintered regions. After high temperature experiments, amount of nanopowders decrease gradually due to sintering. α_{Chem} values can be changed due to calcination temperatures because sintering directly affects surface area of samples. Decreasing surface area means lower oxygen release.

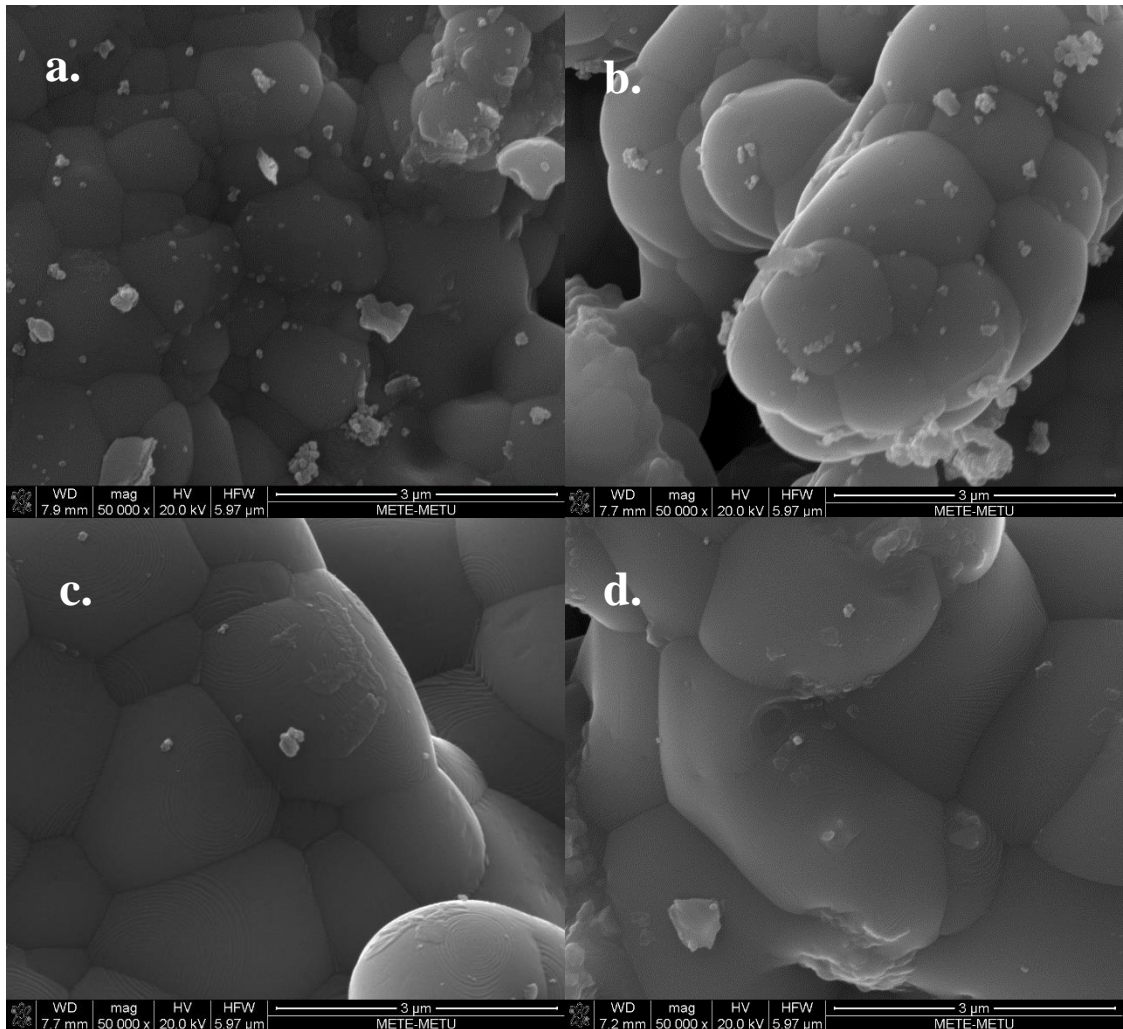


Figure 75: SEM images of a. LSMO7-As synthesized b. LSMO7-After experiment
c. LSMO8-As synthesized d. LSMO8-After experiment

From LSMO7 to SMO, all samples are calcined at relatively high temperatures. As a result, almost no nanopowders are observed in SEM images which is shown in Figure 75 and Figure 76. After in situ XRD experiments, there is no change morphology of the images because samples are already sintered after calcination. In sintered regions, there will be less oxygen release and chemical expansion value is expected to be low.

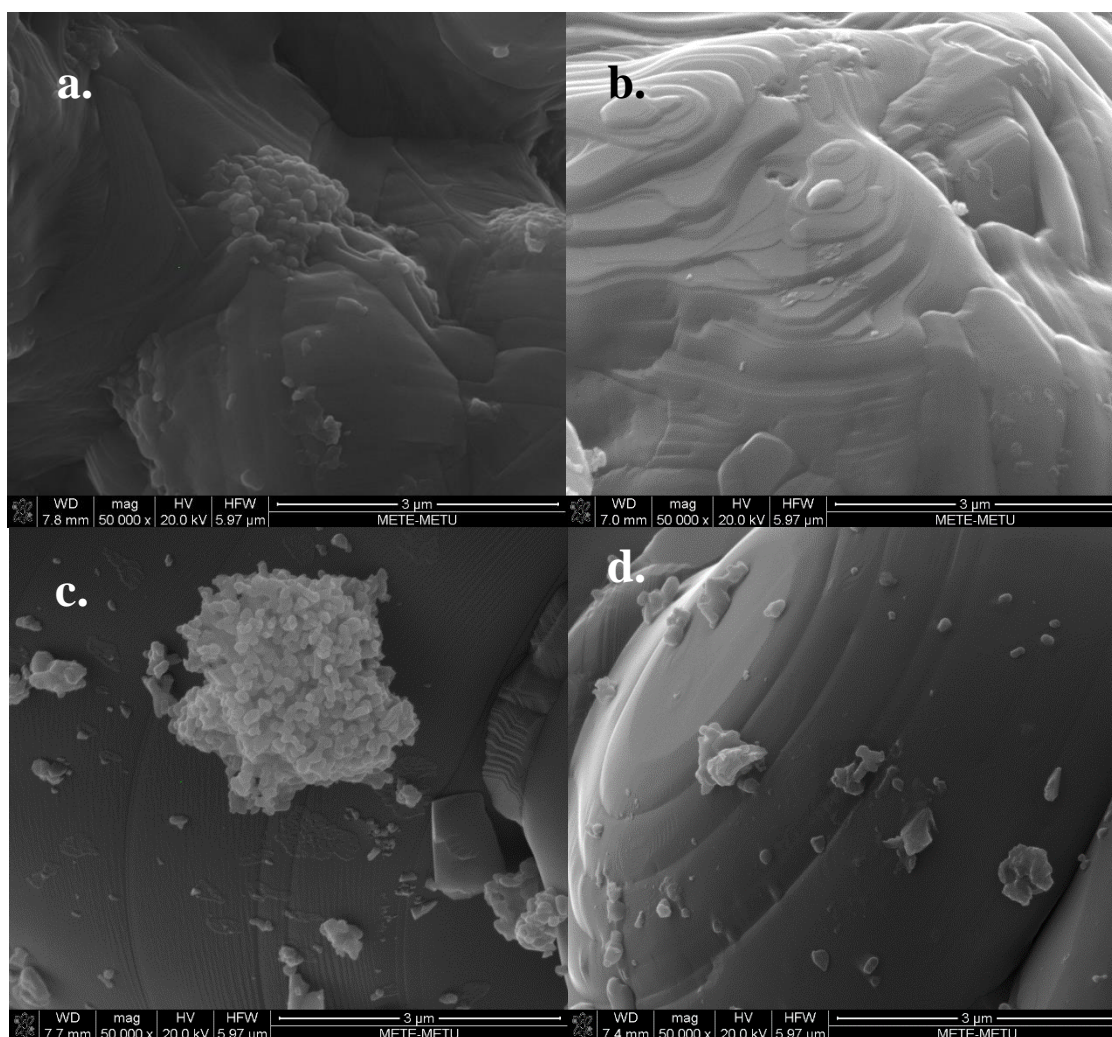


Figure 76: SEM images of a. LSMO9-As synthesized b. LSMO9-After experiment
c. SMO-As synthesized d. SMO-After experiment

6.4 Discussion about TGA Slope Changes

Slope changes are observed in weight loss vs. temperature diagrams. Some samples have the same slope change. There are some hypothesis about slope change. First, this slope changes are not related with only structure because all rhombohedral structures should demonstrate same change but they do not. Second, it has been proven that no phase change occurs during in situ XRD and DTA for all samples. Third, Sr substitution may cause slope changes, however, slope changes are seen in LMO samples which do not have Sr. Fourth, from Rietveld refinement analysis, Mn-O bond lengths were measured but no relationship was found. After eliminating these possibilities, it can be more clear to understand slope changes if the oxygen vacancy and manganese valency values are tabulated.

Table 6: Slope changes from LMO to LSMO2

Slope Change	Temperature (°C)	δ	Mn Valency
LMO	485	0.25	2.5
LSMO1	485	0.176	2.75
LSMO2	470	0.13	2.94

Table 7: Slope changes from LSMO4 to SMO

	Temp	δ	Mn	Temp	δ	Mn	Temp	δ	Mn
LSMO4	185	0.088	3.22	475	0.17	3.05	730	0.318	2.76
LSMO5	185	0.106	3.29	540	0.23	3.03	730	0.358	2.78
LSMO6	185	0.06	3.48	680	0.177	3.25			
LSMO7	205	0.07	3.56	640	0.176	3.35			
LSMO8	325	0.05	3.7	780	0.15	3.50			
LSMO9	325	0.035	3.83	780	0.11	3.70			
SMO	325	0.045	3.91	780	0.11	3.78			

It can be seen in Table 6, from LMO to LSMO2 slope change may be due to Jahn-Teller distortion (MnO_6 geometry change) which lowers the energy of the system causing more oxygen vacancy formation. Also, from LMO to LSMO2, between 470 °C and 485 °C, the differences between slopes from LMO to LSMO2 after 470 °C and 485 °C is reduced. This may be increase of Sr that may affect MnO_6 octahedra.

For LSMO3, two slope changes occur just before Mn valence state alters from +3 to +2 at 325°C and from +2 and +1 at 800°C. Changes in valence state may affect the oxygen vacancy formation.

In Table 7, slope changes from LSMO4 to SMO is demonstrated. For LSMO4 and LSMO5, at 730°C, Mn valence state is almost same and this causes slope changes but the reason is unknown with current studies. At 475 °C and 540 °C, Mn valence state becomes 3+ and presence of 2+ Mn may increase the oxygen vacancy formation. From LSMO6 to SMO, the changes of δ and Mn valence state are demonstrated but from the values there is no clear explanation for slope changes.

For all materials, it can be said that Jahn-Teller distortion may affect the structure of the samples and as a result, there may be increase or decrease in oxygen vacancy formation. To prove that, molecular dynamics simulation or in-situ transmission electron microscopy should be applied.

6.5 High Temperature Investigation for LCMO5 and LSMO Series

In results and discussion part above chapters are related with the calculation of coefficient of chemical expansion. The main purpose of this project was stated as to calculate chemical expansion and to see effect of Sr doping. Figure 77 and Figure 78 demonstrates δ vs. Sr % and α_{Chem} vs. Sr %. From the figures, it can be said that besides LSMO3, oxygen deficiency decreases with increasing Sr doping. LSMO9 and SMO have almost same δ values. That means at some point, Sr doping do not result with decreasing δ . Also α_{Chem} values have decreasing trend with increasing Sr

doping but not straight order. There are some anomalous α_{Chem} values. As a result, LSMO9 has the lowest chemical expansion value. Sr acts as agent for decreasing chemical expansion however, SMO has larger value than LSMO9. This points out SMO is not enough for decreasing chemical expansion. Higher Sr and Lower La amount results with lowest chemical expansion.

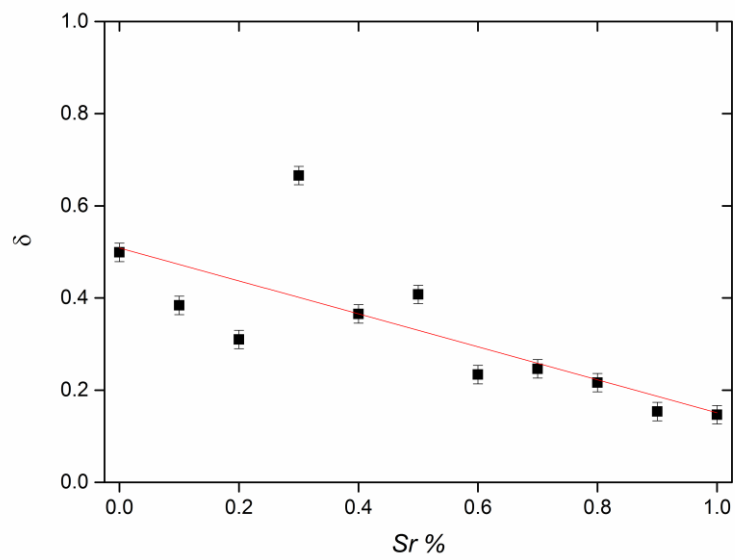


Figure 77: δ with respect to Sr %

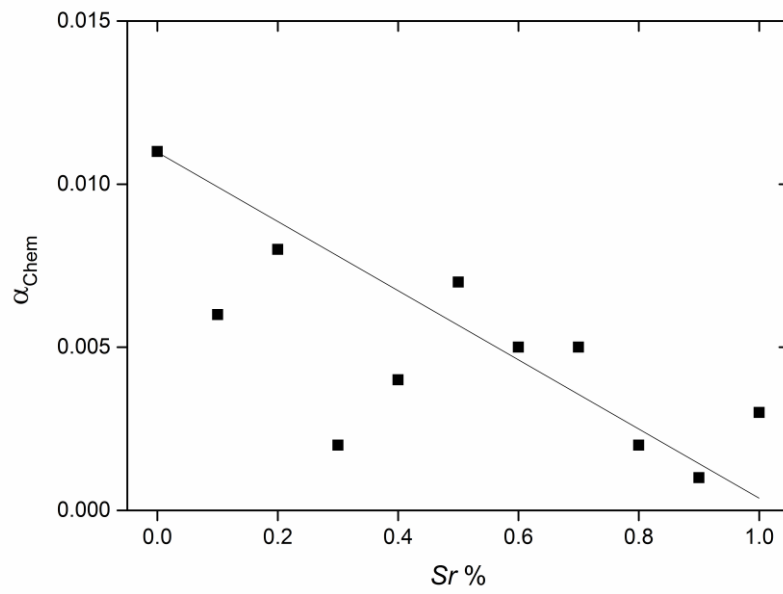


Figure 78: α_{Chem} changes with respect to Sr %

CHAPTER 7

CONCLUSION & FUTURE RECOMMENDATIONS

7.1 Conclusion

In this study, chemical expansion of manganites was investigated in detail by using thermal and diffraction techniques. Results indicated that chemical expansion results from oxygen deficiency and manganese radius change in LCMO5 and LSMO series. The following conclusions were attained. LSMO series and LCMO5 were synthesized by Pechini method. Oxygen deficiency was calculated by performing TGA under high temperature and reducing environment (N₂ atmosphere). Room temperature XRD analysis revealed that synthesized powders are single phase materials. In-situ XRD analysis demonstrates that structural parameters such as lattice constants of substances altered with increasing temperature. Anomalous shift at the peaks justifies existence of chemical expansion. Dilatometry and in-situ XRD analysis on LCMO5 and LSMO series showed volume change in bulk and lattice which helps to calculate chemical expansion. Coefficient of chemical expansion values are found out and effect of Sr doping was observed both α_{Chem} and δ values. All in all, it has been proved that for calculation of chemical expansion values, LCMO5 and LSMO series were synthesized successfully by Pechini method and with several methods, α_{Chem} and δ values were found out. LSMO9 has the lowest α_{Chem} value.

7.2 Future Recommendations

Chemical expansion values are calculated with the help of thermal and diffraction analyses. In TGA curves, the slope changes cannot be clearly explained due to absence of additional data. In-situ X-ray Photoelectron Spectroscopy (XPS) or in-Situ Electron Energy Loss Spectroscopy (EELS) could be employed in order to find out the change in valence state of Mn such that the relationship between Mn valence state and TGA slope change could be clarified.

Pechini method is an easy way to produce mixed ionic electronic conductive oxides. However, during calcination, air atmosphere creates reductive environment which causes the ejection of oxygen from lattice. Any oxygen deficiency or cation deficiency on lattice can change the property of material. For example, high temperature superconductor YBCO provides significant information about effects of oxygen non-stoichiometry. The changes of oxygen deficiency (δ) between 0 and 1 results with structural and also electronic properties change. If δ is smaller than 0.65 superconductivity is observed. At higher δ values, the compound become semiconductor [65]. In this research, synthesized powders are accepted as fully stoichiometric however, generally, it should be controlled. By applying coulometric titration, one can determine Mn valence state and as a result, oxygen deficiency can be found out before experiments.

In this research, effect of temperature on chemical expansion coefficient under constant pressure is measured in TGA experiments. In addition to this, effect of pressure under isothermal heating can be applied and the behaviour of material can be understood.

Moreover, LSMO samples are calcined powders. In order to represent the service life, powders can be sintered as pellets. After that, experiments can be employed. Also, for dilatometry experiments, sintered pellets are needed.

Further investigations can be useful to understand the mechanisms of chemical expansion under various environments.

CHAPTER 8

REFERENCES

- [1] Q. G. Gong, C. Canedy, G. Xiao, J. Z. Sun, A. Gupta ve W. J. Gallagher, "Colossal magnetoresistance in the antiferromagnetic $\text{La}_{0,5}\text{Ca}_{0,5}\text{MnO}_3$ system", *Journal of Applied Physics*, volume 79, pp. 4538-4540, 1996.
- [2] S. Park, N. Hur, S. Guha ve S. -W. Cheong, "Percolative Conduction in the Half-Metallic-Ferromagnetic and Ferroelectric Mixture of $(\text{La}, \text{Lu}, \text{Sr})\text{MnO}_3$ ", *Physical Review Letters*, volume 92, p. 167206, 2004.
- [3] J. R. Frade , V. V. Kharton, A. Yaremchenko ve E. Naumovich, "Methane to syngas conversion Part I. Equilibrium conditions and stability requirements of membrane materials", *Journal of Power Sources*, volume 130, pp. 77-84, 2004.
- [4] R. Von Helmont, J. Wecker, B. Holzapfel, L. Schultz ve K. Samwer, "Giant Negative Magnetoresistance in Perovskite Like $\text{La}_{2/3}\text{Ba}_{1/3}\text{MnO}_x$ Ferromagnetic Films", *Physical Review Letters*, volume 71, p. 2331, 1993.
- [5] S. B. Adler, "Factors Governing Oxygen Reduction in Solid Oxide Fuel Cell Cathodes", *Chemical Reviews*, volume 104, p. 4791, 2004.
- [6] J. M. D. Coey, M. Viret ve S. Von Molnar, "Mixed-valence Manganites",

Advances in Physics, volume 48, pp. 167-293, 1999.

- [7] R. B. Gangineni, "Extrinsic Magnetotransport in Manganites and Its Dependence on Mechanical Strain", Göttingen: Cuvillier Verlag, 2008.
- [8] S. B. Adler, J. A. Lane ve B. C. H. Steele, "Electrode Kinetics of Mixed-Conducting Oxygen Electrodes", *Journal of Electrochemical Society*, volume 143, p. 3554, 1996.
- [9] M. Suigure, "Oxygen storage materials for automotive catalysts: ceria-zirconia solid solutions", *Catalysis Surveys from Asia*, volume 7, p. 77, 2003.
- [10] P. N. Dyer, R. E. Richards, S. L. Russek ve D. M. Taylor, "Ion transport membrane technology for oxygen separation and syngas production", *Solid State Ionics*, volume 134, pp. 21-33, 2000.
- [11] Y. Liu, X. Tan ve K. Li, "Mixed Conducting Ceramics for Catalytic Membrane Processing", *Catalysis Reviews: Science and Engineering*, volume 48, pp. 145-198, 2006.
- [12] Y. Kuru, M. Wohlschlögel, U. Welzel ve E. J. Mittemeijer, "Crystallite size dependence of the coefficient of thermal expansion of metals", *Applied Physics Letters*, volume 90, p. 243113, 2007.
- [13] D. Marrocchelli, S. R. Bishop, H. L. Tuller ve B. Yildiz, "Understanding Chemical Expansion in Non-Stoichiometric Oxides: Ceria and Zirconia Case Studies", *Advanced Functional Materials*, volume 22, pp. 1958-1965, 2012.
- [14] A. Atkinson, "Chemically-induced stresses in gadolinium-doped ceria solid oxide fuel cell electrolytes", *Solid State Ionics*, volume 95, pp. 249-258, 1997.
- [15] E. Blond ve N. Richet, "Thermomechanical modelling of ion-conducting membrane for oxygen separation", *Journal of the European Chemical Society*,

volume 28, pp. 793-801, 2008.

- [16] Y. Wang, K. Duncan, E. D. Wachsman ve F. Ebrahimi, "The effect of oxygen vacancy concentration on the elastic modulus of fluorite-structured oxides", *Solid State Ionics*, volume 178, pp. 53-58, 2007.
- [17] B. W. Sheldon ve V. B. Shenoy, "Space Charge Induced Surface Stresses: Implications in Ceria and Other Ionic Solids", *Physical Review Letters*, volume 106, p. 216104, 2011.
- [18] M. Mogensen, N. M. Sammes ve G. A. Tompsett, "Physical, chemical and electrochemical properties of pure and doped ceria", *Solid State Ionics*, volume 129, pp. 63-94, 2000.
- [19] V. Strbik ve S. Chromik, "Characterization of electrical transport in LSMO with enhanced temperature of metal-insulator transition", *Journal of Electrical Engineering*, volume 63, pp. 270-272, 2012.
- [20] P. -M. Geffroy, J. Fouletier, N. Richet ve T. Chartier, "Rational selection of MIEC materials in energy production processes", *Chemical Engineering Science*, volume 87, pp. 408-433, 2013.
- [21] Q. Shu, J. Zhang, B. Yan ve J. Liu, "Phase formation mechanism and kinetics in solid-state synthesis of undoped and calcium-doped lanthanum manganite", *Materials Research Bulletin*, volume 44, pp. 649-653, 2009.
- [22] M. Kakihana ve M. Yoshimura, "Synthesis and Characteristics of Complex Multicomponent Oxides Prepared by Polymer Complex Method", *Bulletin of Chemical Society of Japan*, volume 72, pp. 1427-43, 1999.
- [23] Q. Ming, M. D. Nersesyan, J. T. Richardson ve D. Luss, "A new route to synthesize $\text{La}_{1-x}\text{Sr}_x\text{MnO}_3$ ", *Journal of Materials Science*, volume 35, pp. 3599-3506, 2000.

- [24] W. L. Sin, K. H. Wong ve P. Li, "Surfactant Effect on Synthesis of Nanocrystalline $\text{La}_x\text{Sr}_{1-x}\text{MnO}_3$ by Hydrothermal Method", *Acta Physica Polonica A*, volume 111, pp. 165-171, 2006.
- [25] A. Ghosh, A. K. Sahu, A. K. Gulnar ve A. K. Suri, "Synthesis and characterization of lanthanum strontium manganite", *Scripta Materialia*, volume 52, pp. 1305-1309, 2005.
- [26] M. P. Pechini, "Method of preparing lead and alkaline earth titanates and niobates and coating method using the same to form a capacitor", USA Patent: 3330697, 11 July 1967.
- [27] M. Johansson ve P. Lemmens, "Crystallography and Chemistry of Perovskites".
- [28] Z. P. Shao ve S. M. Haile, "A High-Performance Cathode for the Next Generation of Solid-Oxide Fuel Cells", *Nature*, volume 431, pp. 170-3, 2004.
- [29] P. Datta, P. Majewski ve F. Aldinger, "Structural Studies of Sr- and Mg-Doped LaGaO_3 ", *Journal of Alloys and Compounds*, volume 438, pp. 232-7, 2007.
- [30] H. A. Jahn ve E. Teller, "Stability of Polyatomic Molecules in Degenerate Electronic States. I. Orbital Degeneracy", *Proceedings of The Royal Society A*, volume 161, pp. 220-235, 1937.
- [31] R. Bindu, "Structural Studies of $\text{La}_{1-x}\text{Sr}_x\text{MnO}_{3-\delta}$ ", *The European Physical Journal B*, volume 37, pp. 321-327, 2004.
- [32] A. Maignan, S. Hebert, P. Li, D. Pelloquin, C. Martin, C. Michel, M. Hervieu ve B. Raveau, "Perovskite manganites and layered cobaltites: potential materials for thermoelectric applications", *Crystal Engineering*, volume 5, pp. 365-382, 2002.
- [33] H. Sawada, Y. Morikawa, K. Terakura ve N. Hamada, "Jahn-Teller distortion

and magnetic structures in LaMnO_3 ", *Physical Review B*, volume 56, pp. 154-160, 1997.

- [34] M. V. Goldschmidt, "Die Gesetze der Krystallochemie", *Die Naturwissenschaften*, volume 21, pp. 477-485, 1926.
- [35] X. Chen ve T. Grande, "Anisotropic Chemical Expansion of $\text{La}_{1-x}\text{Sr}_x\text{CoO}_{3-\delta}$ ", *Chemistry of Materials*, volume 25, pp. 927-934, 2013.
- [36] J. M. Gonzalez-Carbet, E. Herrero, N. Rangavittal, J. M. Alonso, J. L. Martinez ve M. Vallet-Regi, "Ordering of Oxygen Vacancies and Magnetic Properties in $\text{La}_{0.5}\text{Ca}_{0.5}\text{MnO}_{3-\delta}$ ", *Journal of Solid State Chemistry*, volume 148, pp. 158-168, 1999.
- [37] R. V. Shpanchenko, V. V. Chernaya, A. A. Tsirlin, P. S. Chizhov, D. E. Sklovsky ve E. V. Antipov, "Synthesis, Structure, and Properties of New Perovskite PbVO_3 ", *Chemistry of Materials*, volume 16, no. 17, pp. 3267-73, 2004.
- [38] R. H. E. Van Doorn ve A. J. Burggraaf, "Structural aspects of the ionic conductivity of $\text{La}_{1-x}\text{Sr}_x\text{CoO}_{3-\delta}$ ", *Solid State Ionics*, volume 128, pp. 65-78, 2000.
- [39] C. C. Chou, C. L. Huang, S. Mukherjee, Q. Y. Chen, H. Sakurai, A. A. Belik, E. Takayama-Muromachi ve H. D. Yang, "Multiple magnetic transitions in multiferroic BiMnO_3 ", *Physical Review B*, volume 80, no. 18, p. 184426, 2009.
- [40] S. Pathak, "Manganites: phenomenology, present understanding and future prospects", India.
- [41] S. Jin, T. H. Tiefel, M. McCormack, H. M. O'Bryan, L. M. Chen, R. Ramesh ve D. Schurig, "Thickness dependence of magnetoresistance in La-Ca-Mn-O

- epitaxial films", *Applied Physics Letters*, volume 67, pp. 557-559, 1995.
- [42] Y. F. Yang ve K. Held, "Localization of strongly correlated electrons as Jahn-Teller polarons in manganites", *Physical Review B*, volume 76, p. 212401, 2007.
- [43] C. Zener, "Interaction between the d-shells in the transition metals. 2. ferromagnetic compounds of manganese with perovskite structure", *Physical Review*, volume 82, no. 3, pp. 403-405, 1951.
- [44] A. J. Jacobson, "Materials for Solid Oxide Fuel Cells", *Chemistry of Materials Review*, volume 22, pp. 660-674, 2009.
- [45] "Web Elements Periodic Table", The University of Sheffield and WebElements Ltd., 1993. [Online]. Available: <http://www.webelements.com/>. [Received: 10 January 2015].
- [46] T. R. Armstrong, J. W. Stevenson, L. R. Pederson ve P. E. Raney, "Dimensional instability of doped lanthanum chromite", *Journal of the electrochemical society*, volume 143, pp. 2919-25, 1996.
- [47] F. L. Tang, M. Huang, W. J. Lu ve W. Y. Yu, "Structural relaxation and Jahn-Teller distortion of LaMnO₃ (001) surface".
- [48] B. B. Van Aken, A. Meetsma ve T. T. M. Palstra, "La-site shift as probe for Jahn-Teller effect", *Condensed Matter*, 2001.
- [49] J. Hemberger, A. Krimmel, T. Kurz, H. -A. Krug Von Nidda, V. Y. Ivanov, A. A. Mukhin, A. M. Balbashov ve A. Loidl, "Structural, magnetic, and electrical properties of single-crystalline La_{1-x}Sr_xMnO₃ (0.4<x<0.85)", *Physical Review B*, volume 66, p. 094410, 2002.
- [50] A. Urushibara, Y. Moritomo, T. Arima, A. Asamitsu, G. Kido ve Y. Tokura,

- "Insulator-Metal Transition and Giant Magnetoresistance in $\text{La}_{1-x}\text{Sr}_x\text{MnO}_3$ ", *Physical Review B*, volume 51, no. 20, pp. 14103-109, 1995.
- [51] R. Mahendiran, S. K. Tiwary, A. K. Raychaudhuri, T. V. Ramakrishnan, R. Mahesh, N. Rangavittal ve C. Rao, "Structure, electron-transport properties, and giant magnetoresistance of hole-doped LaMnO_3 systems", *Physical Review B*, volume 53, no. 6, pp. 3348-58, 1996.
- [52] T. Mori, K. Inoue ve N. Kamegashira, "Phase behaviour in the system $\text{La}_{1-x}\text{Sr}_x\text{MnO}_{(5+x)/2}$ ($x=0.8-1.0$) with trivalent state of manganese ion", *Journal of Alloys and Compounds*, volume 308, pp. 87-93, 2000.
- [53] T. Negas ve R. Roth, "The System SrMnO_{3-x} ", *Journal of Solid State Chemistry*, volume 1, p. 409, 1970.
- [54] O. I. Lebedev, G. Van Tendeloo, S. Amelinckx, B. Leibold ve H. -U. Habermeier, "Structure and microstructure of $\text{La}_{1-x}\text{Ca}_x\text{MnO}_{3-\delta}$ thin films prepared by pulsed laser deposition", *Physical Review B*, volume 58, pp. 8065-73, 1998.
- [55] E. O. Wollan ve W. C. Koehler, "Neutron diffraction study of the magnetic properties of the series of perovskite-type compounds $[(1-x)\text{La},x\text{Ca}]\text{MnO}_3$ ", *Physical Review*, volume 100, no. 2, pp. 545-563, 1955.
- [56] "Superstructures formed by the ordering of vacancies in a selective oxidation catalyst- Grossly defective CaMnO_3 ", *Proceedings of the Royal Society of London Series A-Mathematical Physical and Engineering Sciences*, volume 394, pp. 223, 1984.
- [57] W. Schuddinck, G. Van Tendeloo, C. Martin, M. Hervieu ve B. Raveau, "Influence of oxygen content on the charge ordering process in $\text{La}_{0.5}\text{Ca}_{0.5}\text{MnO}_{3-x}$ ", *Journal of Alloys and Compounds*, volume 333, pp. 13-20,

2002.

- [58] P. K. Siwach, H. K. Singh ve O. N. Srivastava, "Low field magnetotransport in manganites", *Journal of Physics-Condensed Matter*, volume 20, p. 273201, 2008.
- [59] C. Wagner ve W. Schottky, *Z Physik Chem B*, volume 11, p. 163, 1930.
- [60] J. Maier, "Defect Chemistry : Composition, Transport, and Reactions in the Solid State; Part I: Thermodynamics", *Angewandte Chemie*, volume 32, no. 3, pp. 313-456, 1993.
- [61] J. Frenkel, "Die Electrodynamik des rotierenden Elektrons", *Z. Phys.*, volume 37, pp. 243-262, 1926.
- [62] F. A. Kröger ve H. J. Vink, "Relations between the Concentrations of Imperfections in Crystalline Solids", *Solid State Physics*, volume 3, pp. 307-435, 1956.
- [63] P. Kofstad, "Defect chemistry in metal oxides", *Phase Transitions: A Multifunctional Journal*, volume 58, pp. 75-93, 1996.
- [64] L. Malavasi, M. C. Mozzati, P. Ghigna, G. Chiodelli, C. B. Azzoni ve G. Flor, "Role of oxygen content on the transport and magnetic properties of $\text{La}_{1-x}\text{Ca}_x\text{MnO}_{3+\delta}$ Manganites", *Solid State Communications*, volume 123, no. 8, pp. 321-326, 2002.
- [65] P. Benzi, E. Bottizzo ve N. Rizzi, "Oxygen determination from cell dimensions in YBCO superconductors", *Journal of Crystal Growth*, volume 269, pp. 625-629, 2004.
- [66] A. Y. Zuev, V. V. Sereda ve D. S. Tsvetkov, "Defect Structure and Defect-induced Expansion of MIEC Oxides - Doped Lanthanum Cobaltites", *ECS*

Transactions, volume 45, pp. 63-73, 2012.

- [67] R. Moreno, J. Zapata, J. Roqueta, N. Bagues ve J. Santiso, "Chemical Strain and Oxidation-Reduction Kinetics of Epitaxial Thin Films of Mixed Ionic-Electronic Conducting Oxides Determined by X-ray Diffraction", *Journal of Electrochemical Society*, volume 161, pp. 3046-51, 2014.
- [68] D. Marrocchelli, S. R. Bishop, H. L. Tuller ve B. Yildiz, "Understanding Chemical Expansion in Non-Stoichiometric Oxides: Ceria and Zirconia Case Studies", *Advanced Functional Materials*, volume 22, pp. 1958-65, 2012.
- [69] L. Minervini ve M. O. Zacate, "Defect cluster formation in M_2O_3 -doped CeO_2 ", *Solid State Ionics*, volume 116, pp. 339-349, 1999.
- [70] S. R. Bishop, "Chemical expansion of solid oxide fuel cell materials: A brief overview", *Acta Mechanica Sinica*, volume 29, no. 3, pp. 312-317, 2013.
- [71] V. V. Kharton, *Solid State Electrochemistry II: Electrodes, Interfaces and Ceramic Membranes*, John-Wiley & Sons Inc., 2011.
- [72] W. D. Callister Jr. ve D. G. Rethwisch, *Material Science and Engineering*, John Wiley & Sons, 2010.
- [73] D. A. Padmavathi, "Potential Energy Curves & Material Properties", *Scientific Research*, volume 2, pp. 97-104, 2011.
- [74] S. R. Bishop, H. L. Tuller, Y. Kuru ve B. Yildiz, "Chemical expansion of nonstoichiometric $Pr_{0.1}Ce_{0.9}O_{2-\delta}$: Correlation with defect equilibrium model", *Journal of the European Ceramic Society*, volume 31, pp. 2351-2356, 2011.
- [75] S. R. Bishop, K. L. Duncan ve E. D. Wachsman, "Thermo-Chemical Expansion in Strontium-Doped Lanthanum Cobalt Iron Oxide", *Journal of American Chemical Society*, volume 93, pp. 4115-4121, 2010.

- [76] S. R. Bishop, D. Chen, Y. Kuru, J. -J. Kim, T. Stefanik ve H. L. Tuller, "Measurement and Modeling of Electrical, Mechanical, and Chemical Properties of a Model Mixed Ionic Electronic Conductor: Pr Doped Ceria", *ECS Transactions*, volume 33, no. 40, pp. 51-57, 2011.
- [77] N. Swaminathan, J. Qu ve Y. Sun, "An electromechanical theory of defects in ionic solids", *Philosophical Magazine*, volume 87, p. 1705, 2007.
- [78] R. Krishnamurthy ve B. W. Sheldon, "Stresses due to oxygen potential gradients in non-stoichiometric oxides", *Acta Materialia*, volume 52, p. 1807, 2004.
- [79] T. Kushi, K. Sato, A. Unemoto, K. Amezawa, T. Kawada, S. Singhal ve K. Eguchi, "Mechanical Properties of $Ce_{0.9}Gd_{0.1}O_{2-\delta}$ at High Temperatures under Controlled Atmospheres", *ECS Transactions*, volume 35, p. 1145, 2011.
- [80] Y. Kuru, S. R. Bishop, J. -J. Kim, B. Yildiz ve H. L. Tuller, "Chemomechanical properties and microstructural stability of nanocrystalline Pr-doped ceria: An in situ X-ray diffraction investigation", *Solid State Ionics*, volume 193, pp. 1-4, 2011.
- [81] S. B. Adler, "Chemical expansivity of electrochemical ceramics", *Journal of American Chemical Society*, volume 84, p. 2117, 2001.
- [82] S. Wang , M. Katsuki, M. Dokiya ve T. Hashimoto , "High temperature properties of $La_{0.6}Sr_{0.4}Co_{0.8}Fe_{0.2}O_{3-\delta}$ phase structure and electrical conductivity", *Solid State Ionics*, volume 159, p. 71, 2003.
- [83] X. Y. Chen, J. S. Yu ve S. B. Adler, "Thermal and Chemical Expansion of Sr-Doped Lanthanum Cobalt Oxide($La_{1-x}Sr_xCoO_{3-\delta}$)", *Chemistry of Materials*, volume 17, p. 4537, 2005.
- [84] S. McIntosh, J. F. Vente, W. G. Haije, D. H. A. Blank ve H. J. M.

- Bouwmeester, "Oxygen Stoichiometry and Chemical Expansion of $\text{Ba}_{0.5}\text{Sr}_{0.5}\text{Co}_{0.8}\text{Fe}_{0.2}\text{O}_{3-\delta}$ Measured by in Situ Neutron Diffraction", *Chemistry of Materials*, volume 18, p. 2187, 2006.
- [85] S. Miyoshi, J. -O. Hong, K. Yashiro, A. Kaimai, Y. Nigara, K. Kawamura, T. Kawada ve J. Mizusaki, "Lattice expansion upon reduction of perovskite-type LaMnO_3 with oxygen-deficit nonstoichiometry", *Solid State Ionics*, volume 161, p. 209, 2003.
- [86] M. Vracar, A. Kuzmin, R. Merkle, J. Purans, E. A. Kotomin, J. Maier ve O. Mathon, "Jahn-Teller distortion around Fe^{4+} in $\text{Sr}(\text{Fe}_x\text{Ti}_{1-x})\text{O}_{3-\delta}$ from x-ray absorption spectroscopy, x-ray diffraction and vibrational spectroscopy", *Physical Reviews B*, volume 76, p. 174107, 2007.
- [87] V. V. Kharton, A. A. Yaremchenko, M. V. Patrakeev, E. N. Naumovich ve F. M. B. Marques, "Thermal and chemical induced expansion of $\text{La}_{0.3}\text{Sr}_{0.7}(\text{Fe}, \text{Ga})\text{O}_{3-\delta}$ ceramics", *Journal of European Ceramic Society*, volume 23, p. 1417, 2003.
- [88] L. A. Isupova, S. V. Tsybulya, G. N. Kryukova, G. M. Alikina, N. N. Boldyreva, I. S. Yakovleva, V. P. Ivanov ve V. A. Sadykov, "Real structure and catalytic activity of $\text{La}_{1-x}\text{Ca}_x\text{MnO}_{3-\delta}$ perovskites", *Solid State Ionics*, Volume 1/2 141-142, pp. 417-425, 2001.
- [89] *Ceramic Processing: Powder Preparation and Forming*, Japan: Ceramic Society of Japan, 1984.
- [90] M. A. Gülgün, M. H. Nguyen ve W. M. Kriven, "Polymerized Organic-Inorganic Synthesis of Mixed Oxides", *Journal of the American Ceramic Society*, volume 82, pp. 556-560, 1999.
- [91] H. Lee, M. Hong, S. Bae, H. Lee, E. Park ve K. Kim, "A novel approach to preparing nano-size Co_3O_4 -coated Ni powder by the Pechini method for MCFC

- cathodes", *Journal of Materials Chemistry*, volume 13, pp. 2626-2632, 2003.
- [92] A. Abrue Jr., S. M. Zanetti, M. A. S. Oliveira ve G. P. Thim, "Effect of Urea on Lead Zirconate Titanate - $\text{Pb}(\text{Zr}_{0.52}\text{Ti}_{0.48})\text{O}_{3-\delta}$ Nanopowders Synthesized by the Pechini Method", *Journal of the European Ceramic Society*, volume 25, pp. 743-748, 2004.
- [93] R. J. Wiglusz, A. Gaki, G. Kakali, A. Chuchmala ve W. Streck, "Conductivity and electric properties of $\text{La}_{1-x}\text{Sr}_x\text{MnO}_{3-\delta}$ nanopowders", *Journal of Rare Earths*, volume 27, p. 651, 2009.
- [94] K. K. Hansen ve V. K. Hansen, "A-site deficient $(\text{La}_{0.6}\text{Sr}_{0.4})_{1-x}\text{Fe}_{0.8}\text{Co}_{0.2}\text{O}_{3-\delta}$ perovskites as SOFC cathodes", *Solid State Ionics*, volume 178, pp. 1379-84, 2007.
- [95] K. P. Shinde, N. G. Deshpande, T. Eom, Y. P. Lee ve S. H. Pawar, "Solution-combustion synthesis of $\text{La}_{0.65}\text{Sr}_{0.35}\text{MnO}_3$ and the magnetocaloric properties", *Material Science and Engineering B*, volume 167, pp. 202-205, 2010.
- [96] W. W. Lee ve J. M. Lee, "Novel synthesis of high performance anode materials for lithium-ion batteries (LIBs)", *Journal of Materials Chemistry A*, volume 2, pp. 1589-1626, 2014.
- [97] D. Segal, *Chemical Synthesis of Advanced Ceramic Materials*, Cambridge University Press, 1991.
- [98] W. L. Sin, K. H. Wong ve P. Li, "Surfactant Effect on Synthesis of Nanocrystalline $\text{La}_x\text{Sr}_{1-x}\text{MnO}_3$ by Hydrothermal Method", *Acta Physica Polonica A*, volume 111, pp. 165-171, 2007.
- [99] M. Marinsek, K. Zupan, T. Razpotnik ve J. Macek, "A co-precipitation procedure for the synthesis of LSM material", *Materials and technology*, volume 41, p. 85, 2006.

- [100] U. Adem, "Preparation of $\text{Ba}_x\text{Sr}_{1-x}\text{TiO}_3$ Thin Films by Chemical Solution Deposition and Their Electrical Characterization", 2003.
- [101] I. Dhiman, A. Das, P. K. Mishra ve L. Panicker, "The Influence of A-site Ionic Radii on the Magnetic Structure of Charge Ordered $\text{La}_{0.5}\text{Ca}_{0.5-x}\text{Sr}_x\text{MnO}_3$ Manganites", *Physical Review B, Condensed Matter*, volume 77, no. 9, 2008.
- [102] T. Grande, J. Tolchard ve S. M. Selbach, "Anisotropic Thermal and Chemical Expansion in Sr-Substituted $\text{LaMnO}_{3-\delta}$: Implications for Chemical Strain Relaxation", *Chemistry of Materials*, volume 24, no. 2, pp. 338-345, 2012.